PULSED ELECTROMAGNETIC FIELDS:

THEIR POTENTIALITIES, COMPUTATION AND EVALUATION

NWO
Netherlands Organisation for Scientific Research

UGC 大學教育資助委員會
University Grants Committee

Delft University of Technology

University of Hong Kong

Pulsed Electromagnetic Fields:

Their Potentialities, Computation and Evaluation

Proceedings of the Workshop

March 18–19, 2013, Delft, the Netherlands

edited by

Ioan E. Lager
Delft University of Technology, the Netherlands

and

Li Jun Jiang
University of Hong Kong, Hong Kong, China

2013
IOS Press

ISBN 978-1-61499-229-5 (print)
ISBN 978-1-61499-230-1 (online)

Published by IOS Press BV under the imprint Delft University Press

IOS Press BV
Nieuwe Hemweg 6b
1013 BG Amsterdam
The Netherlands
tel: +31−20−688 3355
fax: +31−20−687 0019
email: info@iospress.nl
www.iospress.nl

PRINTED IN THE NETHERLANDS

This publication is supported by:
Netherlands Organisation for Scientific Research (NWO)

and

Research Grants Council of Hong Kong (RGC) /
University Grants Committee of Hong Kong

Preface

Exploiting the potentialities of electromagnetic (EM) fields with high pulse rates is at the core of the Computer Science's challenging demand for designing ultra-fast integrated circuits that are capable of handling the digital signals involved, next to exploiting the possibilities of wireless (i.e., pulsed EM fields supported) digital information transfer.

To address this challenge, the Workshop **Pulsed Electromagnetic Fields: Their Potentialities, Computation and Evaluation** collects state-of-the-art contributions on the computational modeling of pulsed EM fields in configurations that are representative for road mapping future developments. Furthermore, it sets itself the task to accommodate relevant interaction as to in which direction these developments are to be pursued. The included works cover a very broad range, from the physical and mathematical foundations up to operational systems making use of the potentialities arising from the use of pulsed EM fields.

The workshop will set the course for an intensified and formalized cooperation on fundamental research between the Delft University of Technology and the University of Hong Kong. Two aspects are here primarily envisaged: the impact of pulsed EM fields with ultra-high pulse rates on the methods for designing integrated circuits and systems for inter- and intra-device wireless transfer of information, and the evaluation of the possible impact of such fields on the 'Electromagnetic environment', in particular their Electromagnetic Interference with 'living and inert matter'.

The organizers express their gratitude to the Netherlands Organisation for Scientific Research (NWO) and Research Grants Council of Hong Kong (RGC) / University Grants Committee of Hong Kong that provided the financial means for the workshop's organization via their "Collaboration Hong Kong – Joint Research Scheme". They also extend their gratitude to the specialized Delft University of Technology departments that provided the logistic support for this event.

Ioan E. Lager
Li Jun Jiang.

Delft and Hong Kong, January 25, 2013.

Contents

Wave analysis of Airy beams and Airy Pulsed Beams

Yan Kaganovsky[†] and **Ehud Heyman**[‡]
[†]*Duke University, Dept. of Electrical and Computer Engineering,*
Durham, NC 27708, USA, e-mail: yankagan@gmail.com

[‡]*Tel Aviv University, School of Electrical Engineering,*
Tel Aviv 69978, Israel

Abstract

The Airy beam (AiB) has attracted a lot of attention recently because of its intriguing features. We have previously provided a cogent physical explanation for these properties by showing that the AiB is, in fact, a caustic of rays that radiate from the tail of the Airy function aperture distribution. We have also introduced a class of ultra wide band (UWB) Airy pulsed beams (AiPB), where a key step has been the use of a proper frequency scaling of the initial aperture field that ensures that all the frequency components propagate along the same curved trajectory so that the wavepacket of the AiPB does not disperse. An exact closed form solution for the AiPB has been derived using the spectral theory of transients (STT) which is an extension of the well know Cagniard–de Hoop (CdH) method. In this paper we discuss the properties of the AiB and AiPB, and use the present problem to discuss the relation between the CdH method and the STT.

1 Introduction

Recently, a class of Airy beam (AiB) solutions of the paraxial time-harmonic wave equation was introduced [1–4]. Originally, these beams were formulated in a 2D coordinate space, say (x, z), and were generated by setting an Airy function as the initial field distribution in the aperture plane $z = 0$. Later on, finite energy AiB's were obtained by multiplying the Airy function aperture distribution by exponential or Gaussian windows, leading to closed form field solutions in [2] and [3], respectively.

Pulsed Electromagnetic Fields: Their Potentialities, Computation and Evaluation
I. E. Lager and L. J. Jiang (Eds.).
doi: 10.3233/978-1-61499-230-1-1

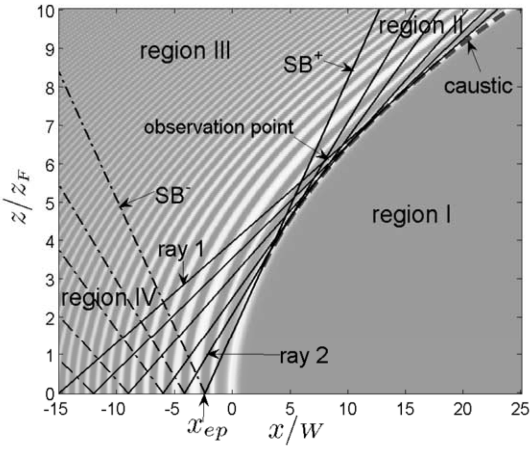

Figure 1: Ray description of the Airy beam plotted on a background of the intensity of the Airy beam in (2) (see [6, Fig. 1]). The z and x axes are normalized with respect to the Fresnel length z_{F} and the beamwidth W, respectively. As discussed in (7), the rays of species $\hat{U}^{+}$ (solid lines) radiate to the right with respect to the z-axis and converge to a caustic that delineates the AiB propagation trajectory. Species $\hat{U}^{-}$ (dashed-dotted lines) radiates to the left and diverges. As discussed in (8), species $\hat{U}^{+}$ has additional set of rays that emerge from distant points in the aperture (beyond the figure frame) and do not converge on that caustic. These rays are shown in Fig. 2 but they have been removed here for clarity. Other parameters that appear in this figures are used in [6] but are not used here.

The AiB's attracted a lot of attention because of their intriguing features, the most distinctive one is the propagation along *curved* trajectories in free-space. These beams are also weakly diffractive along their trajectories, i.e., they retain their structure and remain essentially diffraction-free for distances that are much longer than the conventional diffraction (Rayleigh) length of Gaussian beams with the same width [2]. Another interesting feature, pointed out in [5], is the ability of the AiB to 'heal' itself, i.e., regenerate itself if the main beam is obstructed.

A cogent physical description to the AiB's and their intriguing properties has been presented in [6]. In that paper we have shown that the AiB is not generated by the main lobe of the Airy function in the aperture, but rather it is a caustic of rays that emanate from the oscillatory tail of this function and then focus on the caustic (Fig. 2). This also implies that the evolution of the main lobe of the AiB along the curved trajectory is not described by a local wave dynamics, and hence it cannot be regarded as a 'beam field' in that sense. These concepts were extended in [7] to construct an AiB in a 3D coordinate space, where the structure of the caustic is much more complicated and requires the use of catastrophe theory.

The results of [6] have been utilized in [8] to introduce a class of ultra wide band (UWB) Airy pulsed beams (AiPB) with *frequency independent* ray skeleton, thus ensuring that all the frequency components of the AiB propagate along the same curved trajectory and in the overall, the AiPB wavepacket does not disperse. We also derived an exact closed-form TD solution for the AiPB via the spectral theory of transients (STT) [9–12]. The TD properties of the AiPB provide further insight into the wave mechanism of the AiB. Finally, in [7] we extended the non dispersive AiB solution to a 3D space where the caustic has the much more complicated structure of a *hyperbolic umbilic* catastrophe that evolves into a *parabolic umbilic* catastrophe.

The STT is an extension of the celebrated Cagniard–de Hoop (CdH) method [13–15] for the direct inversion into the TD of FD solutions that are given as spatial-spectrum integrals. In the CdH method, the TD solutions are recovered by manipulating the FD spectral integrals into a form from which one may infer the TD solutions. In the STT, on the other hand, the FD integrals are converted to the TD so that the TD fields are expressed as a spatial-spectrum integral of *transient plane waves*. This STT integral can be evaluated in a closed form, leading to results that are similar to those derived via the CdH method in those cases where the latter is applicable. Yet the STT provides a more flexible framework that may be used in cases where the CdH cannot be applied, e.g., problems involving reflections and diffraction of complex source pulsed beams (CSPB) [16, 17] (see STT solutions of 3D-CSPB reflection and diffraction at plane dielectric interfaces [18] and at wedges [19–21]). One of the main goals of the present paper is to discuss the concepts of the STT in the context of the AiPB where the CdH approach in not applicable.

The presentation starts in Section 2 with a wave-analysis of the AiB in the FD. It presents the ray interpretation of the AiB and the frequency scaling of the parameters such that the radiating field is *non-dispersive* in the sense that the ray skeleton and the propagation trajectory are frequency independent. The STT formulation and the derivation of the exact TD solution (21) are then considered in Section 3, following some numerical results that provide further insight into the wave mechanism of the AiB. The exact solution describes the field everywhere as an implicit function of space and time. One may derive explicit wavefront approximations for the time windows near the pulse arrival. This topic and others are discussed in [8].

2 Non dispersive Airy beams – frequency domain representation

The finite-energy non dispersive Airy beams (AiB) field $\hat{U}(x,z)$ in the half-space $z>0$ of a 2D coordinate frame $\boldsymbol{r}=(x,z)$ is generated by the aperture field distribution at $z=0$

$$\hat{U}_0(x';\omega)=\mathrm{Ai}(\beta^{-1/3}k^{2/3}x')e^{\alpha kx'} \tag{1}$$

where x' referrers to points in the aperture, Ai is the Airy function, and the exponential window is added in order to render the energy of this distribution finite. Here and henceforth, an over hat denotes time-harmonic constituents with harmonic time-dependence $e^{-\mathrm{i}\omega t}$, $k=\omega/c$ and a subscript 0 indicates values in the $z=0$ plane.

In (1) we used a specific frequency scaling of the parameters such that β and α are frequency-independent parameters. This scaling, first introduces in [7] in contradistinction to previous suggestions (e.g., [22]), ensures that the radiating AiB is *non-dispersive* in the sense that it has a *frequency independent ray skeleton* (see (7)) thus ensuring that all frequency components propagate along the same ray trajectories and focus onto the same caustic which delineated the AiB propagation trajectory (see (3)). We note that the parameters β and α used here are related to the parameters x_0 and α_0 used in the AiB literature (e.g., [2]) via $x_0=\beta^{1/3}k^{-2/3}$ and $\alpha_0=(k\alpha)^{1/3}$.

The paraxial solution for the radiating AiB field due to the initial conditions in (1) is [2]

$$\begin{aligned}\hat{U}(\boldsymbol{r};\omega)=\mathrm{Ai}\big[(k\beta)^{2/3}\big(x/\beta-(z/2\beta)^2+\mathrm{i}\alpha z/\beta\big)\big]\\ \times e^{\mathrm{i}k(z+xz/2\beta-z^3/12\beta^2+\alpha^2z/2)}e^{k\alpha(x-z^2/\beta)}.\end{aligned} \tag{2}$$

One readily verifies that the beam envelope shifts transversely without change along a parabolic trajectory (see Fig. 1)

$$x/\beta=\big(z/2\beta\big)^2. \tag{3}$$

Note that this trajectory is frequency-independent because of the frequency scaling of the parameters in (1).

2.1 Ray representation

In order to facilitate ray analysis we use the asymptotic expression $\mathrm{Ai}(\xi)\sim(-\pi^2\xi)^{-1/4}\sin\big[2/3(-\xi)^{3/2}+\pi/4\big]$ for $\xi\ll-1$ and decompose the aperture

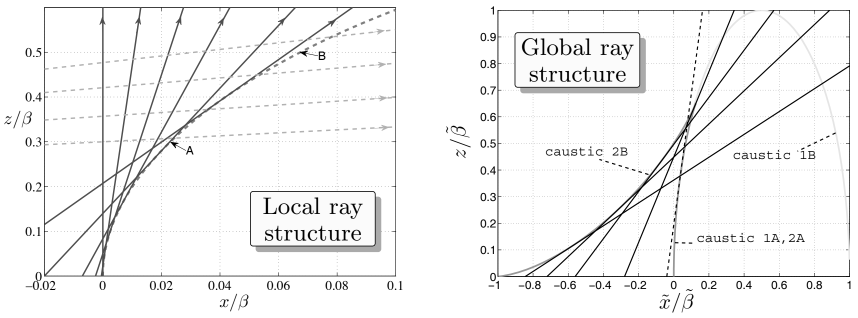

a b

Figure 2: Local and global structures of ray species $\hat{U}^+$. Note the scale difference of the x axes in (a) and (b). All axes are normalized. (a) The solid line rays radiate from the aperture at $z = 0$ and converge onto a caustic (dashed line). The dashed line rays originate at distant points where the aperture field is weak (see also (b)). They intersect the caustic at very late times, beyond the pertinent time-window of the AiPB, and do not focus there. These rays are not included in the paraxial solution of (2). Points $A = (x, z) = (0.023, 0.3)\beta$ and $B = (0.067, 0.5)\beta$ are typical points on the caustic where the field will be calculated in the sequel. (b) The global ray picture described by the cusped caustic formed by the two grey caustics 2A and 2B that merge into a cusp. This figure is taken from [7, Fig. 16]. That reference deals with 3D Airy beams, where the caustic has a much more complicated 3D structure of a *hyperbolic umbilic* catastrophe that evolves into a *parabolic umbilic* catastrophe [26, Fig. 7.3]. Nevertheless, since this figure depicts a cross sectional cut of the catastrophe in the symmetry plane, the cusped caustic above referred to describes also the ray structure of the 2D problem considered here with $\tilde{\beta} = \beta$ and $\tilde{x} = x$. It consists of two parts 2A and 2B that merge in a cusp. The solid lines are the corresponding rays.

field at $x \ll -k^{-2/3}\beta^{1/3}$ into a sum of two local plane wave constituents, viz.

$$\hat{U}_0(x') \approx A_0^+ \exp\left(\mathrm{i}k\psi_0^+\right) + A_0^- \exp\left(\mathrm{i}k\psi_0^-\right) \equiv \hat{U}_0^+(x') + \hat{U}_0^-(x') \qquad (4)$$

where the initial phase and amplitude functions $\psi_0^\pm$ and $A_0^\pm$ are given by

$$k\psi_0^\pm(x') = \mp\left[k(2/3)(-x')^{3/2}\beta^{-1/2} + \pi/4\right] \qquad (5)$$

$$A_0^\pm(x') = \pm(\mathrm{i}/2\sqrt{\pi})\left[-xk^{2/3}\beta^{-1/3}\right]^{-1/4}e^{\alpha k x'}. \qquad (6)$$

We assume here that α is sufficiently small so that it is included in the amplitudes functions $A_0^\pm$ and note in the phase $\psi_0^\pm$. This assumption will be removed in the exact TD analysis in Section 3.

The initial fields $\hat{U}_0^{\pm}$ in (4) give rise to rays that emerge from points $x' < 0$ in the aperture at local angles (measured with respect to the z-axis)

$$\theta^{\pm}(x') = \sin^{-1}\left[\partial_{x'}\psi_0^{\pm}(x')\right] = \pm\sin^{-1}[(-x'/\beta)^{-1/2}]. \tag{7}$$

Ray species $\hat{U}^{-}$ emerges to the left with respect to the z axis and diverges (dashed-dotted line rays in Fig. 1), giving rise to a weak contribution there. Ray species $\hat{U}^{+}$ emerges to the right (solid lines in Fig. 1) and converges to a caustic that delineates the curved beam trajectory. The paraxially approximated caustic is given in (3), but the exact caustic can be obtained via a standard ray analysis as outlined in the Appendix of [8].

From (7), the exit points x' of species $\hat{U}_0^{+}(x)$ corresponding to a given observation point $\boldsymbol{r} = (x, z)$ on the lit side of the caustic is found via

$$\sin\theta(x') = (-x'/\beta)^{-1/2} = (x - x')/\rho, \quad \rho = \sqrt{(x - x')^2 + z^2}, \tag{8}$$

with ρ denoting the distance along the ray. This equation has *three* solutions, denoted as $x'_{1,2,3}$ in accord with their arrival times. Rays 1 and 2 converge onto the caustic such that ray 2 has touched the caustic before reaching the observer while ray 1 has not (see Figs. 1 and 2(a)). The third solution corresponds to rays that originate at distant points where the aperture field is weak (dashed lines in Fig. 2(a)). They intersect the caustic at very late times, beyond the pertinent time-window of the AiPB, and yield weak contributions. By definition, these contributions are not included in the paraxial solution of (2). Note that the paraxially approximated caustic in (3) is obtained from (8) by replacing there $\rho \to z$.

The complete (exact) ray structure calculated via (8) is described by the cusped caustic in Fig. 2(a) consisting of two caustics 2A and 2B (grey lines) that merge in a cusp (Fig. 16 from [7]). Caustic 2A is formed by the convergence of rays 1 and 2, and describes the AiB propagation trajectory. Caustic 2B is formed by the convergence of rays 1 and 3, and, as noted earlier, it is irrelevant for the field near the AiB propagation trajectory. Note that beyond the cusp, the field disperses and losses its beam shape. This limits the AiB propagation range to a distance of order 0.6β (see Fig. 2(a)) hence β should be chosen according to application. The range is also determined by the parameter α which controls the decay rate along the beam axis.

The field of the AiB may now be calculated using ray techniques. A uniform ray-based solution that is valid near the caustic where the standard ray solution fails, has been derived in [6] via the the uniform geometrical optics (UGO) [23, 24]. The UGO solution fully agrees with the paraxially approximated AiB solution in (2) in the region where the latter is valid. This ray solution provides a cogent physical description to the AiB and explains its intriguing properties. It is also more accurate than the solution in (2), in particular at large ranges where (2) fails since the parabolic trajectory in (3) deviates substantially from the true caustic obtained via the ray analysis. We do not present the analysis here; this has been done in [7] in the context of the more complicated 3D AiB (see Figs. 11,12 there).

3 Time domain solutions – Airy pulsed beams

As discussed in Section 2, the specific scaling of the initial field in (1) ensures that all frequency components of the field are AiB that propagate along the same curved trajectory (3). If the initial conditions are pulsed, they generate a non-dispersive wavepacket that propagates along the curved trajectory, henceforth denoted as Airy Pulsed Beams (AiPB).

The TD expression for the AiPB can be obtained by converting the FD paraxial solution (2). Here, however, we use an alternative approach which is based on an exact spectral representation in the TD via the spectral theory of transients (STT) [9–12]. This approach leads to an exact closed-form TD solutions for the AiPB and it does not suffer from the difficulties of the paraxial approximation noted above.

The following section reviews the concepts of the STT in the context of the AiPB. In Section 3.2 we construct the STT integral representation of the time-dependent AiPB field, which is a spatial-spectrum integral of *transient plane waves.* The general procedure for evaluating this integral is discussed in Section 3.3, while Section 3.4 presents the details of the spectral evaluation in the present case. Finally in Section 3.5 we present numerical results for the AiPB that provide new insight into the wave mechanism of the AiB.

3.1 Analytic signal formulation

Analytic signals are extensions of physical time signals that can accommodate a complex time variable. Therefore, they are a useful tool in TD wave theory in applications involving complex propagation times delays, e.g., in complex-spectrum representations such as the STT, or in accommodating the off-axis field of beams [16, 17].

An analytic TD wave-function is related to the FD solution $\hat{U}(\boldsymbol{r};\omega)$ via the one sided Fourier transform

$$\overset{+}{u}(\boldsymbol{r},t)=\frac{1}{\pi}\int_0^\infty \mathrm{d}\omega e^{-\mathrm{i}\omega t}\hat{f}(\omega)\hat{U}(\boldsymbol{r};\omega),\quad \mathrm{Im}(t)\leqslant 0 \tag{9}$$

where $\hat{U}$ is a frequency domain solution and $\hat{f}(\omega)$ is an arbitrary temporal spectrum. Since the integral converges for real t, it also converges for all $t \in \mathbb{C}^-$, the lower half of the complex plane, thus defining an analytic function there. Here and henceforth analytic signals are denoted by an over $+$ symbol. The physical signal field for real t is obtained by

$$u(\boldsymbol{r},t) = \mathrm{Re}\left[\overset{+}{u}(\boldsymbol{r},t)\right], \quad \mathrm{Im}(t) \uparrow 0. \tag{10}$$

Actually, multiplying $\overset{+}{u}$ by a complex parameter $e^{\mathrm{i}\gamma}$, $\gamma \in [-\pi,\pi]$, one obtains via (10) a real solution $u(\boldsymbol{r},t)$ as a linear combination of $\mathrm{Re}\left(\overset{+}{u}\right)$ and $\mathrm{Im}\left(\overset{+}{u}\right)$.

In (15) we make use of the convolution theorem for analytic signals. Stated generally, given two analytic signals $\overset{+}{f}$ and $\overset{+}{g}$, with spectra $\hat{f}$ and $\hat{g}$, the analytic signal $\overset{+}{w}$ corresponding to $\hat{w} = \hat{f}\hat{g}$ is

$$\begin{aligned}\overset{+}{w}(t) &= \frac{1}{\pi}\int_0^\infty \mathrm{d}\omega e^{-\mathrm{i}\omega t}\, \hat{f}(\omega)\, \hat{g}(\omega) = \frac{1}{2}\int_{-\infty}^{\infty} \mathrm{d}t' \overset{+}{f}(t')\, \overset{+}{g}(t-t') \\ &\equiv \frac{1}{2}\overset{+}{f}(t) \otimes \overset{+}{g}(t),\end{aligned} \tag{11}$$

where $\mathrm{Im}(t) \leqslant 0$ while the t'-integration is performed along the real axis.

3.2 STT integral representation of the AiPB

In order to derive the STT representation of the AiPB, namely its representation as a spectrum of *transient plane-waves*, we start with the spectral (plane-wave) representation of the FD aperture field (1) [25, Eq. (9.5.4)]

$$\hat{U}_0(x';\omega) = \frac{\omega^{1/3}}{2\pi}\int_{-\infty}^{\infty} \mathrm{d}\xi\, A e^{\mathrm{i}\omega\tau_0(\xi)}\, e^{\mathrm{i}\omega\xi x'/c}, \tag{12}$$

$$\tau_0(\xi) = \beta(\xi + \mathrm{i}\alpha)^3/3c, \quad A = (\beta/c)^{1/3} \tag{13}$$

where $e^{\mathrm{i}\omega\xi x'/c}$ in (12) is identified as the Fourier kernel, and the spectral variable ξ is normalized such that the frequency ω appears explicitly in this kernel. With this normalization, ξ has a *frequency-independent* geometrical interpretation that enables a closed form inversion of the spectrum to the TD, as in (15).

The radiated field is obtained by adding the spectral propagator, viz.

$$\hat{U}(\boldsymbol{r};\omega) = \frac{\omega^{1/3}}{2\pi}\int_{\mathcal{C}} \mathrm{d}\xi\, A e^{\mathrm{i}\omega\tau(\xi)}, \quad \tau(\xi;\boldsymbol{r}) = \tau_0(\xi) + \xi x/c + \zeta z/c \tag{14}$$

where $\zeta = \sqrt{1-\xi^2}$ is the spectral wave-number in the z-direction, chosen with $\mathrm{Im}(\zeta) \geqslant 0$ for $\omega > 0$, and the integration contour $\mathcal{C}$ extends along the real ξ axis from $-\infty$ to ∞, passing above and below the branch point $\xi = \mp 1$ corresponding to ζ (Fig. 3). Equation (14) expresses the field as a spectrum of plane-waves propagating at angles $\theta(\xi) = \sin^{-1}\xi$ with respect to the z axis.

The TD solution is obtained now by applying the analytic (one-sided) Fourier transform (9), obtaining

$$\overset{+}{u}(\boldsymbol{r},t) = \frac{1}{2\pi^2}\int_0^\infty \mathrm{d}\omega e^{-\mathrm{i}\omega t}\,\hat{g}(\omega)\int_{\mathcal{C}} \mathrm{d}\xi\, A e^{\mathrm{i}\omega\tau(\xi)} \tag{15}$$

where, for simplicity, we use $\hat{f}(\omega) = \omega^{-1/3}\hat{g}(\omega)$.

The reasons for using the analytic signal formulation are:

- The non dispersive spectral integral in (14) has a different form for $\omega > 0$ and $\omega < 0$ (e.g., for $\omega < 0$, the square root of ζ in (14) should be chosen with $\mathrm{Im}(\zeta) \leqslant 0$). Leaving out the negative frequencies simplifies the analysis.

- The one sided transform allows using $\mathrm{Im}(t) \leqslant 0$ and switching the order of the ξ and ω integrations in (15). The latter can then be evaluated in closed-form as in (16).

- Adding a small imaginary part to t displaces the location of the integrand's singularities in the complex ξ plane in a way that clarifies their location with respect to the integration path (see (19)).

Following the discussion above, we switch the order of integrations in (15) and evaluate the ω integration in a closed form, using also (11), obtaining

$$\overset{+}{u}(\boldsymbol{r},t) = \frac{1}{2}\overset{+}{g}(t) \otimes \frac{-\mathrm{i}}{2\pi^2}\int_{\mathcal{C}} \mathrm{d}\xi\,\frac{A}{t-\tau(\xi)}. \tag{16}$$

The ξ-integral in (16), denoted as the *STT integral*, represents the field as a spectrum of transient plane-waves. It is convenient at this point to change the definition of the complex square root in ζ such that $\mathrm{Re}(\zeta) \geqslant 0$ on the upper Riemann sheet [9, 10]. The resulting branch cuts of ζ extend along the real ξ-axis from ∓ 1 to $\mp\infty$, respectively (Fig. 3). This change has no effect on the result of the integral.

There are several classes of signals for which the convolution above can be evaluated in a closed-form. Here we use the class of analytic δ signals whose spectral and temporal counterparts are given by

$$\hat{g}(\omega) = e^{\mathrm{i}\gamma}(-i\omega)^m e^{-\omega T}, \quad \overset{+}{g}(t) = e^{\mathrm{i}\gamma}\overset{+}{\delta}{}^{(m)}(t-\mathrm{i}T) = e^{\mathrm{i}\gamma}\partial_t^m \frac{1}{\pi\mathrm{i}}\,\frac{1}{t-\mathrm{i}T} \tag{17}$$

with $m = 0, 1, 2....$ The parameter $T > 0$ is proportional to the pulse length. The amplitude parameter $e^{\mathrm{i}\gamma}$, where $\gamma \in [-\pi, \pi]$, controls the balance between the real and imaginary parts of the analytic signal when one calculates the physical signal via (10). The function $\overset{+}{\delta}{}^{(m)}$ is the m-th derivative of the analytic δ function, having m oscillations for $|t| < T$ and a t^{-m-1} decay rate for $|t| \gg T$. In the example of Section 3.5 we use $m = 2$.

Using (17) and (11), Eq. (16) becomes

$$\overset{+}{u}(\boldsymbol{r}, t) = \partial_t^m \frac{-\mathrm{i}e^{\mathrm{i}\gamma}}{2\pi^2} \int_{\mathcal{C}} \mathrm{d}\xi \, \frac{A}{t - \tau(\xi) - \mathrm{i}T}. \tag{18}$$

3.3 Evaluation of the STT integral

The integral in (18) has time-dependent poles $\xi(t)$ in the complex ξ plane, defined by

$$\tau[\xi(t)] = \beta(\xi + \mathrm{i}\alpha)^3/3c + \xi x/c + \zeta z/c = t - \mathrm{i}T. \tag{19}$$

The solutions $\xi(t)$ to (19) are generally found numerically via a search algorithm. This search is simplified by using, as a starting point, the paraxial approximation $\zeta \approx 1 - \xi^2/2$, in which case (19) reduces to a third order polynomial equation with a closed-form solution. These solutions are generally complex, and are located in the upper and in the lower Riemann sheets (URS or LRS, respectively), where $\mathrm{Re}(\zeta) \gtrless 0$. Further details are given in Section 3.4 and Figs. 3 and 4.

The integral in (18) can be evaluated by closing the integration contour at infinity about the lower or the upper half of the complex ξ-plane, thus expressing the field as contributions from the poles $\xi(t)$ lying in the respective half plane, plus a contribution from the branch-cuts of ζ that extend along the real ξ-axis,

$$\overset{+}{u}(\boldsymbol{r}, t) = \mp \sum_p \partial_t^m \frac{A\, e^{\mathrm{i}\gamma}}{\pi\tau'\big[\xi^{(p)}(t)\big]} + \partial_t^m \frac{-\mathrm{i}e^{\mathrm{i}\gamma}}{2\pi^2} \int_{\mathcal{I}_b^{\pm}} \mathrm{d}\xi \, \frac{A}{t - \tau(\xi) - \mathrm{i}T} \tag{20}$$

$$\simeq \mp \sum_p \partial_t^m \frac{A\, e^{\mathrm{i}\gamma}}{\pi\tau'\big[\xi^{(p)}(t)\big]} \tag{21}$$

where the upper and lower signs correspond to the upper or lower half-plane closures, respectively. The first term in (20) represents the contribution of all the poles $\xi^{(p)}(t)$ in the respective half plane with p being an index and $\tau' = \partial_\xi \tau$. Referring, for example, to the ξ-plan configuration in Figs. 3 and 4 (see discussion in Section 3.4 below), choosing the upper or the lower

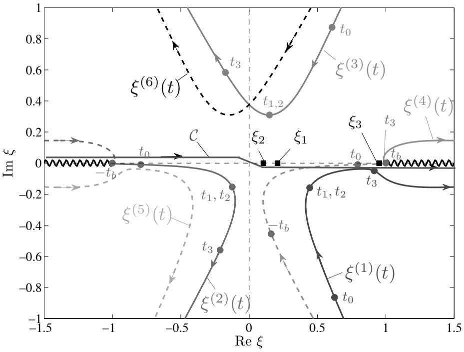

Figure 3: The complex ξ plane of the STT integral (18) for a typical observation point on the lit side of caustic (specifically, this point is displaced horizontally by $\Delta_x = -2.5\,10^{-3}\beta$ from point A in Fig. 2(a) that resides on the caustic). Wiggly lines: branch cuts of ζ separating the upper Riemann sheet (URS) where $\operatorname{Re}\zeta > 0$ from the lower Riemann sheet (LRS) where $\operatorname{Re}\zeta < 0$. $\mathcal{C}$: the integration contour in Eqs. (14) and (18). Square tags: stationary points $\xi_{1,2,3}$ corresponding to rays $r = 1, 2, 3$ in Fig. 1 (for clarity, ray 3 is suppressed in Fig. 1 but it is shown in Fig. 2(a)). $t_{1,2,3}$: ray arrival times. Note that $t_1 \sim t_1$, but $t_3 - t_{1,2} \gg T$. $\xi^{(p)}(t)$, $p = 1, 2, ...6$: trajectories of the 6 poles $\xi(t)$ of (19) as a function of t; poles on the URS and LRS are denoted by solid or dashed lines, respectively. The tags on the trajectories denote values of t there. The poles $p = 1, 3$ are always in the URS; $p = 5, 6$ are always in the LRS; $p = 2, 4$ are located first in the LRS and then cross to the URS. In order to improve visibility, we displaced the poles from the real ξ axis by choosing large T, $T = 10^{-2}\beta/c$, but in the field calculations we used $T = 10^{-6}\beta/c$, yielding the poles map in Fig. 4. Here and in the following figures we used $\alpha = 10^{-5}$.

half plane closure implies that the summation involves the pole $p = 3$ or the poles $p = 1, 2$, respectively. The second term in (20) is the contribution of the branch-cuts $\mathcal{I}_b^{\pm}$ of ζ extending, respectively, along the real ξ-axis segments $\xi \in [1, \infty)$ and $\xi \in (-\infty, -1]$ (wiggly lines in Fig. 3). In (21), the branch-cut integrals have been neglected since they correspond to the evanescent spectrum. Finally, we note that ∂_t can be calculated in a closed-form by noting from (19) that $\partial_t \xi(t) = \{\tau'[\xi(t)]\}^{-1}$.

The result in (21) expresses the field everywhere as an implicit function of space and time. As noted in the Introduction, wavefront approximations near the rays arrival times, expressed explicitly in terms of the space-time coordinates, have been derived in [8].

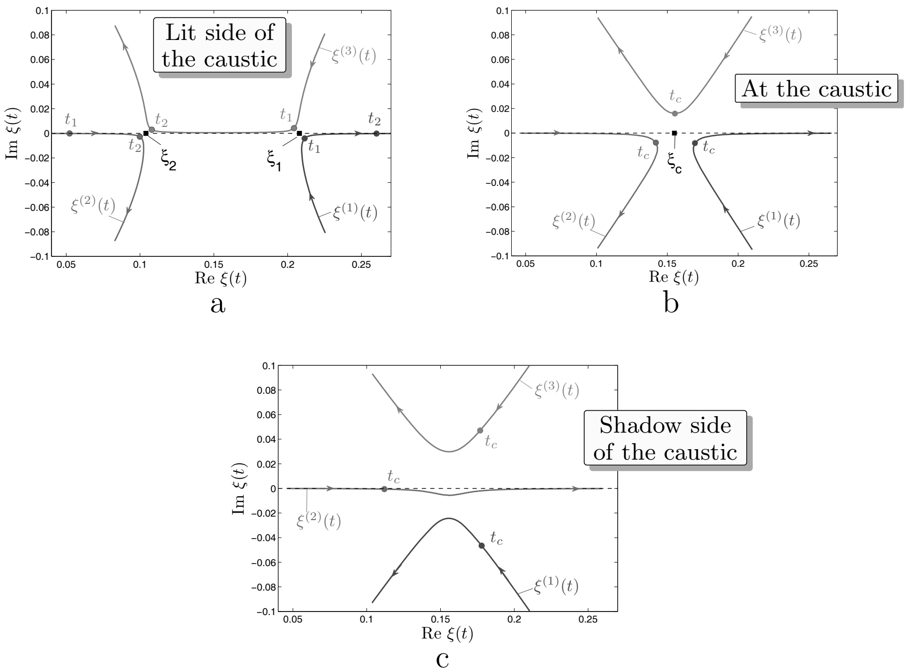

a b

c

Figure 4: Trajectories of the poles $\xi^{(p)}(t)$, $p = 1, 2, 3$ of (19) in the complex ξ plane for observation points near point A of Fig. 2(a) that resides on the caustic. The figure zooms on the spectral zone near the stationary points $\xi_{1,2}$ of Fig. 3 (square tags) and the trajectories are marked by the same numbers and tags as in Fig. 3. Pulse length parameter: $cT/\beta = 10^{-6}$. (a) Observation point on the lit side of the caustic; (b) on the caustic; (c) on the shadow side. Specifically in this figure, the point in (a) is displaced horizontally from A by $\Delta_x = -2.5\,10^{-3}\beta$ and the point in (c) is displaced by $\Delta_x = 2.3\,10^{-4}\beta$. On the caustic, the two stationary points coalesce to a 2nd order stationary point ξ_c and both rays $r = 1, 2$ arrive at $t = t_c$.

3.4 Spectral properties of the STT integral

We start with the properties of $\tau(\xi)$, referring to Fig. 3 which depicts the ξ-plane for a given $\boldsymbol{r}$ on the lit side of the caustic (specifically, near point A of Fig. 2(a) that resides on the caustic). $\tau(\xi)$ has three stationary points, denoted by ξ_r, $r = 1, 2, 3$, shown in Fig. 3 as square tags. $\xi_1 = 0.208$ and $\xi_2 = 0.104$ correspond to rays 1 and 2 in Fig. 1, where ray 1 has not touched the caustic yet while ray 2 has touched it. The aperture exit points of these rays are $x'_1 = -0.043\beta$ and $x'_2 = -0.011\beta$ and the arrival times are $t_1 = 0.3007\beta/c$ and $t_2 = 0.3009\beta/c$.

The stationary point $\xi_3 = 0.951$ corresponds to a ray that emerges from a very remote point $x_3' = -0.9\beta$ in the aperture and propagates almost parallel to the aperture($\xi_3 \lesssim 1$), reaching $\boldsymbol{r}$ at a later time $t_3 = 0.39\beta/c$ (note that $t_1 \approx t_2$ but $t_3 - t_{1,2} \approx 0.09\beta/c \gg T$ where T is typically $\sim 10^{-6}\beta/c$). For clarity, this ray is suppressed in Fig. 1 but it is shown in Fig. 2 where one may see that, unlike rays 1 and 2, it *intersects* the caustic and does not *converge onto it.* It also has a relatively weak contribution due to the $e^{k\alpha x'}$ decay in the aperture (see (1)). This ray is not included in the paraxial approximation (2).

Equation (19) has 6 roots $\xi^{(p)}(t)$, $p = 1, \ldots, 6$, at any given t. Figure 3 depicts their trajectories in the complex ξ-plane as a function of t at the point A referred above. The poles may be located either on the URS or the LRS where they are denoted by solid or dashed trajectories, respectively. The tags on the trajectories indicate the corresponding values of t. The poles $p = 1, 3$ are located always on the URS, while $p = 5, 6$ are always on the LRS. At a very early time, the poles $p = 2, 4$ are located in the LRS and then cross to the URS at $t = \mp t_b$, $t_b > 0$, respectively, never crossing to the LRS again. Note that the trajectories in Fig. 3 are calculated for a wide pulse with $cT = 10^{-2}\beta$ in order to displace the poles from the real ξ axis and to clarify their location with respect to the integration contour $\mathcal{C}$. In practice, however, T is much smaller: in Fig. 4 and henceforth we use $cT = 10^{-6}\beta$.

For $t \approx t_{1,2}$ near the pulse arrival time, the poles $p = 1, 2, 3$ converge to the stationary points $\xi_{1,2}$ in the URS. Figure 4 zooms in on this spectral zone for three observation points: on the lit side of the caustic, on the caustic, and in the shadow side. Each case is characterized by a different arrangement of the stationary points and of the poles, as follows from the different spectral properties of $\tau(\xi)$. One should note though that the overall poles-topology is similar in all three cases, with poles $p = 1, 2$ being in the lower half of the URS with respect to $\mathcal{C}$, while pole $p = 3$ is in the upper half of the URS. Thus, the field in (21) is described by the two poles $p = 1, 2$ if one chooses a lower half plane closure, or by a single pole $p = 3$ if one chooses an upper half plane closure. We also note that at a later time $t = t_b$, the pole $p = 4$ crosses the branch cut and enters the URS near ξ_3, never crossing to the LRS again. However, as mentioned earlier, this contribution is weak and it is beyond the pertinent time window.

3.5 The AiPB field

In view of the discussion in the preceding paragraph, we have calculate the field by using an upper half plane closure in (21) so that the field is given

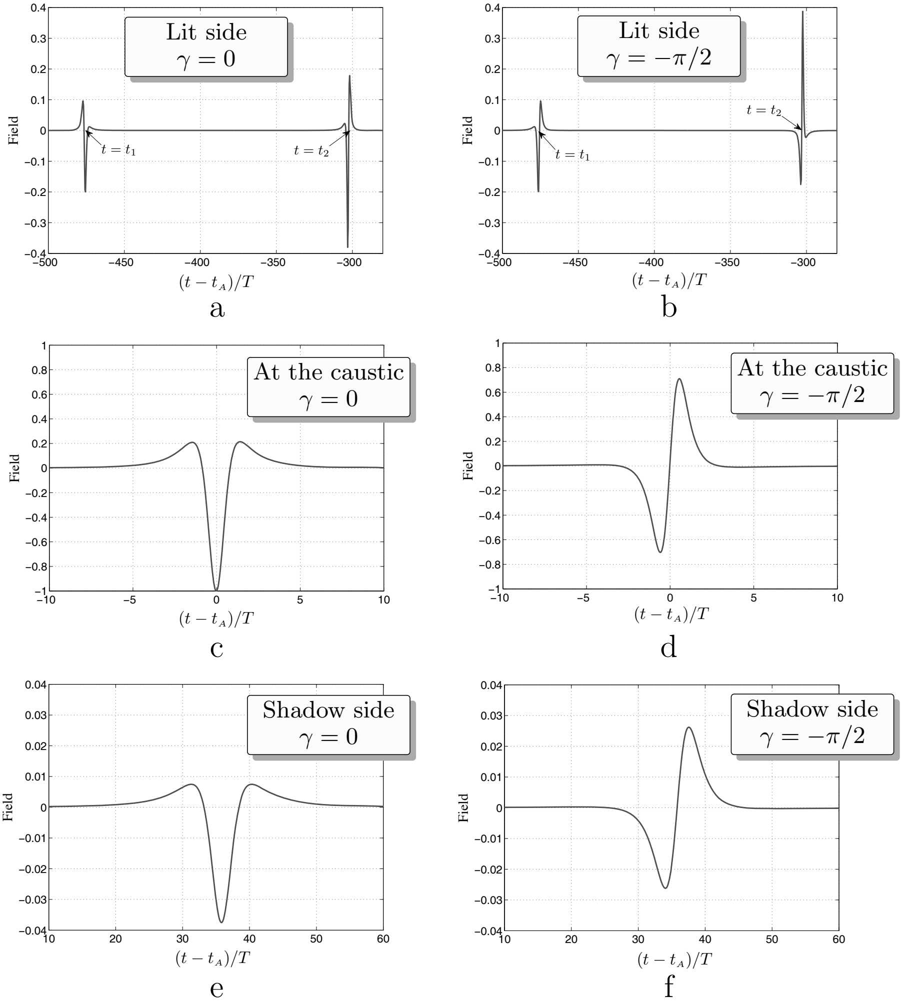

Figure 5: The waveforms near the caustic: (a,b), (c,d) and (e,f) correspond to points on the lit side of the caustic, on the caustic at point A, and on the shadow side, respectively. They are calculated exactly via (21). The temporal signal is (17) with $m = 2$ and $\gamma = 0$ in (a,c,e) or $\gamma = -\pi/2$ in (b,d,f). Note that the waveforms for $\gamma = -\pi/2$ are Hilbert transforms of those for $\gamma = 0$. The time axis is centered around t_A, the arrival time to A, and normalized with respect to T. The field is normalized such that $\max |u| = 1$ on the caustic in (c). Note also the different vertical scales.

by the single pole $p = 3$ in Figs. 3 and 4, viz.

$$\overset{+}{u}(\boldsymbol{r}, t) = -\partial_t^m \frac{A\, e^{\mathrm{i}\gamma}}{\pi\tau'\big[\xi^{(3)}(t)\big]}. \tag{22}$$

Figure 5 depicts the field at the 3 observation points considered in Fig. 4, located near point A in Fig. 2. The temporal signal is given by (17) with $m = 2$ and $\gamma = 0$ in (a,c,e) or $\gamma = -\pi/2$ in (b,d,f). The field is calculated exactly via the real part of (22) (the case $\gamma = -\pi/2$ is the same as taking the imaginary part of (22) for $\gamma = 0$, and it is a Hilbert transform of the case $\gamma = 0$).

On the lit side of the caustic (Figs. 5(a,b)) there are two separate peaks at $t_{1,2}$, which are obtained when this pole passes near the stationary points $\xi_{1,2}$ where τ' vanishes so that $\tau'\left[\xi^{(3)}(t)\right]$ in the denominator of (22) is small. On the caustic (Figs. 5(c,d)), these two peaks coalesce to a stronger peak, obtained when the pole passes near the second order stationary point ξ_c in Fig. 4(b). Finally, on the shadow side of the caustic (Figs. 5(e,f)), the pulse evanesces, as follows also from the fact that the pole $p = 3$ in Fig. 4(c) passes far away from the real ξ axis.

Figure 6 depicts snapshots of the field in the vicinity of points A and B on the caustic, defined in Fig. 2(a). The snapshots are taken at the arrival times at each point. The field on the lit side consists of wavefronts 1 and 2 corresponding to ray species $r = 1$ that converges toward the caustic and ray species $r = 2$ that diverges away from it. Species $r = 1$ originate from points x' in the aperture that are further away from its center and therefore arrive at larger angles with respect to the z-axis. The two species coalesce on

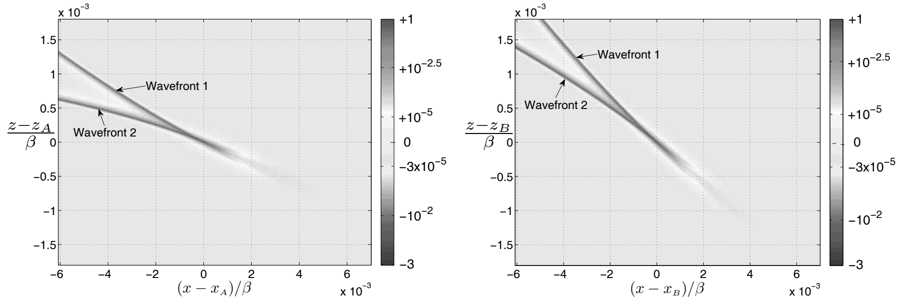

a b

Figure 6: Snapshots of the field near points A (a) and B (b) on the caustic. The snapshots are taken at $t = t_{\mathrm{A,B}}$ denoting the time of arrival at A and B, respectively. The axes are centered around point A and B and are normalized with respect to β. The temporal signal is given by (17) with $m = 2$, $\gamma = 0$, $T = 10^{-6}\beta/c$ and $\alpha = 10^{-5}$. The logarithmic scale retains the sign of the waveform (see the bar), and is normalized with respect to the maximal value in (a). 'Wavefronts 1,2' corresponding to rays species $r = 1, 2$, respectively, coalesce at the caustic with an evanescent contributions on the shadow side.

the caustic generating the strong peak of the beam that follows the curved trajectory. The field on the shadow side decays algebraically, as opposed to the exponential decay in the time-harmonic case. Note also the wavefront rotation as the pulse progresses along the caustic from point A to B, which is due to the bending of the caustic and the fact that rays reaching the caustic at longer ranges arrive at increasingly sharper angles (see Fig. 1).

The resolution of Fig. 6 fails to depict the narrow negative peak of the wavefronts (see Fig. 5). We therefore depict in Figs. 7 cross sectional cuts of the snapshot in Fig. 6(a). The cut in Fig. 7(a) passes exactly through point A, demonstrating the strong peak at the caustic, as opposed to the peaks of the rays in Fig. 7(b).

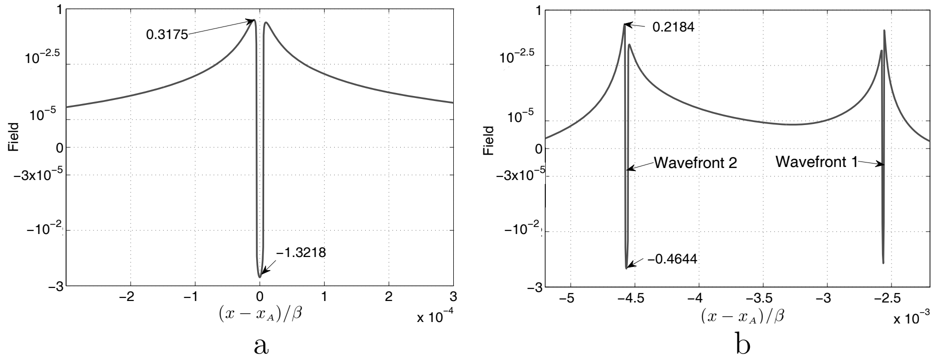

Figure 7: Cross sectional cuts along z =constant lines in Fig. 6(a). (a) Cut passing exactly through A ($z - z_{\mathrm{A}} = 0$); (b) cut along $z - z_{\mathrm{A}} = 0.5\,10^{-3}\beta$.

Figure 8 explores the effect of the parameter α that controls the exponential decay of the aperture field (see (1)). Increasing α affects essentially the $r = 1$ ray species that arrives first, since this species originates from aperture points x' that are located further away from the center and are therefore strongly affected by the exponential decay. Indeed, comparing Figs. 8(a,b) with Figs. 6(a,b) one observes that the field of 'wavefront 1' is weaker and has a longer pulse length. For the same reason, the field becomes weaker as it propagates further away from point A to B.

4 Conclusions

In this paper we discussed the Airy Beams (AiB) and the ultra wide band (UWB) Airy Pulsed Beams (AiPB). We discussed the physical properties of these wave functions and the mathematical techniques that are involved in calculating the solutions in the frequency domain (FD) and in the time domain (TD).

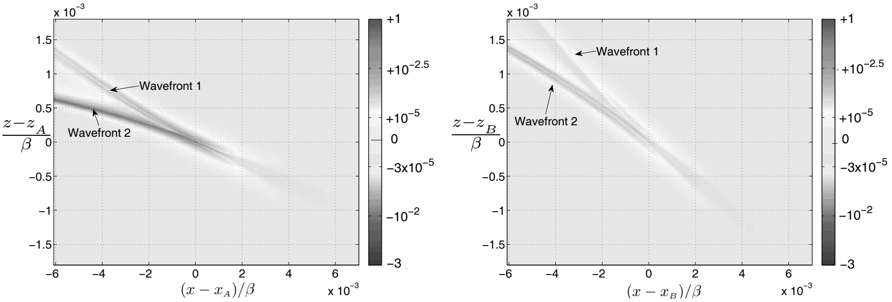

a b

Figure 8: Snapshots of the field near points A (a) and B (b) on the caustic. All parameters are the same as in Fig. 6, except for $\alpha = 10^{-3}$.

We started in Section 2.1 with a ray analysis of the FD solution. The ray representation provides a cogent physical interpretation to the AiB and explains its intriguing properties. The ray formulation, when applied judiciously, is more accurate than the paraxial solution of (2), mainly due to the growing deviation of the paraxial propagation trajectory (3) from the exact trajectory obtained via ray analysis. In particular, the paraxial theory does not predict the cusp in Fig. 2(b) beyond which the AiB disperses. The error of the paraxial solution versus the exact ray solution is studied in [7, Figs. 11 and 12] in the context of the 3D AiB. Note that the error is obtained even at a relatively short range $z \sim 0.16\beta$.

The formulation of the UWB-AiPB solution is based on a frequency scaling of the initial aperture field in (1). This scaling, first introduced in [8], renders the FD AiB solution *non-dispersive* in the sense that the ray skeleton of the field is frequency independent. This ensures that all the frequency components are AiB's that propagate along the same curved trajectory, so that the TD wavepacket does not disperse due to the wide frequency band.

An exact closed-form solution to the AiPB has been derived in Section 3 via the spectral theory of transients (STT). The STT synthesizes the field as a spectral integral of time dependent plane waves. This integral is then evaluated in a closed form and the final result in Eq. (21) expresses the field compactly by tracking the time-dependent spectral poles of the integrand. Actually, the AiPB is expressed in (21) by the contribution of a single pole.

The properties of the AiPB were explored in Section 3.5 via a detailed numerical example. It has been shown that the AiPB indeed propagates along a curved caustic while retaining its field structure. From Fig. 6 one concludes that the AiPB consists of two propagating wavefronts that coalesce on the caustic, generating a strong peak there. The wave mechanism of the AiPB is explained further in Fig. 8 where one may discern that the first arriving wavefront is weaker than the second one. This is due to the fact that this waveform is formed by rays originating from more distant points at the aperture that are affected more strongly by the attenuation parameter α. This demonstrates again that the AiB is, in fact, not a beam field in the sense that it is not described by a local beam dynamics [6]. One also observes that the STT solution applies uniformly through the caustic, from the lit side to the shadow.

The emphasis in this paper has been placed on the exact spectral solution via the STT, which is an extension of the Cagniard–de Hoop (CdH) method. In the CdH approach, the TD solutions are obtained by manipulating the FD spectral integrals into a form from which one may infer the TD solutions ‘by inspection’. Specifically, in that approach the integration contour of the original FD spectral integral are deformed to a CdH contour which is defined by the solution of (19) (with $T\to 0$) with t being a parameter along the CdH contour that increases monotonically from some finite value, say t_0, to infinity. From the solution of Eq. (19) as a function of t shown in Figs. 3 or 4 one readily observes that it is impossible to find a simple deformation of the original integration contour $\mathcal{C}$ to a path whereon the parameter t increases monotonically as explained above. In the STT approach, this difficulty is circumvented by formulating the field as a TD spectral integral and then evaluating this integral by closing the integration contour $\mathcal{C}$ about *all* the relevant singularities in the complex-spectrum plane. The present example demonstrates that the STT is indeed a flexible reformulation of the CdH method.

Acknowledgment

This work is supported in part by the Israeli Science Foundation, under Grant No. 263/11. EH would like to extend his warm thanks to Professor Adrianus T. de Hoop for inspiring discussions on the relation between the CdH method and the STT.

Bibliography

[1] G. A. Siviloglou, J. Broky, A. Dogariu, and D. N. Christodoulides, “Observation of accelerating Airy beams,” *Phys. Rev. Lett.*, vol. 99, pp. 213901-1–213901-4, Nov. 2007.

[2] G. A. Siviloglou and D. N. Christodoulides, “Accelerating finite energy Airy beams,” *Opt. Lett.*, vol. 32, no. 8, pp. 79–981, April 2007.

[3] M. A. Bandres and J. Gutiérrez-Vega, “Airy-Gauss beams and their transformation by paraxial optical systems,” *Opt. Express*, vol. 15, no. 25, pp. 16719–16728, Dec. 2007.

[4] G. A. Siviloglou, J. Broky, A. Dogariu, and D. N. Christodoulides, “Ballistic dynamics of Airy beams,” *Opt. Lett.*, vol. 33, no. 3, pp. 207–209, Feb. 2008.

[5] J. Broky, G. A. Siviloglou, A. Dogariu, and D. N. Christodoulides, “Self-healing properties of optical Airy beams,” *Optics Express*, vol. 16, no. 17, pp. 12880–12891, Aug. 2008.

[6] Y. Kaganovsky and E. Heyman, “Wave analysis of Airy beams,” *Optics Express*, vol. 18, no. 8, pp. 8440–8452, April 2010.

[7] Y. Kaganovsky and E. Heyman, “Non-paraxial wave analysis of 3D Airy beams,” *J. Opt. Soc. Am. A*, vol. 29, no. 5, pp. 671–688, May 2012.

[8] Y. Kaganovsky and E. Heyman, “Airy pulsed beams,” *J. Opt. Soc. Am. A*, vol. 28, no. 6, pp. 1243–1255, June 2011.

[9] E. Heyman and L. B. Felsen, “Weakly dispersive spectral theory of transients (STT), Part I: Formulation and interpretation,” *IEEE Trans. Antennas Propag.*, vol. 35, no. 1, pp. 80–86, Jan. 1987.

[10] E. Heyman and L. B. Felsen, “Weakly dispersive spectral theory of transients (STT), Part II: Evaluation of the spectral integral,” *IEEE Trans. Antennas Propag.*, vol. 35, no. 5, pp. 574–580, May 1987.

[11] E. Heyman, “Weakly dispersive spectral theory of transients (STT), Part III: Applications,” *IEEE Trans. Antennas Propag.*, vol. 35, no. 11, pp. 1258–1266, Nov. 1987.

[12] E. Heyman and L. B. Felsen, “Real and complex spectra – an alternative view of WKBJ seismograms,” *Geophys. J. Roy. Astro. Soc.*, vol. 91, no. 3, pp. 1087–1126, Dec. 1987.

[13] L. Cagniard, *Reflection and Refraction of Progressive Seismic Waves,* (Translation by E. Flinn, C. H. Dix, of *Réflexion et réfraction des ondes séismiques progressives*, Paris, Gauthier-Villars, 1939) New York: McGraw-Hill, 1962.

[14] A. T. de Hoop, “A modification of Cagniard’s method for solving seismic pulse problems,” *Appl. Sci. Res.*, Sect. B, no. 8, pp. 349–356, May 1960.

[15] A. T. de Hoop and H. J. Frankena, “Radiation of pulses generated by a vertical electric dipole above a plane, non-conducting, earth,” *Appl. Sci. Res.*, Sect. B, no. 8, pp. 369–377, May 1960.

[16] E. Heyman and L. B. Felsen, “Gaussian beam and pulsed beam dynamics: complex source and spectrum formulations within and beyond paraxial asymptotics,” *J. Opt. Soc. Am. A*, vol. 18, no. 7, pp. 1588–1610, July 2001.

[17] E. Heyman, “Pulsed beam solutions for propagation and scattering problems,” in *Scattering: Scattering and Inverse Scattering in Pure and Applied Science*, E. R. Pike and P. C. Sabatier (eds.), Academic Press, vol. 1, chap. 1.5.4, pp. 295–315, 2002.

[18] E. Heyman, R. Strachielevitz, and D. Koslof, “Pulsed beam reflection and transmission at a planar interface: Exact solutions and approximate local models,” *Wave Motion*, vol. 18, no. 4, pp. 315–343, Dec. 1993.

[19] R. Ianconescu and E. Heyman, “Pulsed field diffraction by a perfectly conducting wedge: A spectral theory of transient (STT) analysis,” *IEEE Trans. Antennas Propag.*, vol. 42, no. 6, pp. 781–789, June 1994

[20] R. Ianconescu and E. Heyman, “Pulsed beam diffraction by a perfectly conducting wedge. Exact Solution,” *IEEE Trans. Antennas Propag.*, vol. 42, no. 10, pp. 1377–1385, Oct. 1994.

[21] E. Heyman and R. Ianconescu, “Pulsed beam diffraction by a perfectly conducting wedge. Local scattering models,” *IEEE Trans. Antennas Propag.*, vol. 43, no. 5, pp. 519–528, May 1995.

[22] P. Saari, “Laterally accelerating Airy pulses,” *Optics Express*, vol. 16, no. 14, pp. 10303–10308, July 2008.

[23] D. Ludwig, “Wave propagation near a smooth caustic,” *Bull. Amer. Math. Soc.*, vol. 71, no. 5, pp. 776–779, May 1965.

[24] Y. A. Kravtsov, “A modification of the geometrical optics method,” *Izv. VUZ Radiofiz.*, Engl. transl., *Radiophys. Quantum Electron.*, vol. 7, pp. 664–673, 1964.

[25] F. W. J. Olver, D. W. Lozier, R. F. Boisvert, and C. W. Clark, eds., *NIST Digital Library of Mathematical Functions*, http://dlmf.nist.gov/, 2010. Release of 1.0.5 of 2012-10-01.

[26] J. Nye, *Natural Focusing and Fine Structure of Light: Caustics and Wave Dislocations* Philadelphia, PA: Institute of Physics Pub., 1999.

Array-structure theory of Maxwell wavefields in affine $(3+1)$-spacetime: An overview

Adrianus T. de Hoop
Delft University of Technology,
Faculty of Electrical Engineering, Mathematics and Computer Science,
Laboratory of Electromagnetic Research,
Mekelweg 4, 2628 CD Delft, the Netherlands,
e-mail: a.t.dehoop@tudelft.nl

Abstract

An array-structure theory of Maxwell wavefields in affine $(3+1)$-spacetime is presented. The structure is designed to supersede the conventional Gibbs vector calculus and Heaviside vectorial Maxwell equations formulations, deviates from the Einstein view on spacetime as having a metrical structure (with the, non-definite, Lorentz metric), and adheres to the Weyl view where spacetime is conceived as being affine in nature. In the theory, the electric field and source quantities are introduced as one-dimensional arrays and the magnetic field and source quantities as antisymmetrical two-dimensional arrays. Time-convolution and time-correlation field/source reciprocity are discussed, and expressions for the wavefield radiated by sources in an unbounded, homogeneous, isotropic, lossless embedding are derived. These expressions clearly exhibit their structure as convolutions in spacetime. The bookkeeping of the array structure smoothly fits the input requirements of computational software packages. An interesting result of fundamental physical importance is that the 'magnetic charge' appears as a completely antisymmetrical three-dimensional array rather than as a number (as in the Dirac quantum theory of the magnetic monopole). The generalization of the array structure to affine $(N+1)$-spacetime with $N > 3$ is straightforward and is conjectured to serve a purpose in theoretical cosmology. No particular 'orientation' of the observer's spatial reference frame (like the 'right-handedness' in conventional vector calculus) is required.

Pulsed Electromagnetic Fields: Their Potentialities, Computation and Evaluation
I. E. Lager and L. J. Jiang (Eds.).
doi: 10.3233/978-1-61499-230-1-21

1 Introduction

Wave phenomena in macroscopic, classical physics have a number of properties in common that can serve as the basis for constructing the mathematical framework that quantitatively describes their physical behavior in spacetime. In constructing this framework, the views developed by Einstein [1] and Weyl [2] serve as the basic *axioms*. For the intended structure to be acceptable, it should, as a minimum requirement, encompass the special theory of relativity (that interrelates the values of the wavefield and source quantities as they are observed by two observers that are in uniform, rectilinear, relative motion in an unbounded, unstructured background universe ('vacuum') [3] in contrast to which the material world presents itself (Lorentz's theory of electrons [4])). The pertaining basic properties are listed below. For generality, they are expressed in affine $(N+1)$-spacetime $\mathbb{R}^N \times \mathbb{R}$, where the spatial constituent $\mathbb{R}^N$ is an N-dimensional Euclidean space provided with a reference frame that is based on the unit of length handled by the observer, and used to specify the position of observation, and the time constituent $\mathbb{R}$ is a one-dimensional Euclidean space that is based on the unit of time handled by the observer and used to specify the instant of observation.

(1) The physical information in the wave is carried by its two *intensive* field quantities and its two *extensive* field quantities. The intensive field quantities together compose the *area density of power flow* in the wave. The two extensive field quantities together compose the wave's *volume density of field momentum.* In Maxwell fields, the intensive field quantities are denoted as *field strengths*, the extensive field quantities as *flux densities.* The source distributions that generate the wavefield are introduced as *volume densities of electric and magnetic current.* As shown in [3], the framework provides the tools for an axiomatic approach to special relativity in $(N+1)$-spacetime.

(2) In a sourcefree subdomain of spacetime, i.e., a subdomain where the wave motion is left to itself, the spatial rates of change of the two intensive field quantities are counterbalanced by the time rates of change of their dual extensive counterparts. In these equations, the action of sources is incorporated through the introduction, in their right-hand sides, of *source terms* of bounded support in spacetime whose structure is compatible with the structure of the pertaining left-hand sides.

(3) Following Einstein [1] and Weyl [2], the field and source quantities are quantitatively specified through p-dimensional ($p = 0, 1, 2, \ldots$) arrays of arraylength N (the dimension of the spatial constituent of affine

spacetime), containing N^p elements. The basic one-dimensional array is the one that specifies the position of the observer as a function of time.

For the identification of the elements of an array, the subscript notation is used. Lower-case Latin subscripts, with range $1, 2, \ldots, N$, are used for this purpose. The Einstein summation convention is employed to denote the summing over repeated subscripts in a term in an expression. The two-dimensional unit array is $\delta_{m,n}$ with $\delta_{m,n} = 0$ for $m \neq n$ and $\delta_{m,n} = 1$ for $m = n$. Partial differentiation with respect to x_m is denoted by the one-dimensional array ∂_m; ∂_t is a reserved symbol for differentiation with respect to time (Table 1).

Table 1: Observer in $(N+1)$-spacetime.

Position	$\boldsymbol{x} = x_m = \{x_1, \ldots, x_N\} \in \mathbb{R}^N$
Distance	$\lvert\boldsymbol{x}\rvert = (x_1^2 + \cdots + x_N^2)^{1/2} \geqslant 0$
Time	$t \in \mathbb{R}$
Subscript notation, summation convention	
$\lvert\boldsymbol{x}\rvert = (x_m x_m)^{1/2} = (\sum_{m=1}^{N} x_m x_m)^{1/2} \geqslant 0$	
$\delta_{m,n} x_n = x_m, \ \delta_{m,n}\delta_{n,p} = \delta_{m,p}, \ \delta_{m,m} = N$	
Spatial differentiation	
$\partial_m = \partial/\partial x_m$	
Temporal differentiation	
$\partial_t = \partial/\partial t$ (reserved)	

In the present overview, material from the author's basic, open-access publication [5] has been incorporated. Four-dimensional unit arrays that show up in the theory of elastic waves in solids have been introduced, and their properties discussed, in [6].

The material is organized as indicated below.

- The observer in spacetime, array structure of wavefield and source quantities, subscript notation and summation convention (Section 1)
- The Maxwell wavefield equations (Section 2)
- The electromagnetic constitutive relations (Section 3)
- Interface boundary conditions (Section 4)

- Radiation from sources in an unbounded, homogeneous, isotropic medium (Section 5)
- Time-convolution field/source reciprocity (Section 6)
- Time-correlation field/source reciprocity (Section 6)
- Conclusion

2 The Maxwell wavefield equations

In Maxwell wavefield theory, the electric field and source quantities are introduced as one-dimensional arrays, the magnetic field and source quantities as antisymmetric two-dimensional arrays. The resulting area density of power flow and volume density of wave momentum are one-dimensional arrays. The relevant symbols are given in Table 2.

Table 2: Field and source quantities.

E_r	:	electric field strength
D_k	:	electric flux density
J_k	:	volume source density of electric current
$[H_{p,q}]^- = -[H_{q,p}]^-$	:	magnetic field strength
$[B_{i,j}]^- = -[B_{j,i}]^-$	:	magnetic flux density
$[K_{i,j}]^- = -[K_{j,i}]^-$	:	volume source density of magnetic current
$S_m = [H_{m,k}]^- E_k$	:	area density of power flow
$G_i = [B_{i,j}]^- D_j$	:	volume density of electromagnetic momentum

For the antisymmetric part of a two-dimensional array, the notation $[H_{p,q}]^- \stackrel{\text{def}}{=} (H_{p,q} - H_{q,p})/2 = -[H_{q,p}]^-$ is used.

The wavefield equations relate the time rate of change of an extensive field quantity to the spatial rate of change of its 'dual' intensive field counterpart, thus enabling the existence of solutions with a wavelike character. The excitation of such solutions is accommodated in accordance with the (Einstein) requirement that, in a field equation, all terms should be arrays of equal dimensions and array lengths. For the electromagnetic field equations this results into the (Maxwell) field equations (Table 3).

Table 3: Maxwell field equations.

Maxwell field equations	Operation
$\partial_m[H_{m,k}]^- + \partial_t D_k = -J_k$	$\partial_k \Rightarrow\Downarrow^{[1]}$
$[\partial_i E_j]^- + \partial_t[B_{i,j}]^- = -[K_{i,j}]^-$	$\partial_k +$ cyclic $\Rightarrow\Downarrow^{[2]}$
$[\partial_i E_j]^- = (\partial_i E_j - \partial_j E_i)/2$	
Field/source compatibility relations	
$\partial_t \partial_k D_k = -\partial_k J_k$	[1]
$\partial_t[\partial_k[B_{i,j}]^-]^{\circlearrowright} = -[\partial_k[K_{i,j}]^-]^{\circlearrowright}$	[2]
$[\partial_k[B_{i,j}]^-]^{\circlearrowright} = \partial_k[B_{i,j}]^- + \partial_i[B_{j,k}]^- +$ $\partial_j[B_{k,i}]^-$ $(i \neq j \neq k)$	

$$\partial_m[H_{m,k}]^- + \partial_t D_k = -J_k \tag{1}$$

$$[\partial_i E_j]^- + \partial_t[B_{i,j}]^- = -[K_{i,j}]^- \tag{2}$$

in which

$$[\partial_i E_j]^- = (\partial_i E_j - \partial_j E_i)/2 = -[\partial_j E_i]^-. \tag{3}$$

Operating on (1) with ∂_k and noting that $\partial_k \partial_m[H_{m,k}]^- = 0$, we obtain the *electric field/source compatibility relation*

$$\partial_t \partial_k D_k = -\partial_k J_k. \tag{4}$$

Operating on (2) with ∂_k where $k \neq i \neq j$, cyclically permuting the subscripts, and adding the results, we obtain the *magnetic field/source compatibility relation*

$$\partial_t[\partial_k[B_{i,j}]^-]^{\circlearrowright} = -[\partial_k[K_{i,j}]^-]^{\circlearrowright} \tag{5}$$

where

$$[\partial_k[B_{i,j}]^-]^{\circlearrowright} \overset{\text{def}}{=} \partial_k[B_{i,j}]^- + \partial_i[B_{j,k}]^- + \partial_j[B_{k,i}]^- \ (i \neq j \neq k) \tag{6}$$

(see Table 3). Evidently, the condition $i \neq j \neq k$ can only be met if $N \geqslant 3$, which implies that $N = 3$ *is the minimum number of spatial dimensions for which a field structure of the Maxwell type can exist!*

In adherence to the physical concept that the volume densities of current are associated with the (collective) motion of charged particles in a flow in which the conservation of particles holds, [7, Section 19.4] the *volume density of electric charge* is introduced as

$$\rho \overset{\text{def}}{=} -\partial_t^{-1} \partial_k J_k \tag{7}$$

Table 4: Volume density of charge and conservation laws.

	Volume density of charge	Conservation law
Electric	$\rho \overset{\text{def}}{=} -\partial_t^{-1}\partial_k J_k$	$\partial_k J_k + \partial_t \rho = 0$
Magnetic	$\sigma_{i,j,k} \overset{\text{def}}{=} -\partial_t^{-1}[\partial_i[K_{j,k}]^-]^{\circlearrowright}$	$[\partial_i[K_{j,k}]^-]^{\circlearrowright} + \partial_t \sigma_{i,j,k} = 0$
	∂_t^{-1} = time integration	

where ∂_t^{-1} denotes integration with respect to time from the instant of onset of the sources onward. Equation (7) entails the *continuity equation of electric charge*

$$\partial_k J_k + \partial_t \rho = 0. \tag{8}$$

Similarly, the *volume density of magnetic charge* is introduced as

$$\sigma_{i,j,k} \overset{\text{def}}{=} -\partial_t^{-1}[\partial_i[K_{j,k}]^-]^{\circlearrowright} \tag{9}$$

which entails the *continuity equation of magnetic charge*

$$[\partial_i[K_{j,k}]^-]^{\circlearrowright} + \partial_t \sigma_{i,j,k} = 0. \tag{10}$$

(see Table 4). From the procedure, it follows that the volume density of electric charge is a *zero-dimensional array*, i.e., a single number, while the volume density of magnetic charge is a *cyclic symmetrical three-dimensional array*. (Since for $N = 3$ the latter array involves only a single number, the quantity is commonly mistaken to be a scalar charge density.) The array character of the magnetic charge has implications for the Dirac theory of the magnetic 'monopole' [8].

Evidently, the number of unknowns in the field equations is, so far, twice the number of equations. As a consequence, the fundamental physical condition of the *uniqueness* of the solution to the *initial-value problems* is not yet met. This condition requires that, given the physical state of a system at some instant t_0, its *time evolution* into $t > t_0$ should, in a unique manner, follow from the pertaining field equations. To meet this condition, the field equations developed thus far have to be supplemented with the *constitutive relations* that characterize the medium in which the field is present. Standardly, these constitutive relations express the values of the extensive field quantities in terms of the values of the intensive field quantities. For the electromagnetic field, the relevant general necessary and sufficient conditions are, for the most general case, not known. Only sufficient conditions (for a large class of media met in practice) are well-established. These are discussed in the next section.

3 The electromagnetic constitutive relations

In this section, the electromagnetic constitutive relations for the class of *linear, time-invariant, passive, causally* and *locally reacting media* are presented (see Table 5). For this class of media, the uniqueness of the initial-value problem can be proved [9, 10]. Full inhomogeneity, anisotropy and (Boltzmann) relaxation losses [11] are included.

In general, the medium's response consists of an instantaneous part and a time-delayed part (relaxation) [11]. In the Lorentz theory of electrons [4], the instantaneous part of the response is associated with vacuum, while the relaxation is representative for the presence of matter in the background vacuum.

Classic atomic models for the relaxation functions, based on the Lorentz theory of electrons, can be found in [7, Chapter 19]. With $\overset{(t)}{*}$ denoting time

Table 5: Electromagnetic constitutive relations.

<table>
<tr><td colspan="2">Linear | Time-invariant | Locally reacting media</td></tr>
<tr><td>$D_k = \epsilon_{k,r} \overset{(t)}{*} E_r$</td><td>$\epsilon_{k,r}(\boldsymbol{x},t) =$
electric permittivity</td></tr>
<tr><td>$[B_{i,j}]^- = \mu^-_{i,j,p,q} \overset{(t)}{*} [H_{p,q}]^-$</td><td>$\mu^-_{i,j,p,q}(\boldsymbol{x},t) =$
magnetic permeability</td></tr>
<tr><td colspan="2">$\overset{(t)}{*}$ = time convolution</td></tr>
<tr><td colspan="2">Causality</td></tr>
<tr><td colspan="2">$\{\epsilon_{k,r}, \mu^-_{i,j,p,q}\}(\boldsymbol{x},t) = 0$ for $t < 0$</td></tr>
<tr><td colspan="2">Special media</td></tr>
<tr><td colspan="2">Homogeneous</td></tr>
<tr><td colspan="2">$\{\epsilon_{k,r}, \mu^-_{i,j,p,q}\}(\boldsymbol{x},t) = \{\epsilon_{k,r}, \mu^-_{i,j,p,q}\}(t)$</td></tr>
<tr><td colspan="2">Instantaneously reacting</td></tr>
<tr><td colspan="2">$\{\epsilon_{k,r}, \mu^-_{i,j,p,q}\}(\boldsymbol{x},t) = \{\epsilon_{k,r}, \mu^-_{i,j,p,q}\}(\boldsymbol{x})\delta(t)$</td></tr>
<tr><td colspan="2">Isotropic</td></tr>
<tr><td>$\epsilon_{k,r}(\boldsymbol{x},t) = \epsilon(\boldsymbol{x},t)\delta_{k,r}$</td><td>$D_k = \epsilon \overset{(t)}{*} E_k$</td></tr>
<tr><td>$\mu^-_{i,j,p,q}(\boldsymbol{x},t) = \mu^-(\boldsymbol{x},t)\delta_{i,p}\delta_{j,q}$</td><td>$[B_{i,j}]^- = \mu^- \overset{(t)}{*} [H_{i,j}]^-$</td></tr>
<tr><td colspan="2">Vacuum: $c_0 = 299792458$ m/s</td></tr>
<tr><td>$\epsilon(\boldsymbol{x},t) = \epsilon_0\,\delta(t)$</td><td>$\epsilon_0 = (1/c_0^2\,\mu_0)$ F/m</td></tr>
<tr><td>$\mu^-(\boldsymbol{x},t) = 2\,\mu_0\,\delta(t)$</td><td>$\mu_0 = 4\pi{\cdot}10^{-7}$ H/m</td></tr>
</table>

convolution, the pertaining relations are (see Table 5)

$$D_k(\boldsymbol{x},t) = \epsilon_{k,r}(\boldsymbol{x},t) \overset{(t)}{*} E_r(\boldsymbol{x},t) \tag{11}$$

where

$$\epsilon_{k,r}(\boldsymbol{x},t) = \text{electric permittivity} \tag{12}$$

and

$$[B_{i,j}]^-(\boldsymbol{x},t) = \mu^-_{i,j,p,q}(\boldsymbol{x},t) \overset{(t)}{*} [H_{p,q}]^-(\boldsymbol{x},t) \tag{13}$$

where

$$\mu^-_{i,j,p,q}(\boldsymbol{x},t) = \text{magnetic permeability.} \tag{14}$$

We have: for *homogeneous media* $\{\epsilon_{k,r}, \mu^-_{i,j,p,q}\}(\boldsymbol{x},t) = \{\epsilon_{k,r}, \mu^-_{i,j,p,q}\}(t)$; for *instantaneously reacting media* $\{\epsilon_{k,r}, \mu^-_{i,j,p,q}\}(\boldsymbol{x},t) = \{\epsilon_{k,r}, \mu^-_{i,j,p,q}\}(\boldsymbol{x})\delta(t)$; for *isotropic media* $\epsilon_{k,r}(\boldsymbol{x},t) = \epsilon(\boldsymbol{x},t)\delta_{k,r}$ and $\mu^-_{i,j,p,q}(\boldsymbol{x},t) = \mu^-(\boldsymbol{x},t)\delta_{i,p}\delta_{j,q}$, which entails $D_k = \epsilon \overset{(t)}{*} E_k$ and $[B_{i,j}]^- = \mu^- \overset{(t)}{*} [H_{i,j}]^-$, respectively. The vacuum values are $\mu^-(\boldsymbol{x},t) = 2\,\mu_0\,\delta(t)$, with $\mu_0 = 4\pi{\cdot}10^{-7}$ H/m and $\epsilon(\boldsymbol{x},t) = \epsilon_0\,\delta(t)$ with $\epsilon_0 = (1/c_0^2\,\mu_0)$ F/m and $c_0 = 299792458$ m/s.

3.1 Causality and the time Laplace transformation

The properties associated with the causality of the medium's response are most adequately handled via the *time Laplace transformation*

$$\begin{aligned}&\{\hat{\epsilon}_{k,r}, \hat{\mu}^-_{i,j,p,q}\}(\boldsymbol{x},s)\\ &= \int_{t=0}^{\infty} \exp(-st)\{\epsilon_{k,r}, \mu^-_{i,j,p,q}\}(\boldsymbol{x},t)\mathrm{d}t \text{ for } s \in \mathbb{C}, \mathrm{Re}(s) > 0.\end{aligned} \tag{15}$$

The transforms in the left-hand side are *analytic* in the right-half $\{s \in \mathbb{C}, \mathrm{Re}(s) > 0\}$ of the complex s-plane (Fig. 1).

Their limiting values on the imaginary axes of the s-plane yield the *spectral behavior* of the medium's response. The diagram in which $20\log_{10}[|\{\hat{\epsilon}_{k,r}, \hat{\mu}^-_{i,j,p,q}\}(\boldsymbol{x}, 2\pi \mathrm{j} f)|]$, where f is the *frequency*, is plotted against $\log_{10}(f)$ is denoted as the *spectral diagram* or *Bode diagram* [12]. For modeling purposes, the *Debije* and *Lorentz* relaxation functions (Fig. 2) are in use to describe a variety of phenomena.

3.2 Uniqueness of the initial-value problem

There seems not to be a time-domain uniqueness proof of the initial-value (time-evolution) problem for media that show an arbitrary relaxation behavior. The known proof goes via the time Laplace transformed field equations

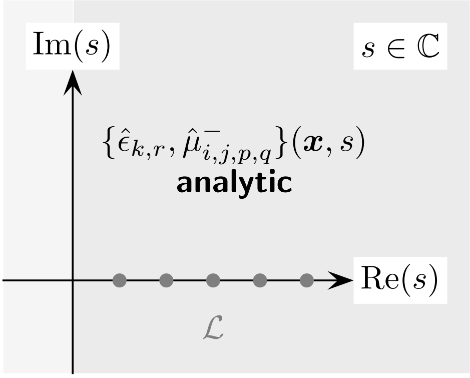

Figure 1: Domain of analyticity and Lerch sequence in the complex time Laplace transform plane.

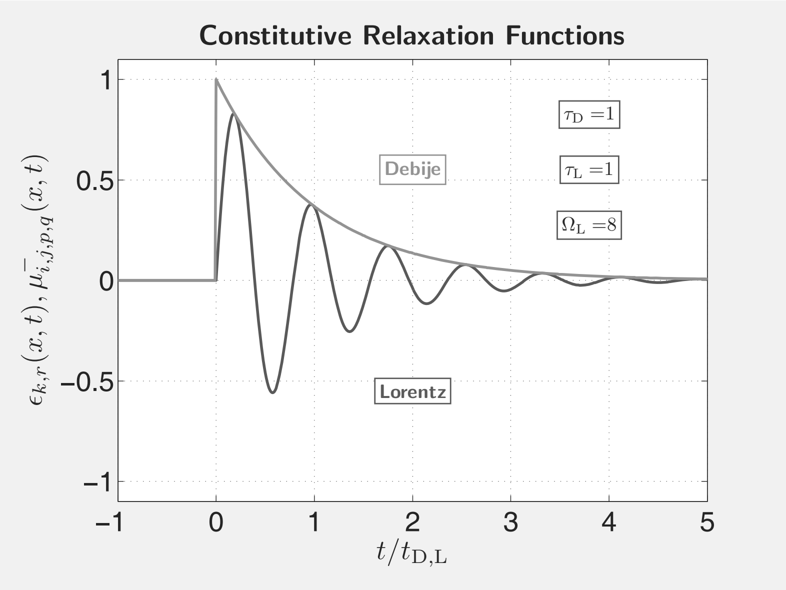

Figure 2: Debije and Lorentz relaxation functions.

and constitutive relations [10] through their properties at the sequence of equidistant values of the transform parameter s (Fig. 1)

$$\mathcal{L} = \{s \in \mathbb{R}; s = s_0 + n\,h, s_0, h > 0, n = 0, 1, 2, \dots\} \text{ (Lerch sequence)} \quad (16)$$

on the positive real s-axis. The corresponding uniqueness in the time domain then follows from Lerch's theorem [13, p. 63].

Sufficient conditions for the uniqueness of the initial-value (time-evolution) problem are (the proof runs parallel to the one presented in [10])

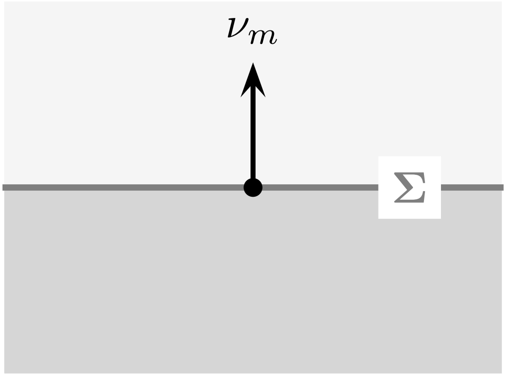

Figure 3: Passive interface between two media with different constitutive parameters.

$$\hat{E}_k\,\hat{\epsilon}_{k,r}\,\hat{E}_r > 0 \text{ for } s \in \mathcal{L}, \text{ and } [\hat{H}_{i,j}]^-\,\hat{\mu}^-_{i,j,p,q}\,[\hat{H}_{p,q}]^- > 0 \text{ for } s \in \mathcal{L} \tag{17}$$

and any nonzero field values. For radiation problems in unbounded domains, a restriction occurs in that outside some sphere of finite radius the medium should be homogeneous and isotropic.

4 Interface boundary conditions

At the passive interface between two media across which the constitutive parameters jump by finite amounts, also the field components show jump discontinuities. Certain components, however, remain continuous. The pertaining continuity conditions follow from the field equations upon decomposing the spatial differentiation ∂_m into a component normal to the interface $(\partial_m)_\perp$ and a component parallel to it $(\partial_m)_\parallel$. Let ν_m denote the unit vector along the normal to the interface, then (Fig. 3)

$$(\partial_m)_\perp = \nu_m(\nu_n \partial_n) \text{ and } (\partial_m)_\parallel = \partial_m - (\partial_m)_\perp \tag{18}$$

If, now, the operation of differentiation perpendicular to the interface would act on a field component that jumps across the interface, this would lead to a Dirac delta distribution operative at the interface and this would violate the assumed physical passivity of the interface. Hence, $(\partial_m)_\perp$ can only act at field components that are continuous across the interface. This consideration leads to the interface boundary conditions (see Table 6)

$$\nu_m[H_{m,k}]^-|^+_- = 0 \tag{19}$$

$$[\nu_i E_j]^-|^+_- = 0. \tag{20}$$

Note that (20) implies $\nu_i[\nu_i E_j]^-|_-^+ = 0$ and, hence, $[E_j - (\nu_i E_i)\nu_j]|_-^+ = 0$ or $(E_j)_{\parallel}|_-^+ = 0$.

Table 6: (Passive) interface boundary conditions.

$\nu_m[H_{m,k}]^-|_-^+ = 0$	$[\nu_i E_j]^-|_-^+ = 0$
Note: $[\nu_i E_j]^-|_-^+ = 0 \Rightarrow \nu_i[\nu_i E_j]^-|_-^+ = 0 \Rightarrow$ $[E_j - (\nu_i E_i)\nu_j]|_-^+ = 0 \Rightarrow (E_j)_{\parallel}|_-^+ = 0$	

5 Radiation from sources in an unbounded homogeneous, isotropic, lossless medium

In this section, the radiation from sources in unbounded $\mathbb{R}^N$, filled with a homogeneous, isotropic and lossless medium is discussed. It will be shown that, in this case, only elementary mathematical operations such as spatial differentiation, temporal differentiation, spatial convolution and temporal convolution are needed to arrive at explicit expressions for the electric and magnetic field components. All of these operations are commutable. Another feature is that the orientation of the spatial reference frame employed (such as the right-handedness in standard Gibbs vector calculus) will turn out to be irrelevant. The source quantities J_k and $[K_{i,j}]^-$ that excite the field will be assumed to have the bounded spatial supports $\mathcal{D}^J \subset \mathbb{R}^N$ and $\mathcal{D}^K \subset \mathbb{R}^N$,respectively. The constitutive coefficients of the medium are $\epsilon > 0$ and $\mu^- > 0$. The electric field strength E_r and the magnetic field strength $[H_{p,q}]^-$ then satisfy the Maxwell equations

$$\partial_m[H_{m,k}]^- + \epsilon\,\partial_t E_k = -J_k \tag{21}$$

$$[\partial_i E_j]^- + \mu^-\,\partial_t[H_{i,j}]^- = -[K_{i,j}]^- \tag{22}$$

with the corresponding source/field compatibility relations

$$\epsilon\,\partial_t\,\partial_k E_k = -\partial_k J_k \tag{23}$$

$$\mu^-\,\partial_t[\partial_k[H_{i,j}]^-]^{\circlearrowright} = -[\partial_k[K_{i,j}]^-]^{\circlearrowright} \quad (i \neq j \neq k). \tag{24}$$

Note that (24) implies that $N \geqslant 3$.

Elimination of $[H_{i,j}]^-$ from (21) and (22) and use of the compatibility relation (23) lead to the *electric-field wave equation*

$$(\partial_m\partial_m)E_k - c^{-2}\partial_t^2 E_k = -Q_k \tag{25}$$

in which

$$c = 1/(2\mu^{-}\,\epsilon)^{1/2} \tag{26}$$

$$Q_k = -2\,\mu^{-}\,\partial_t J_k + (1/\epsilon)\partial_t^{-1}\partial_k(\partial_m J_m) + 2\,\partial_m[K_{m,k}]^{-} \tag{27}$$

where ∂_t^{-1} denotes time integration from the instant of onset of the sources onward. Introducing the *electric-current potential* A_k as the solution of the wave equation

$$(\partial_m\partial_m)A_k - c^{-2}\partial_t^2 A_k = -J_k \tag{28}$$

and the *magnetic current potential* $[\Psi_{i,j}]^{-}$ as the solution of the wave equation

$$(\partial_m\partial_m)[\Psi_{i,j}]^{-} - c^{-2}\partial_t^2[\Psi_{i,j}]^{-} = -[K_{i,j}]^{-} \tag{29}$$

and using the property that, for constant ϵ and μ^{-}, the wave operator $(\partial_m\partial_m) - c^{-2}\partial_t^2$ and the operations ∂_m and ∂_t commute, (25)–(29) lead to

$$E_k = -2\,\mu^{-}\,\partial_t A_k + (1/\epsilon)\partial_t^{-1}\partial_k\partial_m A_m + 2\,\partial_m[\Psi_{m,k}]^{-}. \tag{30}$$

Substituting this result in (22) and using the identity $\partial_m\partial_n[\partial_n[\Psi_{m.k}]^{-}]^{\circlearrowright} = 0$, we arrive at

$$[H_{i,j}]^{-} = -2\,\epsilon\,\partial_t[\Psi_{i,j}]^{-} + (1/\mu^{-})\partial_t^{-1}\partial_m[\partial_m[\Psi_{i,j}]^{-}]^{\circlearrowright} + 2\,[\partial_i A_j]^{-}. \tag{31}$$

Finally, upon introducing the *Green's function*

$$G(\boldsymbol{x},t) = \frac{\delta(t - |\boldsymbol{x}|/c)}{4\pi|\boldsymbol{x}|} \text{ for } \boldsymbol{x} \neq \boldsymbol{0} \tag{32}$$

of the three-dimensional scalar wave equation as the causal solution of

$$(\partial_m\partial_m)G - c^{-2}\partial_t^2 G = -\delta(\boldsymbol{x},t) \tag{33}$$

where $\delta(\boldsymbol{x},t)$ is the $(3+1)$-spacetime Dirac distribution operative at $\boldsymbol{x} = \boldsymbol{0}$ and $t = 0$, and using the property

$$\{J_k, [K_{i,j}]^{-}\}(\boldsymbol{x},t) = \delta(\boldsymbol{x},t) \overset{(\boldsymbol{x})}{*}\overset{(t)}{*} \{J_k, [K_{i,j}]^{-}\}(\boldsymbol{x},t) \tag{34}$$

where $\overset{(\boldsymbol{x})}{*}$ denotes spatial convolution and $\overset{(t)}{*}$ denotes temporal convolution, (29) and (30) lead to the representations

$$\{A_k, [\Psi_{i,j}]^{-}\}(\boldsymbol{x},t) = G(\boldsymbol{x},t) \overset{(\boldsymbol{x})}{*}\overset{(t)}{*} \{J_k, [K_{i,j}]^{-}\}(\boldsymbol{x},t) \tag{35}$$

where the convolutions are extended over the spatio-temporal supports of the pertaining sources.

Equation (35) leads to the well-known *retarded potentials*

$$\{A_k, [\Psi_{i,j}]^{-}\}(\boldsymbol{x},t) = \int_{\mathcal{D}^{J,K}} \frac{\{J_k, [K_{i,j}]^{-}\}(\boldsymbol{x}', t - |\boldsymbol{x} - \boldsymbol{x}'|/c)}{4\pi|\boldsymbol{x} - \boldsymbol{x}'|}\mathrm{d}V(\boldsymbol{x}'). \tag{36}$$

5.1 The far-field approximation

The far-field approximation, with respect to the *reference center* $\boldsymbol{x} = \mathbf{0}$, is the leading term in the expansion of the field expressions as $|\boldsymbol{x}| \to \infty$. With

$$|\boldsymbol{x} - \boldsymbol{x}'| = |\boldsymbol{x}| - \xi_m x'_m + O(|\boldsymbol{x}|^{-1}) \text{ as } |\boldsymbol{x}| \to \infty \tag{37}$$

where

$$\xi_m = x_m / |\boldsymbol{x}| \tag{38}$$

is the unit vector in the direction of observation, we obtain

$$\{A_k, [\Psi_{i,j}]^-\}(\boldsymbol{x}, t) = \frac{\{A_k^\infty, [\Psi_{i,j}^\infty]^-\}(\boldsymbol{\xi}, t - |\boldsymbol{x}|/c)}{4\pi|\boldsymbol{x}|}\left[1 + O(|\boldsymbol{x}|^{-1})\right] \text{ as } |\boldsymbol{x}| \to \infty \tag{39}$$

with

$$\{A_k^\infty, [\Psi_{i,j}^\infty]^-\} = \int_{\mathcal{D}^{JK}} \{J_k, [K_{i,j}]^-\}(\boldsymbol{x}', t + \xi_m x'_m/c)\mathrm{d}V(\boldsymbol{x}'). \tag{40}$$

Observing that

$$\partial_m(\cdot) = -(\xi_m/c)\partial_t(\cdot)\left[1 + O(|\boldsymbol{x}|^{-1})\right] \text{ as } |\boldsymbol{x}| \to \infty \tag{41}$$

the far-field approximations for the field strengths are obtained as

$$\begin{aligned}&\{E_r, [H_{p,q}]^-\}(\boldsymbol{x}, t)\\ &= \frac{\{E_r^\infty, [H_{p,q}^\infty]^-\}(\boldsymbol{\xi}, t - |\boldsymbol{x}|/c)}{4\pi|\boldsymbol{x}|}\left[1 + O(|\boldsymbol{x}|^{-1})\right] \text{ as } |\boldsymbol{x}| \to \infty\end{aligned} \tag{42}$$

in which

$$E_r^\infty = -2\,\mu^-(\delta_{r,k} - \xi_r\xi_k)\partial_t A_k^\infty - 2\,(\xi_m/c)\partial_t[\Psi_{m,r}^\infty]^- \tag{43}$$

$$[H_{i,j}^\infty]^- = -2\,\epsilon\,(\partial_t[\Psi_{i,j}^\infty]^- - \xi_m[\xi_m\partial_t[\Psi_{i,j}^\infty]^-]^{\circlearrowright}) - 2\,[(\xi_i/c)\partial_t A_j^\infty]^-. \tag{44}$$

Note that the far-field spherical wave amplitudes satisfy the local *plane-wave relations*

$$(-\xi_m/c)[H_{m,k}^\infty]^- + \epsilon\,E_k^\infty = 0 \tag{45}$$

$$[(-\xi_i/c)E_j^\infty]^- + \mu^-\,[H_{i,j}^\infty]^- = 0 \tag{46}$$

for a wave traveling in the direction of $\boldsymbol{\xi}$.

The field expressions discussed in this section quantify all sorts of wave propagation from source to receiver, such as the radiation from antennas with known source distributions. In *inverse source and scattering problems* they form the basis for the extraction of the (unknown) source distributions from measured wavefield values in some appropriate subdomain of spacetime. The relevant computational procedures are at the heart of all *wavefield imaging* techniques, both in medical diagnostics and in the prospecting for fossil energy reservoirs in the subsurface of the Earth [14].

6 Time-convolution field/source reciprocity

Reciprocity theorems belong to the category of most fundamental theorems in wave physics. As has been discussed in [15] and [14], various particular cases can be considered as the basis for such computational techniques as the domain integral equations method, the boundary integral equations method, the method of moments, while the concept of introducing the different point-source solutions (Green's functions) leads to such results as Huygens' principle and the Oseen–Ewald extinction theorem (related to the null-field method) and the source-to-receiver data transfer in imaging and constitutive parameter inversion procedures.

Reciprocity deals with the interaction of two states, both of which can exist in a certain domain $\mathcal{D} \subset \mathbb{R}^N$ in space. The two states are associated with, in general, different excitations and are present in, in general, media with different constitutive properties, and, hence, exhibit different field values. The category of configurations for which reciprocity will be discussed is the same as the one for which uniqueness of the time evolution can be proved, i.e., for time-invariant configurations with piecewise continuous, linear, time-invariant, passive, locally and causally reacting media (Section 3). For such configurations, two types of reciprocity relation can be distinguished [7, Sections 28.2, 28.3], viz. the one of the *time-convolution type*, where the interaction between the two states involves their time convolution, and the one of the *time-correlation type*, where the interaction between the two states involves their time correlation. In this respect, it is of importance to observe that the time-convolution one preserves *causality*, whereas the time-correlation one has no such property. This distinction plays an important role in case the theorems are applied to unbounded domains. The time-correlation one leads, for zero correlation time and applied to two identical states, to the energy theorem.

The two interacting states are indicated by the superscripts A an B. The field equations applying to State A are

$$\partial_m[H^A_{m.k}]^- + \partial_t(\epsilon^A_{k,r} \overset{(t)}{*} E^A_r) = -J^A_k \tag{47}$$

$$[\partial_i E^A_j]^- + \partial_t(\mu^{-;A}_{i,j,p,q} \overset{(t)}{*} [H^A_{p,q}]^-) = -[K^A_{i,j}]^-. \tag{48}$$

The field equations applying to State B are

$$\partial_m[H^B_{m.r}]^- + \partial_t(\epsilon^B_{r,k} \overset{(t)}{*} E^B_k) = -J^B_r \tag{49}$$

$$[\partial_p E^B_q]^- + \partial_t(\mu^{-;B}_{p,q,i,j} \overset{(t)}{*} [H^B_{i,j}]^-) = -[K^B_{p,q}]^-. \tag{50}$$

Upon carrying out the operation

$$(47) \overset{(t)}{*} E^B_k - (48) \overset{(t)}{*} [H^B_{i,j}]^- - (49) \overset{(t)}{*} E^A_r + (50) \overset{(t)}{*} [H^A_{p,q}]^-$$

we arrive at the *local form* of the *time-convolution reciprocity relation*

$$\partial_m S^{AB}_m + \partial_t U^{AB} = W^{AB} \tag{51}$$

in which

$$S^{AB}_m = [H^A_{m,k}]^- \overset{(t)}{*} E^B_k - [H^B_{m,r}]^- \overset{(t)}{*} E^A_r \tag{52}$$

represents the transfer of field interaction,

$$\begin{aligned} U^{AB} = {} & E^B_k \overset{(t)}{*} (\epsilon^A_{k,r} - \epsilon^B_{r,k}) \overset{(t)}{*} E^A_r - \\ & [H^B_{i,j}]^- \overset{(t)}{*} (\mu^{-;A}_{i,j,p,q} - \mu^{-;B}_{p,q,i,j}) \overset{(t)}{*} [H^A_{p,q}]^- \end{aligned} \tag{53}$$

yields the contrast-in-media interaction and

$$\begin{aligned} W^{AB} = {} & -(E^B_k \overset{(t)}{*} J^A_k - E^A_r \overset{(t)}{*} J^B_r - \\ & [H^B_{i,j}]^- \overset{(t)}{*} [K^A_{i,j}]^- + [H^A_{p,q}]^- \overset{(t)}{*} [K^B_{p,q}]^-) \end{aligned} \tag{54}$$

represents the field/source interaction.

Upon integrating (51) over a bounded domain $\mathcal{D} \subset \mathbb{R}^N$ (Fig.4) and applying Gauss' theorem, we arrive at the global time convolution reciprocity relation (for the spatial domain $\mathcal{D}$) as

$$\int_{\partial\mathcal{D}} \nu_m S^{AB}_m \mathrm{d}A + \partial_t \int_{\mathcal{D}} U^{AB} \mathrm{d}V = \int_{\mathcal{D}} W^{AB} \mathrm{d}V \tag{55}$$

in which $\mathcal{D}$ is the boundary of $\mathcal{D}$ and ν_m is the unit vector along the outward normal to $\partial\mathcal{D}$.

The further discussion of corollaries of (55) goes along the same lines as in [7, Section 28.2], see also [5]. In computational electromagnetics, (55) provides an important check on the consistency of the pertaining numerical codes.

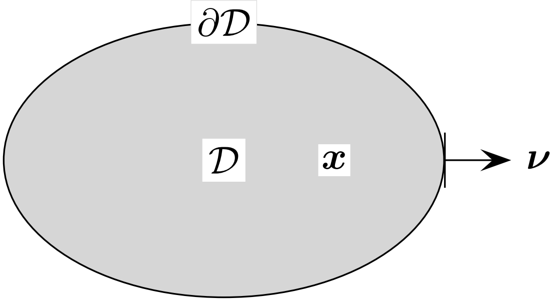

Figure 4: Configuration of application of the global time-convolution reciprocity relation.

7 Time-correlation field/source reciprocity

The time-correlation reciprocity relation is most easily arrived at by writing the time correlation of two of the pertaining quantities as their time convolution, where the second of the two quantities is replaced by its *time-reversed* one. Denoting the operation of time reversal by the superscript *, we start from the field equations applying to State A as

$$\partial_m[H^A_{m.k}]^- + \partial_t(\epsilon^A_{k,r} \overset{(t)}{*} E^A_r) = -J^A_k \tag{56}$$

$$[\partial_i E^A_j]^- + \partial_t(\mu^{-;A}_{i,j,p,q} \overset{(t)}{*} [H^A_{p,q}]^-) = -[K^A_{i,j}]^-. \tag{57}$$

State B applies to the time-reversed field that satisfies

$$\partial_m[H^{B*}_{m.r}]^- - \partial_t(\epsilon^{B*}_{r,k} \overset{(t)}{*} E^{B*}_k) = -J^{B*}_r \tag{58}$$

$$[\partial_p E^{B*}_q]^- - \partial_t(\mu^{-;B*}_{p,q,i,j} \overset{(t)}{*} [H^{B*}_{i,j}]^-) = -[K^{B*}_{p,q}]^-. \tag{59}$$

Upon carrying out the operation

$$(56) \overset{(t)}{*} E^{B*}_k + (57) \overset{(t)}{*} [H^{B*}_{i,j}]^- + (58) \overset{(t)}{*} E^A_r + (59) \overset{(t)}{*} [H^A_{p,q}]^-$$

we arrive at the *local form* of the *time-convolution reciprocity relation*

$$\partial_m S^{AB*}_m + \partial_t U^{AB*} = W^{AB*} \tag{60}$$

in which

$$S^{AB*}_m = [H^A_{m,k}]^- \overset{(t)}{*} E^{B*}_k + [H^{B*}_{m,r}]^- \overset{(t)}{*} E^A_r \tag{61}$$

represents the transfer of field interaction,

$$\begin{aligned} U^{AB*} = {} & E_k^{B*} \overset{(t)}{*} (\epsilon_{k,r}^{A} - \epsilon_{r,k}^{B*}) \overset{(t)}{*} E_r^{A} + \\ & [H_{i,j}^{B*}]^{-} \overset{(t)}{*} (\mu_{i,j,p,q}^{-;A} - \mu_{p,q,i,j}^{-;B*}) \overset{(t)}{*} [H_{p,q}^{A}]^{-} \end{aligned} \tag{62}$$

yields the contrast-in-media interaction and

$$\begin{aligned} W^{AB*} = {} & -(E_k^{B*} \overset{(t)}{*} J_k^{A} + E_r^{A} \overset{(t)}{*} J_r^{B*} + \\ & [H_{i,j}^{B*}]^{-} \overset{(t)}{*} [K_{i,j}^{A}]^{-} + [H_{p,q}^{A}]^{-} \overset{(t)}{*} [K_{p,q}^{*} B]^{-}) \end{aligned} \tag{63}$$

represents the field/source interaction.

Upon integrating (60) over a bounded domain $\mathcal{D} \subset \mathbb{R}^N$ (Fig. 5) and applying Gauss' theorem, we arrive at the global time-correlation reciprocity relation (for the spatial domain $\mathcal{D}$) as

$$\int_{\partial\mathcal{D}} \nu_m S_m^{AB*} \mathrm{d}A + \partial_t \int_{\mathcal{D}} U^{AB*} \mathrm{d}V = \int_{\mathcal{D}} W^{AB*} \mathrm{d}V \tag{64}$$

in which $\mathcal{D}$ is the boundary of $\mathcal{D}$ and ν_m is the unit vector along the outward normal to $\partial\mathcal{D}$.

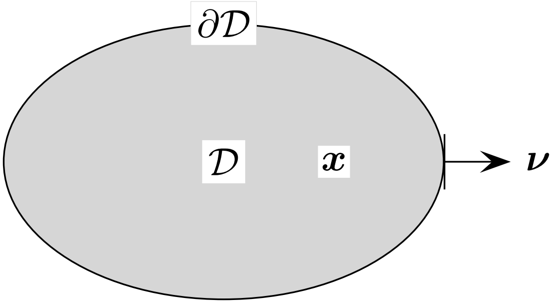

Figure 5: Configuration of application of the global time-correlation reciprocity relation.

The further discussion of corollaries of (64) goes along the same lines as in [7, Section 28]. In computational electromagnetics, (64), too, provides an important check on the consistency of the pertaining numerical codes.

The field/source reciprocity relation discussed in this section plays, in particular, a role in *inverse source and scattering problems* as they turn up in wavefield imaging techniques, employed in medical diagnostics and the prospecting for, and evaluation of, fossil energy reservoirs in the subsurface of the Earth [14,16].

8 Conclusion

A time-domain array-structure approach to electromagnetic field theory is shown to lead to considerable simplifications in the presentation over the traditional one. Through the structure, the standard Gibbs vector calculus and the Heaviside vector form of the Maxwell field equations prove to be a completely superfluous vehicle and even the right-handedness of the spatial coordinate systems employed, turns out to be not a necessity. Only elementary mathematical operations are needed to formulate the theory, which enables its generalization to $(N+1)$-spacetime [3]. The structure introduces magnetic currents and their associated magnetic charges in a manner that deviates from what is standard, with the particular outcome that the magnetic charge is not a scalar (as it is treated in Dirac's theory), but a cyclically symmetric three-dimensional array. In its turn, this has consequences for string theory in quantum electrodynamics and theoretical cosmology [17].

Bibliography

[1] A. Einstein, *The Meaning of Relativity*, Princeton NJ: Princeton University Press, 1955.

[2] H. Weyl. *Space, Time, Matter*, (First American Prining of the Fourth Edition), New York, NY: Dover Publications, 1922.

[3] A. T. de Hoop, "Lorentz-covariant electromagnetic fields in $(N+1)$-spacetime – an axiomatic approach to special relativity," *Wave Motion*, no. 49, pp. 737–744, 2012, [Online]. Available: doi:10.1016/j.wavemoti.2012.05.002.

[4] H. A. Lorentz, *The Theory of Electrons and its Applications to the Phenomena of Light and Radiant Heat*, Leipzig: Teubner, 1916.

[5] A. T. de Hoop, "Electromagnetic field theory in $(N+1)$-space-time: A modern time-domain tensor/array introduction," *Proc. IEEE*, no. 99, pp. 1–17, 2012, [Online]. Available: doi:10.1109/LPROC.2011.2179909.

[6] A. T. de Hoop, A. Abubakar, and T. M. Habashy. "The contrast-source stress-velocity integral-equation formulation of time-domain elastodynamic scattering problems: A structured approach using tensor partitioning," *J. Acoust. Soc. Am.*, vol. 126, no. 3, pp. 1095–1100, Sept. 2009.

[7] A. T. de Hoop, *Handbook of Radiation and Scattering of Waves*, London: Academic Press, 1995, xxx + 1085 pp.; electronic reproduction (with corrections) 2008, freely downloadable, for private use, from http://www.atdehoop.com.

[8] P. A. M. Dirac. "Quantized singularities in the electromagnetic field," *Proc. R. Soc. Lond. A*, no. 133, pp. 60–72, 1931.

[9] A. T. de Hoop, "The initial-value problems in acoustics, elastodynamics and electromagnetics," *Wave Motion*, vol. 23, no. 2, pp. 121–137, March 1996.

[10] A. T. de Hoop, "A time-domain uniqueness theorem for electromagnetic wavefield modeling in dispersive, anisotropic media," *The Radio Science Bulletin, URSI*, no. 305, pp. 17–21, June 2003.

[11] L. Boltzmann. "Zur Theorie der elastischen Nachwirkung," *Poggendorff's Annalen der Physik und Chemie*, vol. 7, pp. 624–654, 1876.

[12] H. W. Bode, *Network Analysis and Feedback Amplifier Design*, 13 edition, New York, NY: Van Nostrand, 1929.

[13] D. V. Widder. *The Laplace Transform*, Princeton NJ: Princeton University Press, 1946.

[14] P. M. van den Berg, H. Blok, and J. T. Fokkema, (editors), *Wavefields and Reciprocity. Proceedings of a Symposium held in honour of Professor dr. A. T. de Hoop, November 20–21, 1996, Delft, the Netherlands*, Delft, the Netherlands: Delft University Press, 1996.

[15] A. T. de Hoop, "Reciprocity, discretization, and the numerical solution of direct and inverse electromagnetic radiation and scattering problems," *Proc. IEEE*, vol. 79, no. 10, pp. 1421–1430, Oct. 1991.

[16] R. Snieder, K. Wapenaar, and U. Wegler, "Unified Green's function retrieval by cross-correlation; connection with energy principles," *Physical Review E (Statistical, Nonlinear, and Soft Matter Physics)*, no. 75, 036103, 2007.

[17] B. P. Kosyakov. "Electromagnetic radiation in even-dimensional spacetime," *Int. J. Mod. Phys*, vol. 23, no. 29, pp. 4695–4708, Nov. 2008, [Online]. Available: doi: 10.1142/S0217751X08041451.

Reducing computational workload from electrically large quadratic surface at high frequency

Yu Mao Wu[†] **Weng Cho Chew**[‡,†] and **Li Jun Jiang**[†]

[†] *Department of Electrical and Electronic Engineering,*
The University of Hong Kong, Pokfulam Road, Hong Kong, China,
e-mail: yumaowu@hku.hk

[‡] *Department of Electrical and Computer Engineering,*
University of Illinois at Urbana-Champaign, USA, 61801

Abstract

In this paper, we propose a frequency independent approach, the numerical steepest descent path method, for computing the physical optics scattered electromagnetic field on the quadratic parabolic and saddle surfaces. Due to the highly oscillatory nature of the physical optics integral in the high frequency regime, the proposed method relies on deforming the integration path of the integral into the numerical steepest descent path on the complex plane. Furthermore, critical-point contributions which contain the stationary phase point, boundary resonance points, and vertex points, are comprehensively studied in terms of the numerical steepest descent path method. To illustrate the efficiency of the proposed method, some extensive numerical results for the physical optics integral defined on arbitrary lines, triangles and polygonal domains are demonstrated. Finally, numerical results on these quadratic surfaces illustrate that the proposed numerical steepest descent path method is frequency independent in computational cost and error controllable in accuracy.

1 Introduction

In electromagnetics (EM), when the product of the external wave frequency k and the size of the considered object L, i.e., kL ranges from tens

---

Pulsed Electromagnetic Fields: Their Potentialities, Computation and Evaluation
I. E. Lager and L. J. Jiang (Eds.).
doi: 10.3233/978-1-61499-230-1-41

to thousands, the analysis of the scattered EM field belongs to the high frequency regime problem. In this case, the classical *physical optics* (PO) current approximation [1, 2], has been accepted as an efficient way to capture the scattered EM field. Given the incident magnetic field $\boldsymbol{H}^{(i)}(\boldsymbol{r})$, the induced PO current on the surface of the considered object $\partial\Omega \subset \mathbb{R}^3$ is represented by

$$\boldsymbol{J}_{\mathrm{PO}}(\boldsymbol{r}) = \begin{cases} \hat{\boldsymbol{n}}(\boldsymbol{r}) \times \boldsymbol{H}^{(i)}(\boldsymbol{r}), & \boldsymbol{r} \in \partial\Omega_1 \\ 0, & \boldsymbol{r} \in \partial\Omega_2 \end{cases} \tag{1}$$

with $\partial\Omega = \partial\Omega_1 \bigcup \partial\Omega_2$, $\partial\Omega_1$ and $\partial\Omega_2$ are the lit and shadow regions of $\partial\Omega$, respectively. The resultant PO scattered electric field $\boldsymbol{E}^{(s)}(\boldsymbol{r})$ is

$$\boldsymbol{E}^{(s)}(\boldsymbol{r}) = \mathrm{i}\omega\mu \int_{\partial\Omega} \bar{\boldsymbol{G}}(\boldsymbol{r}, \boldsymbol{r'}) \cdot \boldsymbol{J}_{\mathrm{PO}}(\boldsymbol{r'})\, \mathrm{d}S(\boldsymbol{r'}) \tag{2}$$

where $\bar{\boldsymbol{G}}(\boldsymbol{r}, \boldsymbol{r'}) = \left(\bar{\boldsymbol{I}} + \frac{\nabla\nabla}{k^2}\right) \frac{\exp\left(\mathrm{i}k|\boldsymbol{r}-\boldsymbol{r'}|\right)}{4\pi|\boldsymbol{r}-\boldsymbol{r'}|}$ is the dyadic Green's function [3] for the electric field in an unbounded medium. Moreover, when kL is large enough, $\boldsymbol{E}^{(s)}(\boldsymbol{r})$ in (2) can be represented as three surface integrals [4]

$$I(\boldsymbol{r}) = \int_{\partial\Omega} s(\boldsymbol{r}, \boldsymbol{r}') \exp\left[\mathrm{i}kv(\boldsymbol{r}')\right] \mathrm{d}S(\boldsymbol{r}'). \tag{3}$$

They are called the *surface PO integrals*. From the mathematical point of view, the PO integrand contains the slowly varying amplitude term $s(\boldsymbol{r}, \boldsymbol{r}')$, and the exponential of the phase function term $\exp\left[\mathrm{i}kv(\boldsymbol{r}')\right]$ giving the highly oscillatory behavior. It is quite changeling to efficiently calculate the PO integral in the high frequency regime.

In computational electromagnetic (CEM) community, the traditional method of moment method (MOM) [6] by Harrington via *surface integral equation* has a workload that grows dramatically with the working frequency as $O\left[(kL)^4\right]$. The efficient *multi level fast multipole algorithm* (MLFMA) developed by Chew [7] makes the computational effort reduce to $O\left[(kL)^2 \log(kL)\right]$. However, in the high frequency regime, the computational effort is still too high to afford. In contrast to these full wave methods like MOM and MLFMA, the PO approximation in (1) has been adopted as an efficient way to capture the scattered field from the large scale object [2,8]. The traditional *high frequency asymptotic* (HFA) approach [9–11], can provide the calculation of the PO scattered field with frequency independent workload. By the HFA method, the PO integrand is approximated by several leading terms. However, the generated PO results lose accuracy due to that kind of approximation, especially when kL is not extremely large but lies in the high frequency regime. The *numerical steepest descent path*

(NSDP) approach [13–16], provides an efficient way to evaluate the highly oscillatory PO integral. On invoking the NSDP method, the original PO *real* integration path is deformed into the *complex* NSDPs on the complex plane. In this manner, the PO integrands decay exponentially on the complex NSDPs, and it can be integrated with workload independent of frequency. In contrast to the HFA method, the only approximation done is the numerical integration of the exponential decay PO integrand. Hence, the proposed NSDP method improves the PO scattered field accuracy.

2 PO surface integral formulation

When a perfect conducting object is excited by an external source, the electromagnetic (EM) scattered fields can be expressed by the Stratton-Chu integral formulas [3]. For the observation point far away from the considered object, the far scattered electric field is expressed as

$$\boldsymbol{E}_s(\boldsymbol{r}) \approx -\frac{\mathrm{i}kZ_0 \exp(\mathrm{i}kr)}{4\pi r} \hat{\boldsymbol{r}} \times \hat{\boldsymbol{r}} \times \int_{\partial\Omega} \left[\hat{\boldsymbol{n}}(\boldsymbol{r}') \times \boldsymbol{H}(\boldsymbol{r}')\right] \exp\left(-\mathrm{i}k\hat{\boldsymbol{r}} \cdot \boldsymbol{r}'\right) \mathrm{d}S(\boldsymbol{r}') \tag{4}$$

where $\partial\Omega$ is the boundary of the object, k is the wave number outside Ω, ω is the angular frequency, $\boldsymbol{r}$ is the observation point with the amplitude r and unit vector $\hat{\boldsymbol{r}}$, $\boldsymbol{r}'$ is the surface point on $\partial\Omega$, $\hat{\boldsymbol{n}}(\boldsymbol{r}')$ is the outward unit normal vector of $\partial\Omega$, Z_0 is the free space intrinsic impedance constant. EM fields are time harmonic with the time dependence $\exp(-\mathrm{i}\omega t)$. For notation simplification, in the following, we still use $\partial\Omega$ to represent the lit region of the considered object. $\boldsymbol{H}^{(i)}(\boldsymbol{r}')$ is the incident magnetic field on $\partial\Omega$. In particular, we choose the plane incident wave

$$\boldsymbol{E}^{(i)}(\boldsymbol{r}) = \boldsymbol{E}_0^{(i)} \exp\left(\mathrm{i}k\hat{\boldsymbol{r}}^{(i)} \cdot \boldsymbol{r}\right) \tag{5}$$

$$\boldsymbol{H}^{(i)}(\boldsymbol{r}) = \frac{\hat{\boldsymbol{r}}^{(i)} \times \boldsymbol{E}_0^{(i)}}{Z_0} \exp\left(\mathrm{i}k\hat{\boldsymbol{r}}^{(i)} \cdot \boldsymbol{r}\right). \tag{6}$$

Then, after substituting (1), (5) and (6) into (4), the far scattered electric field can be represented by a surface integral

$$\boldsymbol{E}_s(\boldsymbol{r}) \approx \int_{\partial\Omega} \boldsymbol{s}_{\mathrm{bi}}(\boldsymbol{r}') \exp\left[\mathrm{i}kv_{\mathrm{bi}}(\boldsymbol{r}')\right] \mathrm{d}S(\boldsymbol{r}') \tag{7}$$

with

$$\boldsymbol{s}_{\mathrm{bi}}(\boldsymbol{r}') = -\frac{\mathrm{i}k\exp(\mathrm{i}kr)}{2\pi r}\,\hat{\boldsymbol{r}} \times \hat{\boldsymbol{r}} \times \left[\hat{\boldsymbol{n}}(\boldsymbol{r}') \times \hat{\boldsymbol{r}}^{(i)} \times \boldsymbol{E}_0^{(i)}\right] \tag{8}$$

$$v_{\mathrm{bi}}(\boldsymbol{r}') = \left(\hat{\boldsymbol{r}}^{(i)} - \hat{\boldsymbol{r}}\right) \cdot \boldsymbol{r}'. \tag{9}$$

The equation above is the bistatic scattered electric field under the PO approximation, which is called the PO integral. $\boldsymbol{E}_0^{(i)}$ in (5) and (6) is the incident electric polarization wave vector. In (8) and (9), $\boldsymbol{s}_{\mathrm{bi}}(\boldsymbol{r}')$ is the vector amplitude function which is usually slowly varying when the surface of the object is smooth. The exponential of the phase function term, $\exp\left[\mathrm{i}kv_{\mathrm{bi}}(\boldsymbol{r}')\right]$, will become highly oscillatory as the working frequency k increases.

In particular, for the monostatic case with $\hat{\boldsymbol{r}} = -\hat{\boldsymbol{r}}^{(i)}$, the PO surface integral in (7) can be represented as

$$\boldsymbol{E}_s(\boldsymbol{r}) \approx \boldsymbol{E}_0^{(i)} \tilde{I}_{\mathrm{mono}}, \tag{10}$$

with

$$\tilde{I}_{\mathrm{mono}} = \int_{\partial\Omega} s_{\mathrm{mono}}(\boldsymbol{r}') \exp\left[\mathrm{i}kv_{\mathrm{mono}}(\boldsymbol{r}')\right] \mathrm{d}S(\boldsymbol{r}'), \tag{11}$$

$$s_{\mathrm{mono}}(\boldsymbol{r}') = -\frac{\mathrm{i}k\exp(\mathrm{i}kr)}{2\pi r}\,\hat{\boldsymbol{r}}^{(i)} \cdot \hat{\boldsymbol{n}}(\boldsymbol{r}') \tag{12}$$

$$v_{\mathrm{mono}}(\boldsymbol{r}') = 2\hat{\boldsymbol{r}}^{(i)} \cdot \boldsymbol{r}'. \tag{13}$$

Comparing (12) and (13) with (8), the amplitude function now is simplified into a scalar function $s_{\mathrm{mono}}(\boldsymbol{r}')$. Furthermore, from (7) and (10), $\boldsymbol{E}_s(\boldsymbol{r})$ under the PO approximation for both the bistatic and monostatic cases takes the general form

$$\tilde{I} = \int_{\partial\Omega} s(\boldsymbol{r}') \exp\left[\mathrm{i}kv(\boldsymbol{r}')\right] \mathrm{d}S(\boldsymbol{r}'). \tag{14}$$

Here, the amplitude and phase terms are denoted as $s(\boldsymbol{r}')$ and $v(\boldsymbol{r}')$, respectively.

3 The quadratic polynomial approximation of the amplitude and phase functions

We assume that the surface of the object $\partial\Omega$ is governed by equation $z = f(x, y)$, and its projection onto the $x-y$ plane is $\partial\Omega_{xy}$. Then we use M triangular patches to discretize the domain $\partial\Omega_{xy}$, that is, $\triangle_1$, $\triangle_2$, $\cdots$, $\triangle_M$.

To capture the stationary phase and resonance points of the PO integrand in (3), we approximate the amplitude and phase functions by the second order polynomials on these triangular patches. Hence, the PO integral $\tilde{I}$ in (3) can be expressed as

$$\begin{aligned}\tilde{I} &= \int_{\partial\Omega_{xy}} \tilde{s}(x,y)\exp\left[\mathrm{i}k\tilde{v}(x,y)\right]t(x,y)\,\mathrm{d}x\mathrm{d}y \\ &= \sum_{n=1}^{M}\int_{\triangle_n}\tilde{d}(x,y)\exp\left[\mathrm{i}k\tilde{v}(x,y)\right]\mathrm{d}x\mathrm{d}y \simeq \sum_{n=1}^{M}\tilde{I}_n,\end{aligned} \tag{15}$$

Furthermore, after some affine transformations, the quadratic phase function $\tilde{v}_n(x,y)$ in each summation integral term in (15) has the simplified canonical form. In this manner, each summation integral term in (15) can be reformulated as

$$I_n = \int_{\triangle_n'} \tilde{p}_n(x',y')\exp\left\{\mathrm{i}k\left[\pm(x')^2 \pm (y')^2\right]\right\}\mathrm{d}x'\mathrm{d}y' \tag{16}$$

where

$$\tilde{p}_n(x',y') = \tilde{d}_n[x(x',y'),y(x',y')]\exp\left(\mathrm{i}k\tilde{G}_n|\boldsymbol{Q}_n|\right) \tag{17}$$

is also a second order polynomial in the $x'-y'$ coordinate system, and $\boldsymbol{Q}_n = \left[\frac{\partial(x,y)}{\partial(x',y')}\right]_{(\triangle_n\to\triangle_n')}$ is the Jacobi coordinate transform matrix between two coordinate systems $x-y$ and $x'-y'$. The above canonical expression (16) is valid for both monostatic and bistatic cases.

Due to the highly oscillatory behavior of the canonical form PO integral I_n in (16), if one evaluates it accurately by the direct numerical scheme, such as the adaptive Simpson's rule, the number of discretized triangle meshes in (15) shall increase as $M = M(k) \sim O(k^2)$. In the following, we will propose a NSDP method to k-independently evaluate the canonical PO integral I_n in (16).

4 The numerical steepest descent path method for the PO scattered field

We assume D as the trapezoidal domain, as shown in Fig. 1. We denote the $x-$values of vertex points $\boldsymbol{V}_1$ and $\boldsymbol{V}_2$ as L_1 and L_2, respectively. The governing line equation for edge $\boldsymbol{V}_3\boldsymbol{V}_4$ is $y = ax + b$, with $a > 0$. The amplitude phase function $p(x,y)$ has the similar form as $q(x,y)$ except with coefficients α_j instead, $j = 1, 2, \ldots, 6$.

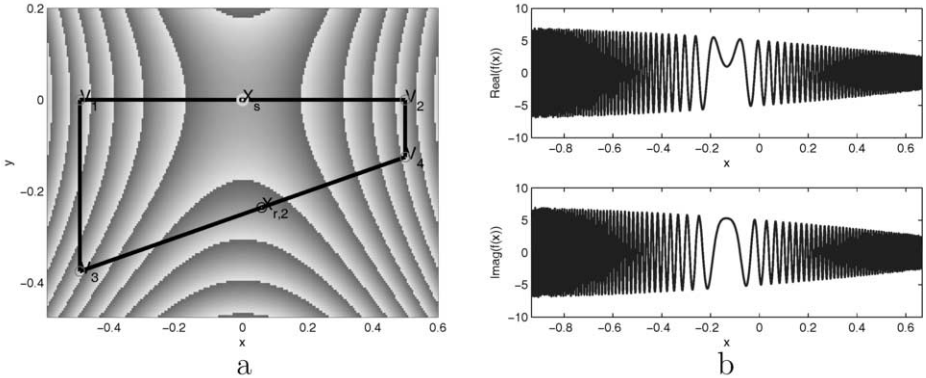

a b

Figure 1: (a) The integration domain is defined on $\boldsymbol{V}_1\boldsymbol{V}_2\boldsymbol{V}_3\boldsymbol{V}_4$, $[L_1, L_2] \times [ax+b, 0]$ for integrand $e^{\mathrm{i}k\left(-x^2+y^2\right)}$ with $a = 0.25$, $b = -0.5$; (b) highly oscillatory PO type integrand, $f(x) = (5 - 3x - x^2)e^{\mathrm{i}k(-x^2+(ax+b)^2)}$, with $k = 500$.

4.1 Reduction of the PO surface integral into highly oscillatory line integrals

$$
\begin{aligned}
I^{(a,b)} &= \int_{L_1}^{L_2}\int_{ax+b}^{0} p(x,y)\,\exp\left[\mathrm{i}k\left(-x^2+y^2\right)\right]\mathrm{d}y\mathrm{d}x \\
&= \int_{L_1}^{L_2}\left[J_2^{(0,0)}(x) - J_2^{(a,b)}(x)\right]\exp\left(-\mathrm{i}kx^2\right)\mathrm{d}x \qquad (18)
\end{aligned}
$$

with $J_2^{(0,0)}(x)$ and $J_2^{(a,b)}(x)$ expressed as

$$J_2^{(0,0)}(x) = j_1(x) + j_2^{(0,0)}(x) \qquad (19)$$

$$J_2^{(a,b)}(x) = j_1(x)\,\mathrm{erfc}\left[\sqrt{-\mathrm{i}k}(ax+b)\right] + j_2^{(a,b)}(x)\,\exp\left(\mathrm{i}k(ax+b)^2\right) \qquad (20)$$

and

$$j_1(x) = -\frac{\sqrt{\pi}}{2\sqrt{-\mathrm{i}k}}\left(\alpha_1 + \alpha_2 x + \alpha_4 x^2 - \frac{\alpha_5}{2\mathrm{i}k}\right) \qquad (21)$$

$$j_2^{(a,b)}(x) = \frac{\alpha_3 + \alpha_6 x + \alpha_5(ax+b)}{2\mathrm{i}k} \qquad (22)$$

$$j_2^{(0,0)}(x) = \frac{\alpha_3 + \alpha_6 x}{2\mathrm{i}k}. \qquad (23)$$

Hence, the original PO integral $I^{(a,b)}$ in (18) can be rewritten as

$$I^{(a,b)} = I_2^{(0,0)} - I_2^{(a,b)} \qquad (24)$$

where

$$I_2^{(a,b)} = \int_{L_1}^{L_2} J_2^{(a,b)}(x)\,\exp\left(-\mathrm{i}kx^2\right)\mathrm{d}x \tag{25}$$

$$I_2^{(0,0)} = \int_{L_1}^{L_2} J_2^{(0,0)}(x)\,\exp\left(-\mathrm{i}kx^2\right)\mathrm{d}x. \tag{26}$$

Here, $I_2^{(a,b)}$ and $I_2^{(0,0)}$ are line integrals associated with edges $\boldsymbol{V}_1\boldsymbol{V}_2$ and $\boldsymbol{V}_3\boldsymbol{V}_4$, respectively.

4.2 Phase behavior of $I_2^{(a,b)}$ and its stationary phase point

As a result, the integrand $J_2^{(a,b)}(x)$ in (20) has the following asymptotic behavior

$$\begin{aligned} J_2^{(a,b)}(x) &= \begin{cases} j_1(x)\nu_1(x)\,\exp\left[\mathrm{i}k(ax+b)^2\right] & \\ \qquad +j_2^{(a,b)}(x)\,\exp\left[\mathrm{i}k(ax+b)^2\right], & x \in \mathcal{D}_1, \\ 2j_1(x) + j_1(x)\nu_2(x)\,\exp\left[\mathrm{i}k(ax+b)^2\right] & \\ \qquad +j_2^{(a,b)}(x)\,\exp\left[\mathrm{i}k(ax+b)^2\right], & x \in \mathcal{D}_2 \end{cases} \\ &= \begin{cases} \varsigma_1(x)\,\exp\left[\mathrm{i}k(ax+b)^2\right], & x \in \mathcal{D}_1, \\ 2j_1(x) + \varsigma_2(x)\,\exp\left[\mathrm{i}k(ax+b)^2\right], & x \in \mathcal{D}_2 \end{cases} \end{aligned} \tag{27}$$

with $\varsigma_1(x)$, $\varsigma_2(x)$ denoted as slowly varying functions. $\mathcal{D}_1$ and $\mathcal{D}_2$ are the domains separated by the *Stokes' line* on the complex plane, with the expressions

$$l_{\text{Stokes}}(x) : \mathrm{Im}(x) = -\mathrm{Re}(x) - \frac{b}{a} \tag{28}$$

$$\mathcal{D}_1 := a\left[\mathrm{Re}(x) + \mathrm{Im}(x)\right] + b > 0 \tag{29}$$

$$\mathcal{D}_2 := a\left[\mathrm{Re}(x) + \mathrm{Im}(x)\right] + b < 0. \tag{30}$$

For the case $x \in \mathcal{D}_2$ in (27), the first term $2j_1(x)$ comes from the Stokes' phenomenon of the complementary error function.

After substituting (27) into (25), we get two phase function terms for $I_2^{(a,b)}$. They are

$$g_1(x) = -x^2 + (ax+b)^2 \tag{31}$$

$$g_2(x) = -x^2. \tag{32}$$

The above equations indicate that the Stokes' phenomenon of complementary error function makes the phase behaviors of the PO integrand $I_2^{(a,b)}$ be discontinuous.

4.3 Numerical steepest descent paths for $I_2^{(a,b)}$

Firstly, we consider the first phase function $g_1(x)$ of $I_2^{(a,b)}$ in (31) and (32). Physically, there may exist a point x_s, at which the phase behavior of $g_1(x)$ is different from others. It is called the *stationary phase point* (SPP). SPP corresponds to the point at which the specular reflection occurs in the high frequency ray physics regime. Mathematically, the SPP x_s satisfies the condition $g_1'(x_s) = 0$. As a result, we have the mathematical expression of x_s as

$$x_s = \begin{cases} \frac{ab}{1-a^2}, & |a| \neq 1 \\ \text{no stationary phase point}, & |a| = 1 \end{cases} \tag{33}$$

Now we see the term $\exp\left[\mathrm{i}kg_1(x)\right]$ in the PO integrand

$$\begin{aligned} \exp\left[\mathrm{i}kg_1(x)\right] &= \exp\left(\mathrm{i}k\ \{\mathrm{Re}[g_1(x)] + \mathrm{i}\,\mathrm{Im}[g_1(x)]\}\right) \\ &= \exp\left\{-k\,\mathrm{Im}[g_1(x)] + \mathrm{i}k\,\mathrm{Re}[g_1(x)]\right\}. \end{aligned} \tag{34}$$

The NSDP method relies on the transformation of the above highly oscillatory functions to exponential decay functions on the complex plane.

To achieve this, for a starting point L_*, we define a complex path function $x = \varphi_{L_*}(p)$ as that in [3], satisfying the following identity

$$-\varphi_{L_*}(p)^2 + \left[a\varphi_{L_*}(p) + b\right]^2 = -L_*^2 + (aL_* + b)^2 + ip^l, \tag{35}$$

with $l = 1$ for integration end points L_1 and L_2, and $l = 2$ for the SPP x_s. After substituting L_1, L_2 and x_s into (35), the corresponding NSDPs are

$$\varphi_{L_m}(p) = \begin{cases} \frac{\mathrm{sgn}(L_m')}{\sqrt{a^2-1}}\sqrt{L_m'^{\,2} + \mathrm{i}p} + x_s, & |a| > 1, \quad p \in [0, \infty) \\ \frac{\mathrm{sgn}(L_m')}{\sqrt{1-a^2}}\sqrt{L_m'^{\,2} - \mathrm{i}p} + x_s, & |a| < 1, \quad p \in [0, \infty) \\ L_m + \frac{\mathrm{i}p}{2ab}, & |a| = 1, \quad p \in [0, \infty) \end{cases} \tag{36}$$

$$\varphi_{x_s}(p) = \begin{cases} \frac{p\sqrt{\mathrm{i}}}{\sqrt{|1-a^2|}} + x_s, & |a| > 1, \quad p \in (-\infty, \infty) \\ \frac{p\sqrt{-\mathrm{i}}}{\sqrt{|1-a^2|}} + x_s, & |a| > 1, \quad p \in (-\infty, \infty) \\ \text{no NSDP}, & |a| = 1, \quad p \in (-\infty, \infty) \end{cases} \tag{37}$$

Here,

$$L_m' = \sqrt{|1-a^2|}\left(L_m - \frac{ab}{1-a^2}\right) = \sqrt{|1-a^2|}(L_m - x_s), \quad m = 1, 2. \tag{38}$$

In Fig. 2, we demonstrate the diagrams of the NSDPs expressed in (36) and (37), with cases $a > 1$ and $a = 1$. Possible cases of NSDP occur when a

changes to the negative sign. However, for the brevity of this paper, we skip those cases here.

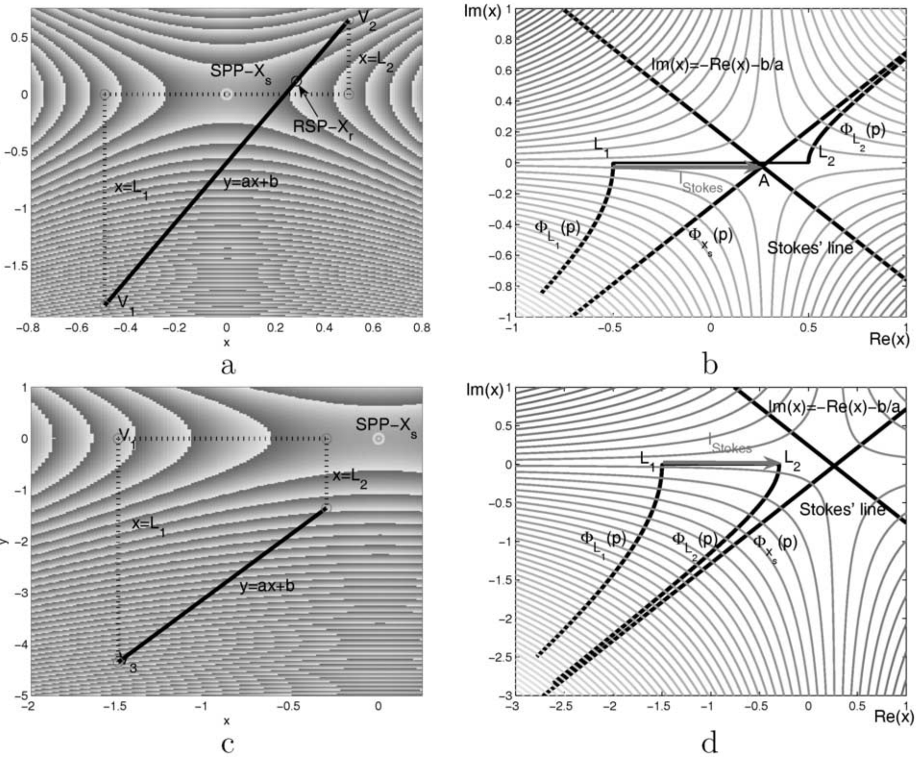

a b

c d

Figure 2: Sub-figures (a) and (b): $I_2^{(a,b)}$ defined on the integration domain $[L_1, L_2]$ with $L_1 < x_s < L_2$, and its numerical steepest descent paths $\varphi_{L_1}(p) \bigcup \varphi_{x_s}(p) \bigcup \varphi_{L_2}(p)$; sub-figures (c) and (d): $I_2^{(a,b)}$ defined on the integration domain $[L_1, L_2]$ with $x_s > L_2$, and its numerical steepest descent paths $\varphi_{L_1}(p) \bigcup \varphi_{L_2}(p)$.

With the above expressions for NSDPs, we give the following main theorem in this paper.

Theorem 4.1 (Frequency independent theorem by the NSDP method). *The highly oscillatory integrand of* $I_2^{(a,b)}$ *in* (25), (26), *i.e.,* $J_2^{(a,b)}(x) \exp\left(-\mathrm{i}kx^2\right)$ *defined on the real integration domain* $[L_1, L_2]$ *can be transformed to that defined on several complex NSDPs on the complex plane, denoted as* $\varphi_{\mathrm{NSDPs}}(p)$, *that takes the formulation*

$$\varphi_{\mathrm{NSDPs}}(p) = \begin{cases} \varphi_{L_1}(p) \bigcup \varphi_{x_s}(p) \bigcup \varphi_{L_2}(p), & L_1 < x_s < L_2 \\ \varphi_{L_1}(p) \bigcup \varphi_{L_2}(p), & L_2 < x_s \end{cases} \tag{39}$$

with these two cases shown in Fig. 2. Then, $I_2^{(a,b)}$ *takes the formulation*

$$I_2^{(a,b)} = \begin{cases} I_{2,L_1}^{(a,b)} + I_{2,x_s}^{(a,b)} - I_{2,L_2}^{(a,b)} + K_2(\boldsymbol{A}) - K_2(L_1,0), & L_1 < x_s < L_2 \\ I_{2,L_1}^{(a,b)} - I_{2,L_2}^{(a,b)} + K_2(L_2,0) - K_2(L_1,0), & L_2 < x_s \end{cases}. \quad (40)$$

Here, $I_{2,L_1}^{(a,b)}$, $I_{2,L_2}^{(a,b)}$ *and* $I_{2,x_s}^{(a,b)}$ *are integrals with exponential decay integrands defined on* $\varphi_{L_1}(p)$, $\varphi_{L_2}(p)$ *and* $\varphi_{x_s}(p)$, *respectively. The complex point* $\boldsymbol{A}$ *corresponds to the intersection point in Fig. 2, and* $K_2(x)$ *is the primitive function of kernel* $2j_1(x)\exp\left(-\mathrm{i}kx^2\right)$ *in* (21), *with the formula*

$$\begin{aligned} K_2(x) = {} & \left(\frac{\pi}{2k}\alpha_1 + \frac{\pi}{4\mathrm{i}k^2}\alpha_4 - \frac{\pi}{4\mathrm{i}k^2}\alpha_5\right)\operatorname{erfc}\left(\sqrt{\mathrm{i}k}\,x\right) \\ & + \left(\frac{\sqrt{\pi}}{2\mathrm{i}k\sqrt{-ik}}\alpha_2 + \frac{\sqrt{\pi}x}{2\mathrm{i}k\sqrt{-ik}}\alpha_4\right)\exp\left(-\mathrm{i}kx^2\right). \end{aligned} \quad (41)$$

Furthermore, on invoking the Gauss-Laguerre quadrature rule, the PO integrand $J_2^{(a,b)}(x)\exp\left(-\mathrm{i}kx^2\right)$ *defined on* $\varphi_{\mathrm{NSDPs}}(p)$ *can be integrated with workload independent of frequency* k, *as* $k \gg 1$.

The detailed proof is given in [17].

5 Numerical results

To illustrate the efficiency of the proposed NSDP method, first, we conduct some numerical experiments for the PO line integral $I_2^{(a,b)}$. Next, we

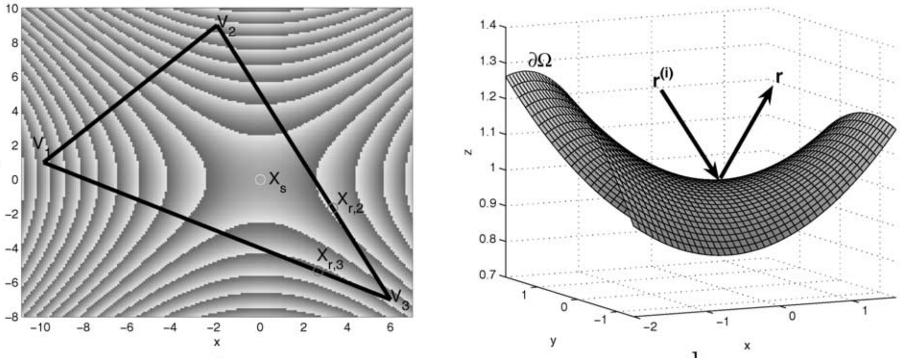

a b

Figure 3: (a) PO surface integral $I_{\triangle_1}$, defined on the triangular patch–Δ_1; (b) the electromagnetic wave impinges on the quadratic saddle surface $\partial\Omega$, governed by equation $z = f(x, y)$.

extend the PO surface integral on the triangular patch. Finally, the RCS values of the PO scattered electric field on the saddle surface are generated via the proposed NSDP method.

5.1 PO surface integral on the triangular patch

In this subsection, we consider the triangular patch $\triangle_1$, as shown in Fig. 3. The critical points in $\triangle_1$ contain the SPP $\boldsymbol{X}_s$, two RSPs $\boldsymbol{X}_{r,m}$ and three vertex points $\boldsymbol{V}_n$, $m = 2, 3$, $n = 1, 2, 3$.

In contrast to the HFA method, Fig. 4 depicts that the PO results by the NSDP method can be significantly improved by one to two orders when $k \in [10, 100]$, as expressed by $E^{(\mathrm{NSDP})}_{\Delta_1}(k)$ and $E^{(\mathrm{HFA})}_{\Delta_1}(k)$. Meanwhile, the computational effort for the PO integral by the NSDP method is also $O(1)$.

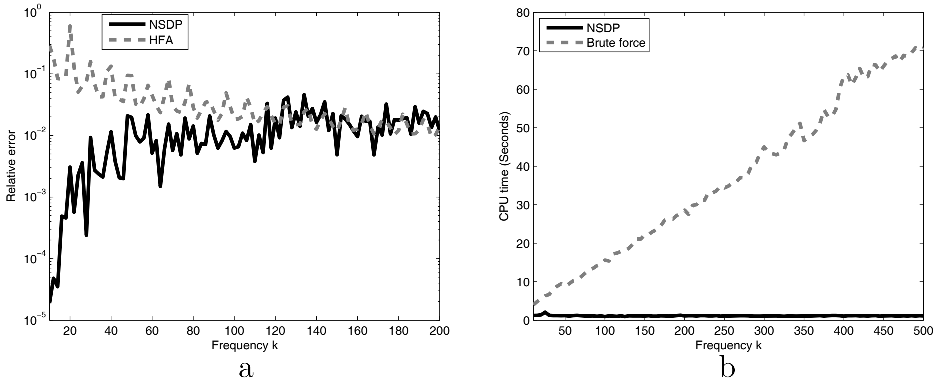

a b

Figure 4: (a) The relative errors of the PO results by using the NSDP and HFA methods relative to the BF method on Δ_1, denoted by $E^{(\mathrm{NSDP})}_{\Delta_1}(k)$ and $E^{(\mathrm{HFA})}_{\Delta_1}(k)$; (b) CPU time comparisons by using NSDP and BF methods.

5.2 PO scattered field on the saddle surface

Finally, we apply the NSDP method to analyze the PO scattered field on the saddle surface in Fig. 3. The incident wave propagates along $\hat{\boldsymbol{r}}^{(i)} = \left[0.5, 0.5, -\sqrt{2}/2\right]$ direction, and the observation point is set along the direction $\hat{\boldsymbol{r}} = \left[\sqrt{2}/4, \sqrt{6}/4, \sqrt{2}/2\right]$.

Figure 5 gives comparisons of the errors of $\boldsymbol{E}_s(\boldsymbol{r})$ produced by NSDP and HFA methods relative to the BF method. Compared with the HFA method, the advantage on improving the scattered electric field accuracy by the NSDP method is again confirmed in Fig. 5.

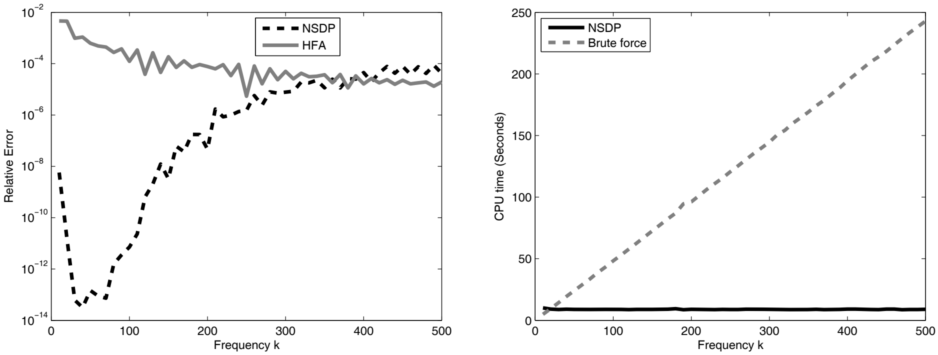

a b

Figure 5: (a) The relative errors of the bistatic scattered electric field $\boldsymbol{E}_s(\boldsymbol{r})$ results by using NSDP and HFA methods relative to the BF method on the saddle surface; (b) comparisons of the CPU time (second unit) for the PO scattered electric field by using NSDP and BF methods.

On invoking the NSDP method, the various critical-point contributions to $\boldsymbol{E}_s(\boldsymbol{r})$ are compared in Fig. 6. Also, we see that the SPP point contribution dominates $\boldsymbol{E}_s(\boldsymbol{r})$ when k is large. Again, Fig. 5 demonstrates the frequency independent computational effort for the scattered electric field. Finally, we apply the NSDP method to calculate the bistatic RCS values of $\boldsymbol{E}_s(\boldsymbol{r})$, which are in good agreement with the results generated by the BF method.

In summary, the proposed NSDP method for calculating the PO scattered field on the quadratic saddle surface is frequency independent and error controllable.

6 Conclusion

In this paper, we propose the NSDP method to calculate the scattered field on the quadratic saddle surface in the high frequency regime. The scattered electric field can be reduced to several highly oscillatory PO surface integrals. By applying the NSDP method, high frequency critical-point contributions are rigorously expressed on these NSDPs. Finally, extensive numerical experiments are given to show the efficiency of the NSDP method. In conclusion, the NSDP method for calculating the electric scattered field on the quadratic saddle surface is frequency independent and error controllable.

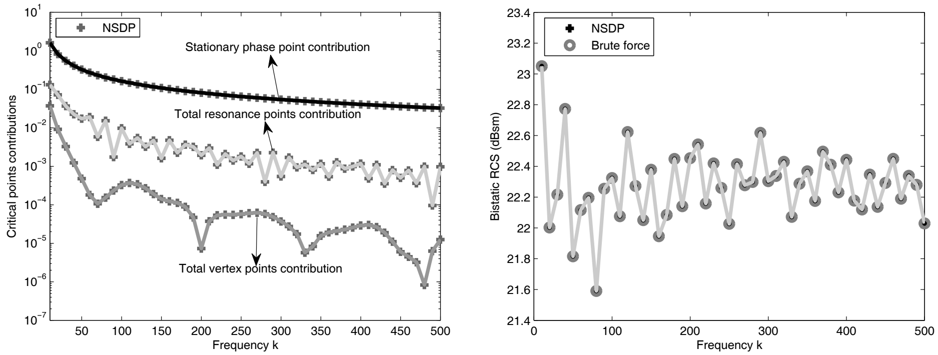

a b

Figure 6: (a) Critical points contributions to $\boldsymbol{E}_s(\boldsymbol{r})$ in (7) in terms of the NSDP method; (b) comparisons of the RCS (dBsm unit) values of the PO scattered electric field on the saddle surface by using NSDP and BF methods.

Acknowledgment

This work was supported in part by the Research Grants Council of Hong Kong (GRF 711511, 713011, and 712612), HKU Small Project Funding(201007176196), HKU Seed funding (201102160033), HKU UDF-CSE grant, and in part by the University Grants Council of Hong Kong (Contract No. AoE/P-04/08).

Bibliography

[1] H. M. Macdonald, “The effect produced by an obstacle on a train of electric waves,” *Phil. Trans. Royal Soc. London, Series A, Math. Phys. Sci.*, no. 212, pp. 299–337, 1913.

[2] P. Y. Ufimtsev, “New insight into the classical macdonald physical optics approximation,” *IEEE Antennas Propag. Mag.*, vol. 50, no. 3, pp. 11–20, June 2008.

[3] W. C. Chew, *Waves and Fields in Inhomogeneous Media*, New York: IEEE Press, 1995.

[4] J. A. Kong, *Electromagnetic Wave Theory*, Cambridge, MA: EMW Publishing, 2000.

[5] W. C. Chew, M. S. Tong, and B. Hu, *Integral Equations Methods for Electromagnetic and Elastic Waves*, Morgan and Claypool, 2008.

[6] R. Harrington, *Field Computation by Moment Method*, New York: Macmillan, 1968.

[7] J. M. Song, C. C. Lu, and W. C. Chew, “Multilevel fast multipole algorithm for electromagnetic scattering by large complex objects,” *IEEE Trans. Antennas Propag.*, vol. 45, no. 10, pp. 1488–1493, Oct. 2009.

[8] A. C. Ludwig, “Computation of radiation patterns involving numerical double integration,” *IEEE Trans. Antennas Propag.*, vol. 16, no. 6, pp. 767–769, Nov. 1968.

[9] S. W. Lee and G. A. Deschamps, “A uniform asymptotic theory of electromagnetic diffraction by a curved wedge,” *IEEE Trans. Antennas Propag.*, vol. 24, no. 1, pp. 25–34, Jan. 1976.

[10] G. Carluccio, M. Albani, and P. H. Pathak, “Uniform asymptotic evaluation of surface integrals with polygonal integration domains in terms of UTD transition functions,” *IEEE Trans. Antennas Propag.*, vol. 58, no. 4, pp. 1155–1163, April, 2010.

[11] R. Wong, *Asymptotic Approximations of Integrals*, New York: SIAM, 2001.

[12] M. Abramowitz and I. A. Stegun, *Handbook of Mathematical Functions*, Mineola, NY: Dover Publications Inc., 1972.

[13] Y. M. Wu, L. J. Jiang, and W. C. Chew, “An efficient method for computing highly oscillatory physical optics integral,” *Progress In Electromagnetics Research (PIER)* vol. 127, pp. 211–257, April, 2012.

[14] Y. M. Wu, L. J. Jiang, and W. C. Chew, “An efficient method for computing highly oscillatory physical optics integral,” in *Proc. IEEE International Symposium on Antennas and Propagation and USNC-URSI National Radio Science Meeting* pp. 1–2, Chicago, USA, July, 2012.

[15] Y. M. Wu, L. J. Jiang, W. E. I. Sha, and W. C. Chew, “The numerical steepest descent path method for calculating physical optics integrals on smooth conducting surfaces,” *IEEE Trans. Antennas Propag.*, in revision.

[16] Y. M. Wu, L. J. Jiang, and W. C. Chew, “Computing highly oscillatory physical optics integral on the polygonal domain by an efficient numerical steepest descent path method,” *J. Comput. Phys.*, November 24, 2012, [Online]. Available: dx.doi.org/10.1016/j.jcp.2012.10.052.

[17] Y. M. Wu, W. C. Chew, and L. J. Jiang, “A frequency independent method for computing high frequency physics optics scattered electromagnetic fields on saddle surfaces,” *SIAM Journal on Scientific Computing*, submitted.

Progress in multiscale computational electromagnetics in time domain

Luis Tobón[†,‡], **Jiefu Chen**[§], **Junho Lee**[*], **Mengqing Yuan**[*], **Bo Zhao**[*] and **Qing Huo Liu**[†]

[†] *Department of Electrical and Computer Engineering, Duke University, Durham, NC 27708, USA, e-mail: luis.tobonllano@duke.edu*

[‡] *Department of Electronic Engineering and Computer Science, Pontificia Universidad Javeriana-Cali, Santiago de Cali 56710, Colombia*

[§] *Adv. R&D Center, Weatherford International Ltd., Houston, TX 77060, USA*

[*] *Wave Computational Technology, Inc. (WCT), Durham, NC 27707, USA*

Abstract

Many system-level electromagnetic design problems are multiscale and very challenging to solve. They remain a significant barrier to system design optimization for a foreseeable future. Such multiscale problems often contain three electrical scales, i.e., the fine scale (geometrical feature size much smaller than a wavelength), the coarse scale (geometrical feature size greater than a wavelength), and the intermediate scale between the two extremes. Existing computational tools are based on single methodologies (such as finite element method or finite-difference time-domain method), and are unable to solve large multiscale problems. We will present our recent progress in solving realistic multiscale system-level EM design simulation problems in time domain. The discontinuous Galerkin time domain method is used as the fundamental framework for interfacing multiple scales with finite-element method, spectral element method, and finite difference method. Numerical results demonstrate significant advantages of our multiscale method. A more detail discussion of the method is given in [1].

Pulsed Electromagnetic Fields: Their Potentialities, Computation and Evaluation
I. E. Lager and L. J. Jiang (Eds.).
doi: 10.3233/978-1-61499-230-1-55

1 Introduction

Realistic system level electromagnetic problems such as electromagnetic interference (EMI), electromagnetic compatibility (EMC) ans signal integrity (SI) are often multiscale. Examples of multiscale problems include small devices under test in a reverberation chamber for EMC/EMI testing, and a multilayer package-to-chip structure in Fig. 1. Here electrically fine structures with details much smaller than a typical wavelength (mode stirrers, devices under testing in the chamber, or on-chip interconnects in the package-to-chip structure) coexist with electrically coarse structures comparable to or larger than a typical wavelength (the empty space insider the chamber, or the package in the multilayer circuit).

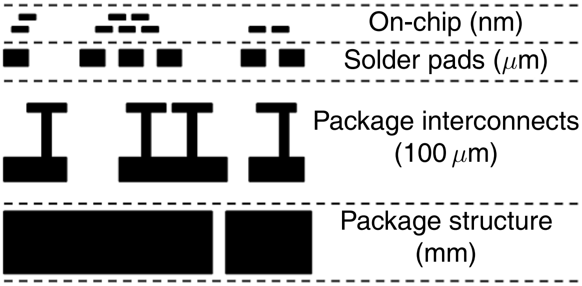

Figure 1: Multiscale package-to-chip structure.

Simulating transient multiscale problems can be very challenging for the conventional finite-difference time-domain (FDTD) method and the finite-element time-domain (FETD) method. The FDTD method [2, 3] requires an orthogonal grid. Thus, a high discretization density required to capture the geometric characteristics of electrically fine structures will lead to a large number of wasted unknowns in the electrically coarse domains. The subgridding technique [4] can alleviate this issue of the FDTD method; however, it will spoil the simple data structure of the standard FDTD scheme and greatly increase computational complexity. The FETD method [5,6] is more flexible in geometric modeling. However, this method requires solving matrix equations, either directly or iteratively. A discretized multiscale problem usually has a large number of unknowns, viz. huge system matrices. It can be prohibitively expensive to perform operations with huge matrices during time stepping.

Discontinuous Galerkin time-domain (DGTD) methods [7–17] are promising in solving multiscale problems. First, for geometric modeling, DGTD allows for domain decomposition. A multiscale structure can be divided into several subdomains, and each subdomain can be discretized by a specific mesh density based on its geometric characteristics. Based on the idea of domain decomposition, DGTD is much more flexible than FDTD and FETD in modeling complex structures because large system matrices are split into a bunch of smaller matrices. DGTD can easily handle problems too large to be solved by the conventional FETD method. As for time integration, DGTD allows for different time stepping schemes to be used in different subdomains. For example, efficient explicit schemes can be applied to subdomains with coarser meshes and relatively large CFL numbers, while unconditionally stable implicit schemes can be employed in subdomains with dense meshes to overcome CFL restrictions. These flexibilities in both spatial and temporal discretization make DGTD efficient in multiscale simulations.

Constructing a DGTD system consists of several key steps: (a) deciding on which governing equations the DGTD method will be based on; (b) choosing element shape and corresponding basis functions for the spatial discretization of each subdomain; (c) applying numerical fluxes onto interfaces to stitch all subdomains together; and (d) selecting a time stepping scheme based on properties of a discretized system. Each step of the above procedure has more than one choice. Thus, dozens of DGTD variations have been proposed with different combinations of implementation schemes. In this review we provide a discussion of the fundamental issues of each step, emphasizing the details of one specific scheme based on mixed finite element discretization and the hybrid implicit-explicit (IMEX) time stepping scheme.

2 The discontinuous Galerkin system for transient electromagnetic analysis

2.1 Governing equations for time domain electromagnetic analysis

The transient electromagnetic problems can be governed by different equations such as first order Maxwell's equations or a second order wave equation. Mathematically these governing equations are equivalent, however, with different discretization schemes they differ greatly in numerical properties [18].

The second order wave equation uses directly curl-conforming elements [19–22], which are free of spurious modes and facilitate the imposition of boundary condition. Despite such advantages, the wave equations have difficulties in constructing the time-domain perfectly matched layer (PML), which is believed to be an all-purpose technique to truncate unbounded regions. Moreover, the implementation of numerical fluxes [23–25], a critical step in building a DGTD system, is based on both $\boldsymbol{E}$ and $\boldsymbol{H}$ variables. These limitations make the wave equation with only one discretized field less suitable for DGTD methods.

To avoid the above difficulties the DGTD systems can be based on first order Maxwell's equations with both $\boldsymbol{E}$ and $\boldsymbol{H}$ as field variables

$$\epsilon\frac{\partial \boldsymbol{E}}{\partial t} + \sigma\boldsymbol{E} - \boldsymbol{\nabla}\times\boldsymbol{H} = -\boldsymbol{J}_{\mathrm{s}} \tag{1}$$

$$\mu\frac{\partial \boldsymbol{H}}{\partial t} + \boldsymbol{\nabla}\times\boldsymbol{E} = \boldsymbol{0} \tag{2}$$

In the following subsections we will see that it is straightforward to implement numerical fluxes for this first order system.

2.2 Galerkin's weak form and numerical fluxes

Denote $\boldsymbol{\Phi}$ and $\boldsymbol{\Psi}$ as basis functions for $\boldsymbol{E}$ and $\boldsymbol{H}$, respectively. With integration by parts, the Galerkin's weak forms of Maxwell's equations are

$$\begin{aligned}&\int_V \boldsymbol{\Phi}\cdot\left(\epsilon\frac{\partial \boldsymbol{E}}{\partial t} + \sigma\boldsymbol{E} + \boldsymbol{J}_{\mathrm{s}}\right)\mathrm{d}V - \int_V (\boldsymbol{\nabla}\times\boldsymbol{\Phi})\cdot\boldsymbol{H}\,\mathrm{d}V\\ &= \int_S \boldsymbol{\Phi}\cdot(\boldsymbol{n}\times\boldsymbol{H})\,\mathrm{d}S\end{aligned} \tag{3}$$

$$\begin{aligned}&\int_V \boldsymbol{\Psi}\cdot\mu\frac{\partial \boldsymbol{H}}{\partial t}\mathrm{d}V + \int_V (\boldsymbol{\nabla}\times\boldsymbol{\Psi})\cdot\boldsymbol{E}\,\mathrm{d}V\\ &= -\int_S \boldsymbol{\Psi}\cdot(\boldsymbol{n}\times\boldsymbol{E})\,\mathrm{d}S\end{aligned} \tag{4}$$

where V denotes the volume of a subdomain, which contains one or more elements, $\boldsymbol{n}$ is the unit normal vector located on surface S and pointing to the outside of V. The terms on the right hand sides of equations (3) and (4) are integrals over subdomain interfaces. In DGTD methods they are evaluated by numerical fluxes.

Choosing different numerical fluxes can lead to different DGTD systems. One commonly used numerical flux is the Riemann solver [23, 24], which is a type of upwind numerical flux and is derived from the physical process of wave propagation and reflection across an interface between two different media

$$\begin{aligned}\int_S \boldsymbol{\Phi}\cdot(\boldsymbol{n}\times\boldsymbol{H})\,\mathrm{d}S &= \int_S \boldsymbol{\Phi}\cdot\left[\boldsymbol{n}\times\frac{Z^{(i)}\boldsymbol{H}^{(i)} + Z^{(j)}\boldsymbol{H}^{(j)}}{Z^{(i)}+Z^{(j)}}\right]\mathrm{d}S\\ &\quad + \int_S \boldsymbol{\Phi}\cdot\left[\boldsymbol{n}\times\boldsymbol{n}\times\frac{\boldsymbol{E}^{(i)} - \boldsymbol{E}^{(j)}}{Z^{(i)}+Z^{(j)}}\right]\mathrm{d}S\end{aligned} \tag{5}$$

$$\begin{aligned}\int_S \boldsymbol{\Psi}\cdot(\boldsymbol{n}\times\boldsymbol{E})\,\mathrm{d}S &= \int_S \boldsymbol{\Psi}\cdot\left[\boldsymbol{n}\times\frac{Y^{(i)}\boldsymbol{E}^{(i)}+Y^{(j)}\boldsymbol{E}^{(j)}}{Y^{(i)}+Y^{(j)}}\right]\mathrm{d}S\\ &\quad -\int_S \boldsymbol{\Psi}\cdot\left[\boldsymbol{n}\times\boldsymbol{n}\times\frac{\boldsymbol{H}^{(i)}-\boldsymbol{H}^{(j)}}{Y^{(i)}+Y^{(j)}}\right]\mathrm{d}S \qquad (6)\end{aligned}$$

where $Z^{(i)} = 1/Y^{(i)} = \sqrt{\mu^{(i)}/\epsilon^{(i)}}$ and $Z^{(j)} = 1/Y^{(j)} = \sqrt{\mu^{(j)}/\epsilon^{(j)}}$ are wave impedances for the i-th and the j-th subdomains, respectively.

2.3 Discretized system of linear equations

Assuming a multiscale structure is divided into N subdomains, the discretized system of equations by the DGTD method will be

$$\boldsymbol{M}_{ee}^{(i)}\frac{\mathrm{d}\boldsymbol{e}^{(i)}}{\mathrm{d}t} = \boldsymbol{K}_{eh}^{(i)}\boldsymbol{h}^{(i)} + \boldsymbol{C}_{ee}^{(i)}\boldsymbol{e}^{(i)} + \boldsymbol{j}^{(i)} + \sum_{j=1}^{N}\left(\boldsymbol{L}_{ee}^{(ij)}\boldsymbol{e}^{(j)} + \boldsymbol{L}_{eh}^{(ij)}\boldsymbol{h}^{(j)}\right), \quad i = 1,\ldots,N \qquad (7)$$

$$\boldsymbol{M}_{hh}^{(i)}\frac{d\boldsymbol{h}^{(i)}}{dt} = \boldsymbol{K}_{he}^{(i)}\boldsymbol{e}^{(i)} + \sum_{j=1}^{N}\left(\boldsymbol{L}_{he}^{(ij)}\boldsymbol{e}^{(j)} + \boldsymbol{L}_{hh}^{(ij)}\boldsymbol{h}^{(j)}\right), \quad i = 1,\ldots,N \qquad (8)$$

where $\boldsymbol{e}^{(i)}$ and $\boldsymbol{h}^{(i)}$ are vectors of the discretized electric and magnetic fields, $\boldsymbol{M}_{ee}^{(i)}$ and $\boldsymbol{M}_{hh}^{(i)}$ are the mass matrices, $\boldsymbol{C}_{ee}^{(i)}$ is the damping matrix, $\boldsymbol{K}_{eh}^{(i)}$ and $\boldsymbol{K}_{he}^{(i)}$ are the stiffness matrices, and $\boldsymbol{j}^{(i)}$ is vector of the discretized excitations of the i-th subdomain. Matrices $\boldsymbol{L}_{ee}^{(ij)}$, $\boldsymbol{L}_{eh}^{(ij)}$, $\boldsymbol{L}_{he}^{(ij)}$, $\boldsymbol{L}_{hh}^{(ij)}$ are obtained from the interface integrations and can be viewed as the couplings between fields of the i-th and j-th subdomains. Detailed formulations of these vectors and matrices are referred to [26].

3 Spatial discretization with different basis functions

3.1 DG-FETD: discontinuous Galerkin finite-element time-domain method

The discontinuous Galerkin finite-element time-domain (DG-FETD) method is a very popular DGTD scheme with finite elements employed for spatial discretization of subdomains. The DG-FETD method can be viewed as a combination of discontinuous Galerkin method (DGM) and finite element method (FEM) in time domain. All kinds of finite elements, e.g., nodal or edge elements as basis functions, tetrahedral, prism, or hexahedral elements as element shapes, have been used in constructing different DG-FETD schemes [7–15].

3.2 DG-SETD: discontinuous Galerkin spectral-element time-domain method

Despite its meshing flexibility, the lower order DG-FETD scheme suffers from a slow convergence rate and a large numerical dispersion. To make multiscale simulations more efficient, the electrically coarse part can be selected out and discretized by higher order finite elements with a coarser mesh. The spectral elements are special types of higher order finite elements with interpolation points chosen based on spectral polynomials, such as Gauss-Lobatto-Legendre (GLL) polynomials [27, 28]. By doing so the spectral elements will avoid the Runge phenomenon and lead to diagonal or block diagonal mass matrices, which are especially favorable to time domain computations because inversion of such mass matrices becomes trivial.

4 Time stepping schemes

For a DGTD system, time stepping can be performed subdomain by subdomain rather than solving a huge matrix system as in FETD schemes. This advantage of DGTD methods can save a large amount of memory during time stepping, and furthermore, it makes parallel computation straightforward for a DGTD system.

Local time stepping and hybrid implicit-explicit schemes for multiscale simulations

A discretized multiscale DGTD system usually contains electrically coarse subdomains with coarse meshes, which have relatively large CFL numbers when an explicit time integration scheme is used. Meanwhile the multiscale system also contains electrically fine subdomains with dense meshes, whose CFL numbers may be several orders smaller than those of electrically coarse subdomains. Local time stepping methods such as the multirate Adams-Bashforth scheme [29,30] or hybrid implicit-explicit schemes [31] can be a good fit for a DGTD system under this circumstance.

Take the hybrid implicit-explicit Runge-Kutta (IMEX-RK) [32] scheme as an example, which consists of two parts. The first part is the explicit Runge-Kutta (ERK) method

$$\begin{array}{c|ccccc}
0 & 0 & 0 & \dots & \dots & 0 \\
c_2 & a^{\mathrm{ex}}_{2,1} & 0 & \ddots & \ddots & \vdots \\
c_3 & a^{\mathrm{ex}}_{3,1} & a^{\mathrm{ex}}_{3,2} & 0 & \ddots & \vdots \\
\vdots & \vdots & \vdots & \vdots & \ddots & 0 \\
c_s & a^{\mathrm{ex}}_{s,1} & a^{\mathrm{ex}}_{s,2} & \dots & a^{\mathrm{ex}}_{s,s-1} & 0 \\
\hline
 & b_1 & b_2 & b_3 & \dots & b_s
\end{array} \tag{9}$$

The second part is for the explicit singly diagonally implicit Runge-Kutta (ESDIRK) method

$$\begin{array}{c|ccccc}
0 & a^{\mathrm{im}}_{1,1} & 0 & \dots & \dots & 0 \\
c_2 & a^{\mathrm{im}}_{2,1} & a^{\mathrm{im}}_{2,2} & 0 & \ddots & \vdots \\
c_3 & a^{\mathrm{im}}_{3,1} & a^{\mathrm{im}}_{3,2} & a^{\mathrm{im}}_{3,3} & \ddots & \vdots \\
\vdots & \vdots & \vdots & \vdots & \ddots & 0 \\
c_s & a^{\mathrm{im}}_{s,1} & a^{\mathrm{im}}_{s,2} & \dots & a^{\mathrm{im}}_{s,s-1} & a^{\mathrm{im}}_{s,s} \\
\hline
 & b_1 & b_2 & b_3 & \dots & b_s
\end{array} \tag{10}$$

Assuming a discretized multiscale problem contains N_{ex} explicit subdomains and N_{im} implicit subdomains, the time stepping formulation for the i-th subdomain based on IMEX-RK with s stages is

$$\boldsymbol{v}^{(i)}_{n+1} = \boldsymbol{v}^{(i)}_{n} + \Delta t \sum_{k=1}^{s} b_k \boldsymbol{u}^{(i)}_{k}, \quad i = 1, \cdots, N_{\mathrm{im}} + N_{\mathrm{ex}} \tag{11}$$

where

$$\begin{aligned}
\boldsymbol{M}^{(i)} \boldsymbol{u}^{(i)}_{k} = & \sum_{j=N_{\mathrm{im}}+1}^{N_{\mathrm{im}}+N_{\mathrm{ex}}} \boldsymbol{L}^{(ij)} \left(\boldsymbol{v}^{(j)}_{n} + \Delta t \sum_{l=1}^{k-1} a^{\mathrm{ex}}_{k,l} \boldsymbol{u}^{(j)}_{l} \right) \\
& + \sum_{j=1}^{N_{\mathrm{im}}} \boldsymbol{L}^{(ij)} \left(\boldsymbol{v}^{(j)}_{n} + \Delta t \sum_{l=1}^{k} a^{\mathrm{im}}_{k,l} \boldsymbol{u}^{(j)}_{l} \right) + \boldsymbol{f}^{(i)}(t_n + c_k \Delta t)
\end{aligned} \tag{12}$$

for explicit subdomains, and

$$\begin{aligned}
\left(\boldsymbol{M}^{(i)} - \Delta t a^{\mathrm{im}}_{k,k} \boldsymbol{L}^{(ii)} \right) \boldsymbol{u}^{(i)}_{k} = & \boldsymbol{f}^{(i)} \left(t_n + c_k \Delta t \right) + \boldsymbol{L}^{(ii)} \left(\boldsymbol{v}^{(i)}_{n} + \Delta t \sum_{l=1}^{k-1} a^{\mathrm{im}}_{k,l} \boldsymbol{u}^{(j)}_{l} \right) \\
& + \sum_{j=N_{\mathrm{im}}+1}^{N_{\mathrm{im}}+N_{\mathrm{ex}}} \boldsymbol{L}^{(ij)} \left(\boldsymbol{v}^{(j)}_{n} + \Delta t \sum_{l=1}^{k-1} a^{\mathrm{ex}}_{k,l} \boldsymbol{u}^{(j)}_{l} \right)
\end{aligned} \tag{13}$$

for implicit subdomains.

The hybrid IMEX scheme does not need temporal interpolation at the interfaces between explicit and implicit regions. To our understanding, the hybrid IMEX scheme is very desirable for a DGTD system with well separated CFL numbers, while the local time stepping scheme may be more suitable for a DGTD system with CFL numbers spanning continuously from a very small value to a relatively large one.

5 Conclusions

In this paper we have reviewed some important concepts, formulations, and implementations of discontinuous Galerkin time domain schemes for multiscale electromagnetic simulations, in particular, the mixed finite element discretization and the hybrid implicit-explicit (IMEX) time stepping scheme. Numerical examples demonstrate that the proposed method is a promising time-domain technique for simulating multiscale structures.

Bibliography

[1] J. Chen, and Q. H. Liu, “Discontinuous Galerkin time domain methods for multiscale electromagnetic simulations: A review,” *Proc. IEEE*, in press, 2013.

[2] K. Yee, “Numerical solution of initial boundary value problems involving Maxwell’s equations in isotropic media,” *IEEE Trans. Antennas Propagat.*, vol. 14, no. 3, pp. 302–307, May 1966.

[3] A. Taflove and S. C. Hagness, *Computational Electrodynamics: The Finite-Difference Time-Domain Method*, 3rd edition, Boston: Artech House, Inc., 2005.

[4] C. Sun and C. W. Trueman, “Three-dimensional subgridding algorithm for FDTD,” *IEEE Trans. Antennas Propagat.*, vol. 45, no. 3, pp. 422–429, March 1997.

[5] A. Cangellaris, C. Lin, and K. Mei, “Point-matched time domain finite element methods for electromagnetic radiation and scattering,” *IEEE Trans. Antennas Propagat.*, vol. 35, no. 10, pp. 1160–1173, Oct. 1987.

[6] J. F. Lee and Z. Sacks, “Whitney elements time domain (WETD) methods,” *IEEE Trans. Magn.*, vol. 31, no. 3, pp. 1325–1329, May 1995.

[7] B. Cockburn, F. Li, and C. W. Shu, “Locally divergence-free discontinuous Galerkin methods for the Maxwell equations,” *J. Comput. Phys.*, vol. 194, no. 2, pp. 588–610, March 2004.

[8] Q. H. Liu and G. Zhao, "Advances in PSTD techniques." Chapter 17, in *Computational Electromagnetics: The Finite-Difference Time-Domain Method*, A. Taflove and S. C. Hagness, Ed., Boston: Artech House, Inc., 2005.

[9] T. Xiao and Q. H. Liu, "Three-dimensional unstructured-grid discontinuous Galerkin method for Maxwell's equations with well-posed perfectly matched layer," *Microw. Opt. Techn. Lett.*, vol. 46, no. 5, pp. 459–463, Sept. 2005.

[10] J. S. Hesthaven, and T. Warburton, "Nodal high-order methods on unstructured grids: I. time-domain solution of Maxwell's equations," *J. Comput. Phys.*, vol. 181, no. 1, pp. 186–221, Sept. 2002.

[11] G. C. Cohen, X. Ferrieres, and S. Pernet, "A spatial high-order hexahedral discontinuous Galerkin method to solve Maxwell's equations in time domain," *J. Comput. Phys.*, vol. 217, no. 2, pp. 340–363, Sept. 2006.

[12] F. Q. Hu, M. Y. Hussaini, and P. Rasetarinera, "An analysis of the discontinuous Galerkin method for wave propagation problems," *J. Comput. Phys.*, vol. 151, no. 2, pp. 921–946, May 1999.

[13] J. S. Hesthaven and T. Warburton, *Nodal Discontinuous Galerkin Methods*, New York, NY: Springer, 2008.

[14] S. Gedney, C. Luo, J. Roden, R. Crawford, B. Guernsey, J. Miller, T. Kramer, and E. W. Lucas, "The discontinuous Galerkin finite-element time-domain method of Maxwell's equations," *ACES Journal*, vol. 24, no. 2, pp. 129–142, April 2009.

[15] H. Fahs and S. Lanteria, "A high-order non-conforming discontinuous Galerkin method for time-domain electromagnetics," *J. Comput. Phys.*, vol. 234, no. 4, pp. 1088–1096, June 2010.

[16] J. S. Hesthaven and T. C. Warburton, "Nodal high-order methods on unstructured grids - 1. Time-domain solution of Maxwell's equations," *J. Comput. Phys.*, vol. 181, no. 1, pp. 186–221, Sept. 2002.

[17] J. H. Lee, J. Chen, and Q. H. Liu, "A 3-D discontinuous spectral element time-domain method for Maxwell's equations," *IEEE Trans. Antennas Propag.*, vol. 57, no. 9, pp. 2666–2674, Sept. 2009.

[18] N. Marais and D. B. Davidson, "Numerical evaluation of high-order finite element time domain formulations in electromagnetics," *IEEE Trans. Antennas Propag.*, vol. 56, no. 12, pp. 3743–3751, Dec. 2008.

[19] J. C. Nédélec, "Mixed finite elements in $\mathbb{R}^3$," *Numer. Math.*, vol. 35, no. 3, pp. 315–341, Sept. 1980.

[20] A. Bossavit, "A rationale for 'edge-elements' in 3-D fields computations," *IEEE Trans. Magn.*, vol. 24, no. 1, pp. 74–79, Jan. 1988.

[21] A. F. Peterson, S. L. Ray, and R. Mittra, *Computational Methods for Electromagnetics*, IEEE Press, 1998.

[22] J. Jin, *The Finite Element Method in Electromagnetics*, 2nd edition, New York, NY: John Wiley & Sons, Inc., 2002.

[23] V. Shankar, A. H. Mohammadian, and W. F. Hall, "A time-domain, finite-volume treatment for the Maxwell equations," *Electromagnetics*, vol. 10, no. 1, pp. 127–145, Jan. 1990.

[24] A. H. Mohammadian, V. Shankar, and W. F. Hall, "Computation of electromagnetic scattering and radiation using a time-domain finite-volume discretization procedure," *Comput. Phys. Commun.*, vol. 68, no. 1–3, pp. 175–196, Nov. 1991.

[25] E. Montseny, S. Pernet, X. Ferrieres, and G. Cohen, "Dissipative terms and local time-stepping improvements in a spatial high order discontinuous Galerkin scheme for the time-domain Maxwell's equations," *J. Comput. Phys.*, vol. 227, no. 14, pp. 6795–6820, Jul. 2008.

[26] J. Chen, L. E. Tobon, M. Chai, J. A. Mix, and Q. H. Liu, "Efficient implicit-explicit time stepping scheme with domain decomposition for multiscale modeling of layered structures," *IEEE Trans. Compon., Packag., Manuf. Technol.*, vol. 1, no. 9, pp. 1438–1446, Sept. 2011.

[27] G. Cohen and M. Durufle, "Non-spurious spectral like element methods for Maxwell's equations," *J. Comput. Math.*, vol. 25, no. 3, pp. 282–300, 2007.

[28] J.H. Lee and Q.H. Liu, "An efficient 3-D spectral element method for Schrödinger equation in nanodevice simulation," *IEEE Trans. Comput.-Aided Design Integr. Circuits Syst.*, vol. 24, no. 12, pp. 1848–1858, Dec. 2005.

[29] S. Piperno, "Symplectic local time-stepping in non-dissipative DGTD methods applied to wave propagation problems," *ESAIM-Math. Model. Num.*, vol. 40, no. 5, pp. 815–841, Sept. 2006.

[30] S. Schomann, N. Godel, T. Warburton, and M. Clemens, "Local timestepping techniques using Taylor expansion for modeling electromagnetic wave propagation with discontinuous Galerkin-FEM," *IEEE Trans. Magn.*, vol. 46, no. 8, pp. 3504–3507, Aug. 2010.

[31] A. Kanevsky, M. H. Carpenter, D. Gottlieb, and J. S. Hesthaven, "Application of implicit-explicit high order Runge-Kutta methods to discontinuous-Galerkin schemes," *J. Comput. Phys.*, vol. 225, no. 2, pp. 1753–1781, Aug. 2007.

[32] J. C. Butcher, *Numerical Methods for Ordinary Differential Equations*, New York, NY: John Wiley & Sons, Inc., 2003.

Generalized complex inductance for radiation problems

Lap K. Yeung and **Ke-Li Wu**
Department of Electronic Engineering,
The Chinese University of Hong Kong, Shatin, NT, Hong Kong,
e-mail: lkyeung@ee.cuhk.edu.hk

Abstract

The concept of generalized complex inductance for the partial element equivalent circuit (PEEC) technique is introduced to model microstrip radiation problems. Using the semi-analytical Greens functions for microstrip substrates, the imaginary part of this generalized complex inductance can be shown to represent a frequency-dependent resistance containing information about the losses from spatial radiations (spherical and lateral) and surface waves (cylindrical). Hence, different radiation components can be derived separately, providing a useful and unique feature for representing high-speed/high frequency microstrip structures and antennas in the network domain.

1 Introduction

Although the partial element equivalent circuit (PEEC) technique [1–3] has been successfully applied for analyzing a wide range of electromagnetic problems, including electromagnetic compatibility, electromagnetic interference, as well as signal integrity for high-speed electronic circuits, its ability to handle radiation problems has not been considered thoroughly. Recently, a radiation model for the PEEC technique has been proposed for the free-space case [4]. This model makes use of the concept of generalized complex inductance to account for the radiation effect and the corresponding PEEC model can be used as a starting point to extract essential information on the radiation characteristics of the structure being investigated. In this work, the radiation model is extended to the case of modeling microstrip circuits and antennas. By using the Green's functions for microstrip substrates, it can

---

Pulsed Electromagnetic Fields: Their Potentialities, Computation and Evaluation
I. E. Lager and L. J. Jiang (Eds.).
doi: 10.3233/978-1-61499-230-1-65

be shown that the imaginary part of the inductance represents a frequency-dependent resistance containing contributions from spatial radiation and surface waves. The resulting equivalent circuits employing this generalized complex inductance concept require no ‘non-conservative’ capacitors, and the (quasi-)static condition for the capacitive components is preserved.

2 Theory

2.1 Single-layered microstrip Greens functions

Magnetic vector and electric scalar Greens functions for microstrip structures are usually expressed in terms of Sommerfeld integral as

$$G = \int \tilde{G}\left(k_\rho\right) H_0^{(2)}\left(k_\rho \rho\right) k_\rho \mathrm{d}k_\rho \tag{1}$$

where $\tilde{G} = \tilde{G}_A^{xx}$ or $\tilde{G}_\phi$ is the corresponding Greens function in the spectral domain, and $H_0^{(2)}$ is the Hankel function of the second kind. In order to compute this integral, a variety of techniques can be used. In general, for a single-layered microstrip substrate, the two spectral-domain Greens functions can be decomposed into three parts [5] as

$$\tilde{G} = \tilde{G}_0 + \tilde{G}_{\mathrm{SW}} + \frac{F}{\mathrm{j}2k_{z0}}. \tag{2}$$

Notice that $k_{z0}^2 = k_0^2 - k_\rho^2$. The first two terms in (2) represent, respectively, the asymptotic ($k_\rho \to \infty$) and surface-wave components of the Greens function. The last term F is the ‘leftover’ for which the first two components do not cover.

In this work, the asymptotic and the ‘leftover’ components are considered together as they both contribute to radiation into free space. In this sense, Eq. (2) should be rewritten as

$$\tilde{G} = \left(\tilde{G}_0 + \frac{F}{\mathrm{j}2k_{z0}}\right) + \tilde{G}_{\mathrm{SW}} = \tilde{G}_{\mathrm{SP}} + \tilde{G}_{\mathrm{SW}} \tag{3}$$

The corresponding spatial domain Greens functions can be obtained through (1).

2.2 Generalized complex inductance

The ‘non-conservative’ capacitance issue can be overcome by extracting only the (quasi-)static portion of the electric scalar Greens function for calculating the shorted-circuit capacitance matrix and moving its frequency-dependent portion to the inductance matrix. It is, mathematically, done by separating $G_{\phi,\mathrm{SP}}$ into two parts as

$$G^0_{\phi,\mathrm{SP}} = G_{\phi,\mathrm{SP}} \quad \text{with } k_0 \to 0 \tag{4}$$

$$G^{\mathrm{f}}_{\phi,\mathrm{SP}} = G_{\phi,\mathrm{SP}} - G^0_{\phi,\mathrm{SP}}. \tag{5}$$

This treatment then leads to the coefficient of potential as

$$\begin{aligned} pp_{i,n} = pp^0_{i,n} + pp^{\mathrm{f}}_{i,n} = \frac{1}{a_i a_n} \iint G^0_{\phi,\mathrm{SP}}\, \mathrm{d}s'_n \mathrm{d}s_i \\ + \frac{1}{a_i a_n} \iint \left(G^{\mathrm{f}}_{\phi,\mathrm{SP}} + G_{\phi,\mathrm{SP}} \right) \mathrm{d}s'_n \mathrm{d}s_i \end{aligned} \tag{6}$$

between capacitive mesh i and mesh n. The frequency-dependent second integral is used only for generating the inductive matrix.

The mutual inductance between two inductive meshes (l and m) or self-inductance ($l = m$) is given by

$$L_{l,m} = \frac{1}{w_l w_m} \iint \left(G^{xx}_{\mathrm{A,SP}} + G^{xx}_{\mathrm{A,SW}} \right) \mathrm{d}s'_n \mathrm{d}s_i. \tag{7}$$

It is generally a complex number. As there is no matrix inversion involved here, the imaginary part does produce a physically meaningful self-resistance ($l = m$). Now, by absorbing the second integral in (6) into the inductance term (7), a generalized self- and mutual inductance is formed. The resulting generalized inductance becomes (see Fig. 1)

$$\bar{L}_{l,m} = L_{l,m} + \frac{pp^{\mathrm{f}+}_{l,n_1}}{\omega^2} - \frac{pp^{\mathrm{f}-}_{l,n_1}}{\omega^2} - \frac{pp^{\mathrm{f}+}_{l,n_2}}{\omega^2} + \frac{pp^{\mathrm{f}-}_{l,n_2}}{\omega^2}. \tag{8}$$

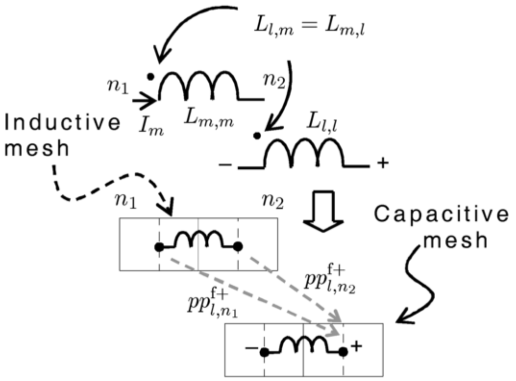

Figure 1: Coupling configuration between inductors l and m.

The significance of introducing such generalized inductance is that it not only correctly accounts for the radiation effect, but also preserves the physical meaning of the capacitance matrix.

3 Results

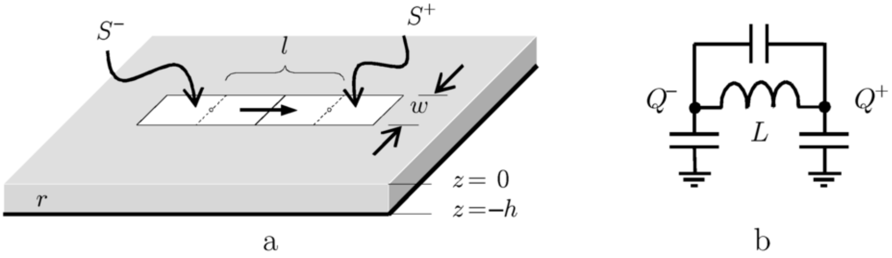

Figure 2: Short dipole on microstrip substrate. (a) Physical configuration; (b) equivalent circuit.

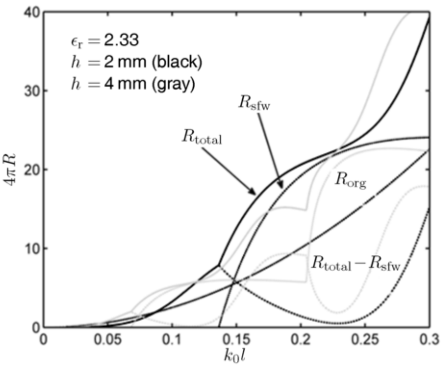

Figure 3: Radiation resistance components of a short dipole on microstrip substrate for $h = 2\,\text{mm}$ and $h = 4\,\text{mm}$.

3.1 Short dipole on microstrip substrate

Following the discussion above, the real part of the term $\mathrm{j}\omega L$ (radiation resistance) of an short (infinitesimal) dipole on microstrip substrate (see Fig. 2) can be decomposed into four components including the original free-space term, the term due to quasi-static images, the surface-wave term, and the remaining term contributed by lateral waves and other higher order effects. Fig. 3 depicts the cases of $\epsilon_r = 2.33$, $h = 2\,\text{mm}$ and $h = 4\,\text{mm}$. It can be seen from the figure that, for the $h = 2\,\text{mm}$ case, the surface waves do not radiate ($R_{\text{sfw}} = 0$) until $k_0 l$ reaches ~0.13. At this point, the component ($R_{\text{total}} - R_{\text{sfw}}$) represents the power radiated into free-space drops significantly. A similar feature can be seen for the $h = 4\,\text{mm}$ case. In this case, the power radiated into free-space drops every time when a new surface wave mode starts propagating.

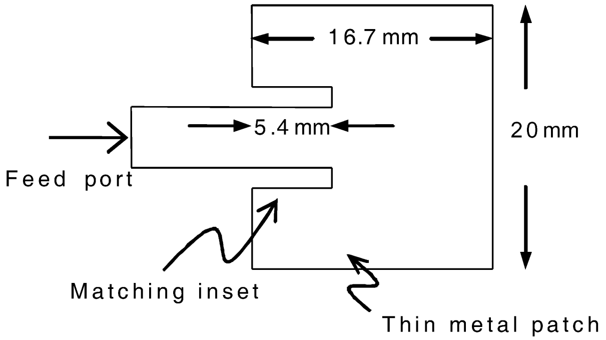

Figure 4: Geometry for the patch antenna.

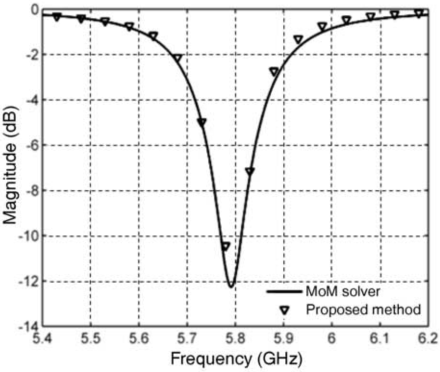

Figure 5: Simulated results ($|S_{11}|$) for the patch antenna with negligible surface waves.

3.2 Patch antenna

Another example to be studied is a patch antenna on thin substrate. The substrate used in this example has a dielectric constant of 2.33 and a thickness of 0.787 mm. As the substrate is thin and has a small value of dielectric constant, the surface wave contributions to the Greens functions are relatively insignificant at low frequencies. The size of the patch antenna (see Fig. 4) is 16.7 mm × 20 mm. It is fed by a microstrip with an inset of 5.4 mm to match to a 50 Ω transmission line. The geometry is divided into a total of 127 capacitive meshes and 222 inductive meshes, corresponding to a meshing scheme of ~30 meshes per (free-space) wavelength at 6.2 GHz. From the simulated results in Fig. 5, it is seen that the patch operates at around 5.8 GHz. The scattering parameters calculated by the PEEC technique using the concept of generalized complex inductance agree well with those from a MoM-based commercial EM solver.

4 Model reduction

Generally, it is not easy to obtain any physical insights by directly examining a PEEC-generated equivalent circuit. To obtain a more concise and physically intuitive circuit model, the model order reduction (MOR) technique described in [6] can be used. In this technique, most circuit nodes except the port nodes (nodes connecting to the source) of a PEEC-generated equivalent circuit are eliminated by using the $Y-\text{to}-\Delta$ transformation. Following a set of elimination criteria, the circuit can usually be simplified to containing only a few nodes. For the example shown in Fig. 6, if the dipole is electrically small, its equivalent circuit may be reduced to a pure capacitive circuit with only three capacitors (Fig. 7). It is important to notice that the inductive components get mixed with the capacitive components and vice versa during the reduction process and this leads to the final simplified circuit containing complex-valued capacitors as well.

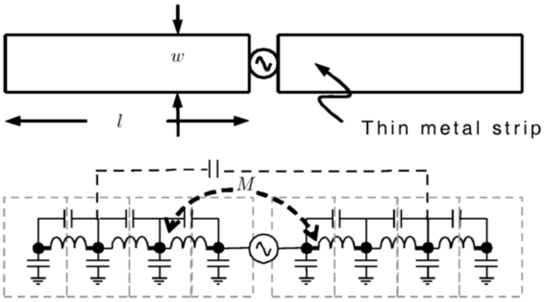

Figure 6: Short thin-strip dipole and its PEEC model.

An antenna is considered to be electrically small if it satisfies the inequality of $ka \leqslant 0.5$, where k is the free-space propagation constant and a is the radius of the smallest sphere that can completely encloses the antenna. Two short thin-strip dipoles, namely, a straight dipole and a meandered dipole (Fig. 8) are investigated here with $ka = 0.5$ at 4 GHz. Assuming there is no conductor loss, it is expected that the meandered dipole should have a smaller radiation quality (Q) factor when comparing to the straight

Table 1: Component values for the straight dipole.

f (GHz)	C_1 (F)	C_2 (F)
1	$1.41 \times 10^{-14} - j3.04 \times 10^{-18}$	$7.30 \times 10^{-14} - j2.23 \times 10^{-21}$
2	$1.44 \times 10^{-14} - j2.52 \times 10^{-17}$	$7.35 \times 10^{-14} - j7.31 \times 10^{-20}$
3	$1.49 \times 10^{-14} - j8.98 \times 10^{-17}$	$7.45 \times 10^{-14} - j5.76 \times 10^{-19}$
4	$1.57 \times 10^{-14} - j2.31 \times 10^{-16}$	$7.58 \times 10^{-14} - j2.57 \times 10^{-18}$

Table 2: Component values for the meandered dipole

f (GHz)	C_1 (F)	C_2 (F)
1	$4.50 \times 10^{-14} - j1.95 \times 10^{-17}$	$1.37 \times 10^{-13} - j7.79 \times 10^{-21}$
2	$5.09 \times 10^{-14} - j1.91 \times 10^{-16}$	$1.44 \times 10^{-13} - j2.97 \times 10^{-19}$
3	$6.53 \times 10^{-14} - j9.76 \times 10^{-16}$	$1.59 \times 10^{-13} - j3.12 \times 10^{-18}$
4	$1.08 \times 10^{-13} - j5.26 \times 10^{-15}$	$1.92 \times 10^{-13} - j2.37 \times 10^{-17}$

one. However this information cannot be seen by simply looking at their PEEC models. On the other hand, this can be easily confirmed from the concise circuit models derived by the algorithm discussed above. In both cases, their PEEC-generated equivalent circuits can be simplified to the one shown in Fig. 7 with the corresponding components values listed in Table 1 and Table 2, respectively.

By looking at the concise circuit models for these two antennas, it is clear that they are both electric-type within the operating frequency band of interest (<4 GHz) because they can be modeled by a circuit with only capacitors. Another interesting fact is that these complex-valued capacitors have their imaginary values increase with the operating frequency. In fact, the imaginary part of such a capacitor represents its loss from radiation. When looking into the excitation port, the circuit in Fig. 7 can be further

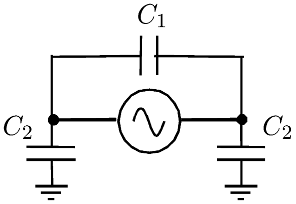

Figure 7: Short thin-strip dipole and its PEEC model.

simplified to just a single capacitor of value $C = C_1 + C_2/2$. Its quality factor is approximately the radiation Q factor of the antenna. Fig. 9 shows the excitation port admittance and the approximated Q factors for the two antennas at different operating frequencies. It can be seen from the figure that the radiation resistance (conductance) of the meandered dipole increases rapidly when ka approaching 0.5. To verify the accuracy of our simplified circuit models, results (solid lines) obtained from a commercial full-wave electromagnetic solver are also shown and they agree well with each other.

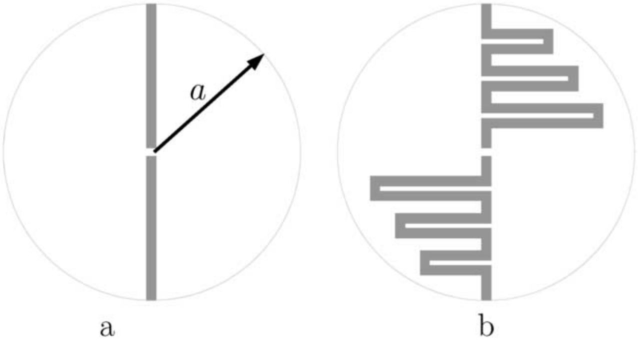

Figure 8: Straight (a) and meandered (b) small dipoles.

5 Conclusions

A new PEEC formulation, which incorporates the concept of generalized complex inductance, for modeling of microstrip structures has been introduced. In this PEEC formulation, the radiation loss is taken into account by having complex-valued inductors in the equivalent circuit. And through these inductors, contributions from various radiation mechanisms, such as spatial and surface waves, to the overall radiation are revealed. In addition, a technique to automatically derive a concise and physically intuitive equivalent circuit model for an electrically small radiating structure is presented. Important information such as radiation resistance, capacitive and inductive storage energy of the structure can be identified directly by examining this concise circuit model. In addition, such a circuit model can readily be incorporated into other higher level design exercises so that impacts of the structure on the overall system performance can easily be simulated. The proposed algorithm is, therefore, useful for modern integrated high-speed/high-frequency circuit design.

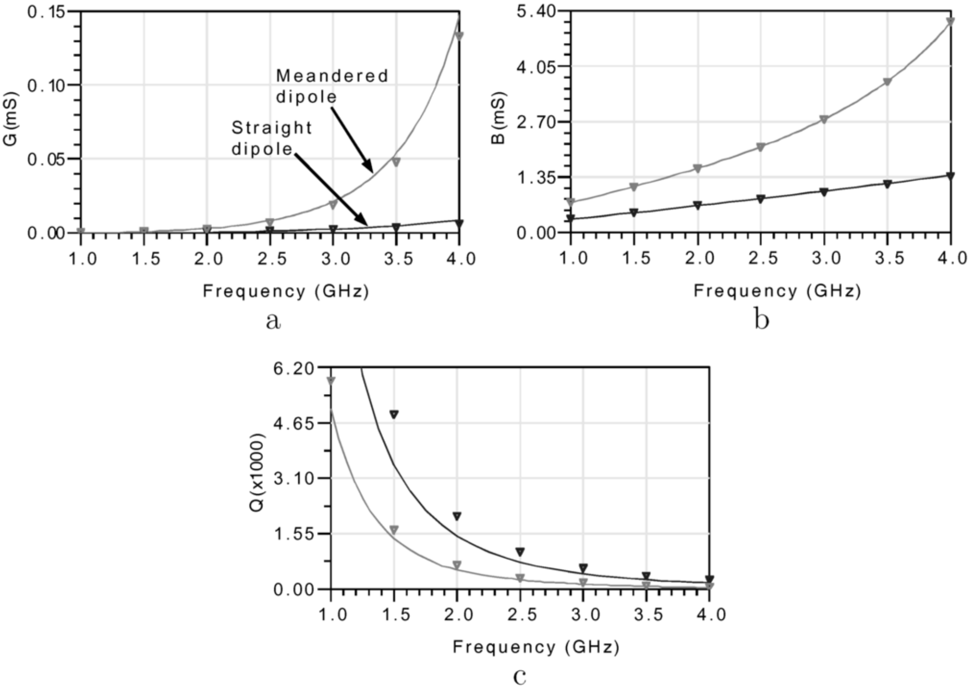

Figure 9: Simulated port for the two example dipoles. (a) Conductance; (b) susceptance; (c) approximated radiation Q factors.

Acknowledgment

The authors wish to acknowledge the supports from University Grants Committee of Hong Kong under Grant AoE/P-04/08 and Innovation Technology Commission of Hong Kong under Grant ITS/019/10.

Bibliography

[1] A. Ruehli, “Equivalent circuit models for three dimensional multiconductor systems,” *IEEE Trans. Microwave Theory Tech.*, vol. 22, no. 3, pp. 216–221, March 1974.

[2] H. Heeb and A. Ruehli, “Three-dimensional interconnect analysis using partial element equivalent circuits,” *IEEE Trans. Circuits and Systems*, vol. 39, no. 11, pp. 974–982, Nov. 1992.

[3] A. Ruehli, “Circuit models for three-dimensional geometries including dielectrics,” *IEEE Trans. Microwave Theory Tech.*, vol. 40, no. 7, pp. 1507–1516, July 1992.

[4] L. K. Yeung and K.-L. Wu, “Generalized partial element equivalent circuit (PEEC) modeling with radiation effect,” *IEEE Trans. Microwave Theory Tech.*, vol. 59, no. 10, pp. 2377–2384, Oct. 2011.

[5] Y. Chow, J. Yang, D. Fang, and G. Howard, “A closed-form spatial Greens function for the thick microstrip substrate,” *IEEE Trans. Microwave Theory Tech.*, vol. 39, no. 3, pp. 588–592, July 1991.

[6] J. Wang and K.-L. Wu, “A derived physically expressive circuit model for multilayer RF embedded passives,” *IEEE Trans. Microwave Theory Tech.*, vol. 54, no. 5, pp. 1961–1968, May 2006.

Generalized-ray theory for electromagnetic fields in layered media

Martin Štumpf[†,§], **Adrianus T. de Hoop**[‡],
and **Guy A. E. Vandenbosch**[†]

[†]*ESAT–Telecommunications & Microwaves, Katholieke Universiteit Leuven, Kasteelpark Arenberg 10, B-3001 Heverlee (Leuven), Belgium,*
e-mail: martin.stumpf@esat.kuleuven.be

[‡]*Delft University of Technology,*
Faculty of Electrical Engineering, Mathematics and Computer Science,
Mekelweg 4, 2628 CD Delft, the Netherlands

[§]*Brno University of Technology, SIX Research Centre,*
Purkyňova 118, 612 00 Brno, the Czech Republic

Abstract

Generalized-ray theory for time-domain electromagnetic fields in a horizontally layered medium is developed. After introducing appropriate integral transformations and source-type field representations in vertically inhomogeneous media, the solution is written out in terms of generalized ray constituents whose space-time counterparts are constructed with the aid of the Cagniard-DeHoop technique. The formulation lays the foundation to rigorously study time domain field behavior in numerous practical topologies where a stratified multilayer is involved, such as planar antennas and circuits, but also EMC and propagation problems.

1 Introduction

The ever increasing bit rates in digital electronic and electrical signal generation, transmission, propagation and reception in a wide field of technical applications such as microelectronic devices, inter- and intra-device wireless signal transfer and the next generation of mobile communication, put severe demands on the computational tools for designing such devices. The kind

---

Pulsed Electromagnetic Fields: Their Potentialities, Computation and Evaluation
I. E. Lager and L. J. Jiang (Eds.).
doi: 10.3233/978-1-61499-230-1-75

of structures we are interested in can be considered as a limited number of geometrical addenda imposed on a background structure of mutually parallel layers of different constitution including impenetrable interfaces. To the knowledge of the authors, electromagnetic time-domain signals have never been studied in a general multilayered medium. This in contrast to frequency domain, where literally hundreds of papers have been published on this topic. Here, standard ways of handling multilayered media is to apply Sommerfeld's theory established as early as in 1909 [1]. In this respect, initial attempts to tackle the simplest structures and related numerical issues can be traced back to the late 1970s [2]. Further research in subsequent decades was mainly focused on various mixed-potential formulations [3–6] and on a numerical handling of Sommerfeld's integrals [7, 8]. For a detailed list of references on the subject we refer the reader to a review paper by Michalski and Mosig [9].

The most efficient tool for analysis of multilayered structures is the boundary integral equation method. The propagation in such a stratified medium can be handled analytically, because the relevant Green's functions admit an analytical represention in the transform domain. Adhering to the flexibility and the versatility of surface integral equation techniques (with their lower dimensionality), and considering the great successes reached with Green's function formulations in the frequency domain, the principal task in this paper is to construct expressions for the time-domain Green's functions involved. For homogeneous isotropic subdomains such Green's functions are well-known and easily implemented, but for a background with stratification no simple expressions exist. However, such expressions can be derived by applying a sophisticated mathematical tool known as the "Cagniard-DeHoop technique" [10]. It has been originally developed by Cagniard for seismic wave propagation problems [11, 12] and later considerably simplified by De Hoop. It has found a wealth of applications in various branches of physics, for example, in acoustics [13], elastodynamics [14] and electromagnetics [15–17]. Initial efforts in antenna and microwave engineering can be found in [18], where Xia et al. introduce time-domain Green's functions for a microstrip structure based on the Cagniard-DeHoop method with the time Fourier transform [19, Ch. 4]. More recently, the pulse-excited electromagnetic radiation from elementary slot antennas is described by De Hoop et al. [20]. As far as generalizations of the method are concerned, the Cagniard-DeHoop method is capable of handling arbitrarily anisotropic solid media [21], continuously layered fluid media [22] as well as dielectric media with conductive losses [23].

Scientifically, the construction of the time-domain Green's function for the EM field in multilayered media is based upon a number of ingredients.

First of all, the nature of the geometrical configuration requires a consistent decomposition of the relevant field quantities as well as the pertaining field equations into components parallel to the interfaces of the layers and components perpendicular to them. Secondly, the spatial shift invariance of the configuration in the plane parallel to the interfaces has to be appropriately accounted for. In the Cagniard-DeHoop technique this is done by introducing for the field components the so-called *wave slowness representation*. This representation employs a one-sided Laplace transformation with respect to time with positive real transform parameter, which parameter is subsequently used as a scaling paramater in the spatial Fourier representation parallel to the layering. In the slowness domain then a one-dimensional wave propagation problem results in the direction normal to the layering, whose constituents are written as being generated by the source that excites the field upon which constituents successively reflected against and transmitted across interfaces are introduced. Each traversal across the layer takes the required propagation time, as a consequence of which the total number of constituents within any prescribed time window of observation is finite.

Generalized ray theory for horizontally multilayered media can be in literature found in connection with elastodynamics and acoustics, mainly for geophysical applications [24, 25]. The theory for a horizontally layered solid was given by Pao and Gajewski [26] using the original Cagniard's technique. To the best knowledge of the authors, a proper electromagnetic formulation is missing in literature. The theory for electromagnetic fields presented in this paper partially leans on the wave-matrix formalism developed for impulsive acoustic field radiation in a discretely multilayered fluid given by De Hoop [27]. However, the vector nature of electromagnetic fields leads to source-type representations for the electric and the magnetic field strengths via potential functions. Here, no postulate of potential functions [9, 28] is required and the representations are constructed directly from the field equations and the pertaining interface conditions. Finally, the transform-domain solution is written out in terms of generalized-ray constituents which are subsequently transformed to space-time by applying the Cagniard-DeHoop method.

The presented theory can find wide applications in computational electromagnetics serving as a basis for time-domain surface-integral equation techniques in stratified media. It can contribute to the solution of time-domain related antenna and circuit design problems, and EMC and propagation problems. With the generation of ultra short pulses in terahertz EM fields, the method is expected to play an illuminating role in the explanation of the (time-domain) phenomena involved [29].

2 Problem description

The problem under consideration is given in Fig. 1. It consists of a stratified medium with electromagnetic properties varying in vertical direction only. The position in the problem configuration is localized by the coordinates $\{x_1, x_2, x_3\}$ with respect to a fixed, orthogonal Cartesian reference frame. The spatial reference frame is defined with respect to the origin O and the three mutually perpendicular base vectors $\{\boldsymbol{i}_1, \boldsymbol{i}_2, \boldsymbol{i}_3\}$ of unit length each; they form, in the indicated order, a right-handed system. The subscript notation for Cartesian tensors with the summation convention for repeated subscripts is employed [30, Sec. A.2]. The Levi-Civita tensor (completely antisymmetrical unit tensor of rank 3) is $\boldsymbol{e}_{k,m,p} = 1$ for $\{k, m, p\}$ = even permutation of $\{1, 2, 3\}$, $\boldsymbol{e}_{k,m,p} = -1$ for $\{k, m, p\}$ = odd permutation of $\{1, 2, 3\}$ and $\boldsymbol{e}_{k,m,p} = 0$ in all other cases and the Kronecker tensor (symmetrical unit tensor of rank 2) is $\delta_{i,j} = 1$ for $i = j$ and $\delta_{i,j} = 0$ for $i \neq j$ [30, Sec. A.7]. Lower-case Latin subscripts stand for the values $\{1, 2, 3\}$ while lower-case Greek subscripts stand for the values $\{1, 2\}$ only. Within the reference frame, the position of a point is defined by the position vector $\boldsymbol{x} = x_k \boldsymbol{i}_k$, $\boldsymbol{x} \in \mathbb{R}^3$. The spatial differentiation with respect to x_m is denoted by ∂_m. The time coordinate is denoted by t and symbol ∂_t is reserved for the partial differentiation with respect to time.

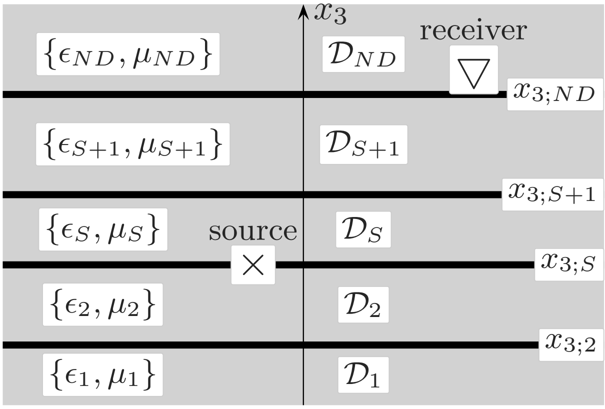

Figure 1: Horizontally layered medium in which electromagnetic waves are generated by an impulsive point-source.

The layered medium consists of ND domains each of which is characterized by the corresponding electric permittivity $\epsilon_N = \epsilon_N(x_3)$, magnetic permeability $\mu_N = \mu_N(x_3)$, $N = \{1, ..., ND\}$ and by its thickness $d_N = x_{3;N+1} - x_{3;N}$ for $N = \{2, ..., ND - 1\}$. The corresponding electromagnetic wave speed is $c_N = (\epsilon_N \mu_N)^{-1/2} > 0$. Both electric permittivity and magnetic permeability are assumed to be real-valued, positive and piecewise constant functions of x_3 only. On account of this property, the problem configuration is linear, instantaneously reacting, time invariant and shift invariant in the $x_1 - x_2$ plane. Loss mechanisms are not incorporated.

The electromagnetic field is radiated by an impulsive source that is located at the source level $x_3 = x_{3;S}$ placed at the interface of two domains with nonzero or zero contrast in electromagnetic properties. The latter can be considered as the source placed within one domain. Consequently, the response is probed at the receiving point that can be defined either at the interface or within a domain. If an observed quantity shows a jump discontinuity across the interface, then the receiver is placed just below or just above the interface. It is assumed that a source starts to act at $t = 0$ and that prior to this instant the electromagnetic fields vanish throughout the configuration (initial condition).

3 Definition of the field problem

In each subdomain of the configuration, the electric field strength E_k and the magnetic field strength H_p are continuously differentiable functions with respect to x_k and t and satisfy the electromagnetic field equations [30, Sec. 18.3]

$$-\boldsymbol{e}_{k,m,p}\partial_m H_p + \epsilon\partial_t E_k = -J_k \tag{1}$$

$$\boldsymbol{e}_{j,n,r}\partial_n E_r + \mu\partial_t H_j = -K_j \tag{2}$$

where J_k is the volume electric current density and K_j is the volume magnetic current density defined for a point source at $(0, 0, x_{3;S})$ as

$$\{J_k, K_j\}(\boldsymbol{x}, t) = \{j_k, k_j\}(t)\delta(x_1, x_2, x_3 - x_{3;S}) \tag{3}$$

We assume that $\{j_k, k_j\}(t) = \{0, 0\}$ for $t < 0$. The electromagnetic field equations (1)–(2) are across interfaces supplemented by the boundary conditions

$$\lim_{x_3 \downarrow x_{3;N}} H_\pi - \lim_{x_3 \uparrow x_{3;N}} H_\pi = \boldsymbol{e}_{3,\pi,\kappa} j_\kappa(t)\delta(x_1, x_2)\delta_{N,S} \tag{4}$$

$$\lim_{x_3 \downarrow x_{3;N}} E_\rho - \lim_{x_3 \uparrow x_{3;N}} E_\rho = \boldsymbol{e}_{3,\iota,\rho} k_\iota(t)\delta(x_1, x_2)\delta_{N,S} \tag{5}$$

for all $t \in \mathbb{R}$, $x_\nu \in \mathbb{R}$, $N = \{2, ..., ND\}$. To solve the electromagnetic field equations (1)–(2) with the interface boundary conditions (4)–(5) and the initial condition, we apply the integral transformations that take the advantage of the time invariance and the shift invariance in the $x_1 - x_2$ plane.

4 Transform-domain field representation

Space-time expressions for the electromagnetic field radiated from impulsive sources will be constructed using the Cagniard-DeHoop technique [10]. The technique employs a unilateral one-sided Laplace transformation with respect to time

$$\hat{E}_k(\boldsymbol{x}, s) = \int_{t=0}^{\infty} \exp(-st) E_k(\boldsymbol{x}, t) \mathrm{d}t \tag{6}$$

in which s is taken real-valued and positive relying on Lerch's uniqueness theorem [31, Sec. 5]. The theorem states that uniqueness of the inverse transformation is ensured under the weaker condition that $\hat{E}_k(\boldsymbol{x}, s)$ is specified at the sequence (Lerch's sequence) of real s values: $\mathcal{L} = \{s \in \mathbb{R}; s_n = s_0 + nh, s_0 > 0, h > 0, n = 0, 1, 2, ...\}$. Subsequently, the wave slowness representation parallel with respect to the layering is used

$$\hat{E}_k(\boldsymbol{x}, s) = \left(\frac{s}{2\pi}\right)^2 \int_{\alpha_2 \in \mathbb{R}} \mathrm{d}\alpha_1 \int_{\alpha_2 \in \mathbb{R}} \exp(-\mathrm{i} s \alpha_\mu x_\mu) \tilde{E}_k(\alpha_1, \alpha_2, x_3, s) \mathrm{d}\alpha_2 \tag{7}$$

involving the real values of the complex wave slowness parameters α_μ. Upon applying (6)–(7) to (1)–(5) we arrive at the transform-domain field equations

$$-\boldsymbol{e}_{k,m,p} \tilde{\partial}_m \tilde{H}_p + s\epsilon \tilde{E}_k = -\tilde{J}_k \tag{8}$$

$$\boldsymbol{e}_{j,n,r} \tilde{\partial}_n \tilde{E}_r + s\mu \tilde{H}_j = -\tilde{K}_j \tag{9}$$

with

$$\{\tilde{J}_k, \tilde{K}_j\}(\alpha_1, \alpha_2, x_3, s) = \{\hat{\jmath}_k, \hat{k}_j\}(s) \delta(x_3 - x_{3;S}) \tag{10}$$

and the corresponding transform-domain interface boundary conditions

$$\lim_{x_3 \downarrow x_{3;N}} \tilde{H}_\pi - \lim_{x_3 \uparrow x_{3;N}} \tilde{H}_\pi = \boldsymbol{e}_{3,\pi,\kappa} \hat{\jmath}_\kappa(s) \delta_{N,S} \tag{11}$$

$$\lim_{x_3 \downarrow x_{3;N}} \tilde{E}_\rho - \lim_{x_3 \uparrow x_{3;N}} \tilde{E}_\rho = \boldsymbol{e}_{3,\iota,\rho} \hat{k}_\iota(s) \delta_{N,S} \tag{12}$$

for all $s \in \mathcal{L}$, $\alpha_\nu \in \mathbb{R}$, $N = \{2, ..., ND\}$ and with $\tilde{\partial}_\kappa = -\mathrm{i} s \alpha_\kappa$, $\tilde{\partial}_3 = \partial_3$. In the next step we will take the advantage of the geometrical properties of the problem configuration and decompose the transform-domain field quantities and the field equations into components parallel to the interfaces of the layers and components perpendicular to them.

5 Transform-domain field decomposition

With regard to the geometry of the problem configuration, the transform-domain electromagnetic field equations (8)–(9) are decomposed as

$$-\boldsymbol{e}_{k,\mu,\pi}\tilde{\partial}_\mu\tilde{H}_\pi - \boldsymbol{e}_{k,\mu,3}\tilde{\partial}_\mu\tilde{H}_3 - \boldsymbol{e}_{k,3,\pi}\partial_3\tilde{H}_\pi + s\epsilon\tilde{E}_k = -\tilde{J}_k \qquad (13)$$

$$\boldsymbol{e}_{j,\nu,\rho}\tilde{\partial}_\nu\tilde{E}_\rho + \boldsymbol{e}_{j,\nu,3}\tilde{\partial}_\nu\tilde{E}_3 + \boldsymbol{e}_{j,3,\rho}\partial_3\tilde{E}_\rho + s\mu\tilde{H}_j = -\tilde{K}_j \qquad (14)$$

Upon decomposing the field quantities and eliminating the vertical ones $\{\tilde{E}_3, \tilde{H}_3\}$, after a few steps we arrive at

$$\begin{aligned}
&\partial_3^2\tilde{E}_\pi - s^2\gamma^2\tilde{E}_\pi \\
&= s\mu\tilde{J}_\pi - \tilde{\partial}_\pi\tilde{\partial}_\nu\tilde{J}_\nu/s\epsilon - \tilde{\partial}_\pi\partial_3\tilde{J}_3/s\epsilon - \boldsymbol{e}_{\pi,\rho,3}\partial_3\tilde{K}_\rho + \boldsymbol{e}_{\pi,\rho,3}\tilde{\partial}_\rho\tilde{K}_3 \qquad (15)\\
&\partial_3^2\tilde{H}_\rho - s^2\gamma^2\tilde{H}_\rho \\
&= s\epsilon\tilde{K}_\rho - \tilde{\partial}_\rho\tilde{\partial}_\pi\tilde{K}_\pi/s\mu - \tilde{\partial}_\rho\partial_3\tilde{K}_3/s\mu + \boldsymbol{e}_{\rho,\kappa,3}\partial_3\tilde{J}_\kappa - \boldsymbol{e}_{\rho,\kappa,3}\tilde{\partial}_\kappa\tilde{J}_3 \qquad (16)
\end{aligned}$$

Once the tangential field strengths are found, the vertical ones follow from Eqs. (13) and (14). The system of Eqs. (15)–(16) with the tangential electromagnetic field strengths as fundamental unknown quantities will serve as the point of departure for the next analysis. As will be shown, it clearly reveals a choice of potentials that represent the electromagnetic fields in a vertically inhomogeneous medium.

6 Source-type EM field representation in stratified media

The hypersingular spatial behavior of direct electric- and magnetic-type integral equation kernels invokes a need of using source-type field representations via potential functions that possess a weaker spatial singularity integrable over a surface domain. It is well-known from theory of electromagnetic fields in horizontally layered media that the fields excited by the vertically-oriented dipole can be represented using a single scalar function while a complete description of the fields due to the horizontally-oriented dipole requires at least two scalar functions [28]. Such scalar functions can be in a general formulation viewed either as components of the electric/magnetic Green's tensor or as scalar potentials. The commonly used approach in this respect postulates the components of the corresponding Green's tensor leading to various scalar potential functions. A number of choices have been previously discussed concerning the frequency-domain mixed-potential integral formulations [4, 6]. The source-type field representation formulated here naturally follows from the system of Eqs. (15)–(16). In view of the problem linearity, different types of sources appearing in the right-hand side of Eqs. (15)–(16) can be discussed separately. For the sake of conciseness, the results are provided for a vertical electric dipole only. For a complete description including the handling of horizontal sources we refer the reader to [32].

A general solution of Eqs. (15) and (16) corresponding to the vertical electric-current excitation (10) can be written as

$$\tilde{E}_\pi(\alpha_1, \alpha_2, x_3, s) = \tilde{\partial}_\pi \partial_3 \hat{j}_3(s) \tilde{G}^{J\perp}(\alpha_1, \alpha_2, x_3, s)/s\epsilon \tag{17}$$

$$\tilde{H}_\rho(\alpha_1, \alpha_2, x_3, s) = \boldsymbol{e}_{\rho,\pi,3} \tilde{\partial}_\pi \hat{j}_3(s) \tilde{G}^{J\perp}(\alpha_1, \alpha_2, x_3, s) \tag{18}$$

Using Eq. (18) in (13) and Eq. (17) in (14) gives the vertical electromagnetic components

$$\tilde{E}_3(\alpha_1, \alpha_2, x_3, s) = -s\mu \hat{j}_3(s) \tilde{G}^{J\perp} + \hat{j}_3(s) \partial_3^2 \tilde{G}^{J\perp}/s\epsilon \tag{19}$$

and $\tilde{H}_3(\alpha_1, \alpha_2, x_3, s) = 0$. Let the Green's function $\tilde{G}^{J\perp}$ corresponding to the solution in $\mathcal{D}_N$ be $\tilde{G}_N^{J\perp}$ for $N = \{1, ..., ND\}$. Then upon applying the interface boundary conditions (11)–(12) we get

$$\lim_{x_3 \downarrow x_{3;N}} \tilde{G}_N^{J\perp} - \lim_{x_3 \uparrow x_{3;N}} \tilde{G}_{N-1}^{J\perp} = 0 \tag{20}$$

$$\lim_{x_3 \downarrow x_{3;N}} \partial_3 \tilde{G}_N^{J\perp}/\epsilon_N - \lim_{x_3 \uparrow x_{3;N}} \partial_3 \tilde{G}_{N-1}^{J\perp}/\epsilon_{N-1} = -\delta_{N,S} \tag{21}$$

for $N = \{2, ..., ND\}$. The boundary conditions on impenetrable interfaces follow from Eqs. (17)–(18) as $\tilde{G}^{J\perp} = 0$ and $\partial_3 \tilde{G}^{J\perp} = 0$ upon approaching the Perfectly Magnetically Conducting (PMC) interface and the Perfectly Electrically Conducting (PEC) interface, respectively. Other source configurations are treated along the same lines.

7 Wawe-matrix formalism

In this section we provide the wave-matrix formalism for electromagnetic fields in layered media excited by the vertical electric-current excitation. The formulation is based on the methodology developed by De Hoop for acoustic waves in a layered fluid [27]. The handling of horizontal electromagnetic sources is much more involved [32] and is not discussed here.

A general solution satisfying the causality condition can be written as

$$\tilde{G}_N^{J\perp} = W_N^+ \exp[-s\gamma_N(x_3 - x_{3;N})] + W_N^- \exp[-s\gamma_N(x_{3;N+1} - x_3)] \tag{22}$$

in $\mathcal{D}_N$ for $N = \{1, ..., ND\}$, where the corresponding vertical propagation coefficient is given as

$$\gamma_N = \left(1/c_N^2 - \tilde{\partial}_\mu \tilde{\partial}_\mu / s^2\right)^{1/2} > 0 \tag{23}$$

for $s \in \mathcal{L}$, $\alpha_\nu \in \mathbb{R}$. In Eq. (22), $\{W_N^+, W_N^-\}$ are upogoing/downgoing transform-domain wave amplitudes in $\mathcal{D}_N$ with $\{W_1^+, W_{ND}^-\} = \{0, 0\}$ that are mutually related via scattering relations

$$W_N^+ = \bar{S}_N^{+-} W_N^- + \bar{S}_N^{++} W_{N-1}^+ + X_N^+ \tag{24}$$

$$W_{N-1}^- = \bar{S}_N^{--} W_N^- + \bar{S}_N^{-+} W_{N-1}^+ + X_{N-1}^- \tag{25}$$

with

$$\{\bar{S}_N^{+-}, \bar{S}_N^{--}\} = \{S_N^{+-}, S_N^{--}\} \exp(-s\gamma_N d_N) \tag{26}$$

$$\{\bar{S}_N^{++}, \bar{S}_N^{-+}\} = \{S_N^{++}, S_N^{-+}\} \exp(-s\gamma_{N-1} d_{N-1}) \tag{27}$$

for $N = \{2, ..., ND\}$, $d_N = x_{3;N+1} - x_{3;N}$. The wave amplitudes on the right-hand side of Eqs. (24)–(25) represent the waves propagating away from N-th interface that are related through the scattering/coupling matrix to the waves propagating toward the interface. The parameters $\{X_N^+, X_{N-1}^-\}$ then represent the source-coupling terms. The wave amplitudes in the structure consisting of ND domains with $ND - 1$ interfaces can be therefore related by the $(2ND - 2) \times (2ND - 2)$ scattering matrix with $4(ND - 2)$ scattering parameters.

In this way, the systems of linear equations can be shortly written as

$$\left[\boldsymbol{W}\right] = [\bar{\boldsymbol{S}}] \cdot \left[\boldsymbol{W}\right] + \left[\boldsymbol{X}\right] \tag{28}$$

and solved using a Neumann iterative procedure [33, Sec. 4.5] leading to

$$\left[\boldsymbol{W}\right] = \sum_{m=0}^{M} [\bar{\boldsymbol{S}}]^m \cdot \left[\boldsymbol{X}\right] + [\bar{\boldsymbol{S}}]^{M+1} \cdot \left[\boldsymbol{W}\right] \tag{29}$$

provided that $||\bar{\boldsymbol{S}}|| < 1$ which is always met for the analyzed problem configuration. Since the scattering matrices contain the Laplace transformation parameter only through the exponential factors that in space-time represent a time delay, each higher constituent in the sum of Eq. (29) arises at a later time than the previous one. Based on the fact that one is always interested in the wave field in a finite time window of observation, a finite number of constituents is sufficient to get the exact time-domain response. Moreover, the iterative procedure can be terminated once the constituents become negligible (below a prescribed treshold) due to the successive reflections and transmissions at the interfaces whose number increases with m.

The wave amplitudes of wave fields excited by the vertical electric dipole are at the N-th interface interrelated via the scattering parameters given by

$$S_N^{+-} = (\gamma_N/\epsilon_N - \gamma_{N-1}/\epsilon_{N-1})/(\gamma_N/\epsilon_N + \gamma_{N-1}/\epsilon_{N-1}) \tag{30}$$

$$S_N^{--} = (2\gamma_N/\epsilon_N)/(\gamma_N/\epsilon_N + \gamma_{N-1}/\epsilon_{N-1}) \tag{31}$$

$$S_N^{-+} = (\gamma_{N-1}/\epsilon_{N-1} - \gamma_N/\epsilon_N)/(\gamma_{N-1}/\epsilon_{N-1} + \gamma_N/\epsilon_N) \tag{32}$$

$$S_N^{++} = (2\gamma_{N-1}/\epsilon_{N-1})/(\gamma_{N-1}/\epsilon_{N-1} + \gamma_N/\epsilon_N) \tag{33}$$

for $N = \{2, ..., ND\}$. If an impenetrable interface is present, then we can find

$$S_2^{+-} = -1 \quad \text{or/and} \quad S_{ND}^{-+} = -1 \quad \text{on PMC} \tag{34}$$

$$S_2^{+-} = +1 \quad \text{or/and} \quad S_{ND}^{-+} = +1 \quad \text{on PEC} \tag{35}$$

The corresponding source-coupling coefficients differ from zero only at the source level

$$X_S^+ = X_{S-1}^- = 1/[s(\gamma_S/\epsilon_S + \gamma_{S-1}/\epsilon_{S-1})] \tag{36}$$

Once the scattering and source-coupling parameters are known, the transform-domain field description is completed. In the final step, the transform-domain constituents appearing in Eqs. (32) and (33) are transformed to the space-time domain using the Cagniard-DeHoop technique [10].

8 Conclusions

The source-type electromagnetic field representations in vertically inhomogeneous media have been constructed and the generalized-ray theory for electromagnetic fields in piecewise homogeneous horizontally layered media has been formulated.

The solution for electromagnetic fields propagating in layered media has been built up in terms of time-domain constituents successively arriving at a point of observation. The solution is exact up to the arrival time of the next time-domain constituent and can serve as a basis for the time-domain boundary integral equation techniques, for a time-domain modeling of electromagnetic field propagation in stratified problem configurations or for a benchmarking of purely numerical techniques.

Acknowledgment

This research was sponsored by the project CZ.1.07/2.3.00/30.0039 of the Brno University of Technology and by the FWO project G.0897.10N.

Bibliography

[1] A. Sommerfeld, "Über die Ausbreitung der Wellen in der drahtlosen Telegraphie," *Ann. Phys.*, vol. 333, no. 4, pp. 665–736, 1909.

[2] J. R. Mosig and F. E. Gardiol, "A dynamic vector potential theory for three-dimensional microstrip structures," *Bulletin AGEN*, vol. 26, pp. 45–52, Nov. 1978.

[3] J. R. Mosig and F. E. Gardiol, "General integral equation formulation for microstrip antennas and scatterers," *Inst. Elect. Eng. Proc.*, vol. 132, pt. H, pp. 424–432, Dec. 1985.

[4] K. A. Michalski, D. Zheng, Electromagnetic scattering and radiation by surfaces of arbitrary shape in layered media, part I: Theory," *IEEE Trans. Antennas Propag.*, vol. 38, no. 3, March 1990.

[5] G. A. E. Vandenbosch and A. R. van de Capelle, "Mixed-potential integral expression formulation of the electric field in a stratified dielectric medium – Application to the case of a probe current source," *IEEE Trans. Antennas Propag.*, vol. 40, no. 7, pp. 806–817, July 1992.

[6] M. Vrancken and G. A. E. Vandenbosch, "Semantics of dyadic and mixed potential field representation for 3-D current distributions in planar stratified media ," *IEEE Trans. Antennas Propag.*, vol. 51, no. 10, pp. 2778–2787, Oct. 2003.

[7] K. A. Michalski, "Extrapolation methods for Sommerfeld integral tails," *IEEE Trans. Antennas Propag.*, vol. 46, no. 10, pp. 1405–1418, Oct. 1998.

[8] F. J. Demuynck, G. A. E. Vandenbosch and A. R. van de Capelle, "The expansion wave concept – part I: Efficient calculation of spatial Green's functions in a stratified dielectric medium," *IEEE Trans. Antennas Propag.*, vol. 46, no. 3, pp. 1405–1418, March 1998.

[9] K. A. Michalski and J. R. Mosig, "Multilayered media Green's functions in integral equation formulations," *IEEE Trans. Antennas Propag.*, vol. 45, no. 3, pp. 508–519, March 1997.

[10] A. T. De Hoop, "A modification of Cagniard's method for solving seismic pulse problems", *Appl. Sci. Res., Section B*, vol. 8, no. 1, pp. 349–356, Dec. 1960.

[11] L. Cagniard, *Réflexion et réfraction des ondes séismiques progressives*, Paris: Gauthier-Villars, 1939.

[12] L. Cagniard, *Reflection and Refraction of Progressive Seismic Waves,* (Translation by E. Flinn, C. H. Dix, of Réflexion et réfraction des ondes séismiques Progressives, Paris: Gauthier-Villars, 1939) New York: McGraw-Hill, 1962.

[13] A. T. De Hoop and J. H. M. T. van der Hijden, "Generation of acoustic waves by an impulsive line source in a fluid/solid configuration with a plane boundary," *J. Acoust. Soc. Am.*, vol. 74, no. 1, pp. 333–342, July 1983.

[14] A. T. De Hoop and J. H. M. T. van der Hijden, "Seismic waves generated by an impulsive point source in a solid/fluid configuration with a plane boundary," *Geophysics*, vol. 50, no. 7, pp. 1083–1090, July 1985.

[15] A. T. De Hoop and H. J. Frankena, "Radiation of pulses generated by a vertical electric dipole above a plane, non-conducting, earth," *Appl. Sci. Res., Section B*, vol. 8, no. 1, pp. 369–377, Dec. 1960.

[16] A. T. De Hoop, "Pulsed electromagnetic radiation from a line source in a two-media configuration," *Radio Sci.*, vol. 14, no. 2, pp. 253–268, 1979.

[17] A. T. De Hoop and M. L. Oristaglio, "Application of the modified Cagniard technique to transient electromagnetic diffusion problems," *Geophys. J.*, vol. 94, no. 3, pp. 387–397, Sept. 1988.

[18] M.-Y. Xia, C. H. Chan, Y. Xu, and W. C. Chew, "Time-domain Green's functions for microstrip structures using Cagniard-de Hoop method", *IEEE Trans. Antennas Propag.*, vol. 52, no. 6, pp. 1578–1585, June 2004.

[19] W. C. Chew, *Waves and Fields in Inhomogeneous Media*, New York: IEEE Press, 1995.

[20] A. T. De Hoop, M. Štumpfand I. E. Lager, "Pulsed electromagnetic field radiation from a wide slot antenna with a dielectric layer," *IEEE Trans. Antennas Propag.*, vol. 59, no. 8, pp. 2789–2798, Aug. 2011.

[21] J. H. M. T. van der Hijden, *Propagation of Transient Elastic Waves in Stratified Anisotropic Media*, North-Holland, Amsterdam, 1987.

[22] A. T. De Hoop, "Acoustic radiation from an impulsive point source in a continuously layered fluid – An analysis based on the Cagniard method," *J. Acoust. Soc. Am.*, vol. 88, no. 5, pp. 2376–2388, Nov. 1990.

[23] B. J. Kooij, "The electromagnetic field emitted by a pulsed current point source above the interface of a nonperfectly conducting Earth," *Radio Sci.*, vol. 31, no. 6, pp. 1345–1360, 1996.

[24] R. A. Wiggins and D. V. Helmberger, "Synthetic seismogram computation by expansion in generalized rays," *Geophys. J. R. Astr. Soc.*, vol. 37, no. 1, pp. 73–90, April 1974.

[25] G. G. Drijkoningen and J. T. Fokkema, "The exact seismic response of an ocean and a N-layer configuration," *Geophys. Prosp.*, vol. 35, no. 1, pp. 33–61, Jan. 1987.

[26] Y.-H. Pao and R. R. Gajewski, "The generalized ray theory and transient responses of layered elastic solids," in W. P. Mason and R. N. Thurston (eds.), *Physical Acoustics*, vol. 13, New York: Academic Press, 1977.

[27] A. T. De Hoop, "Acoustic radiation from impulsive sources in a layered fluid," *Nieuw Arch. Wis.*, vol. 6, no. 4, pp. 111–129, June 1988.

[28] A. Sommerfeld, *Partial Differential Equations in Physics*, New York: Academic Press, 1949.

[29] C. A. Schmuttenmaer, "Exploring dynamics in the far-infrared with terahertz spectroscopy," *Chem. Rev.*, vol. 104, no. 4, pp. 1759–1779, April 2004.

[30] A. T. De Hoop, *Handbook of Radiation and Scattering of Waves*, London: Academic Press, 1995, xxx + 1085 pp.; electronic reproduction (with corrections) 2008, freely downloadable, for private use, from http://www.atdehoop.com.

[31] G. Doetsch, *Introduction to the Theory and Application of the Laplace Transformation*, Berlin, Germany: Springer-Verlag, 1974.

[32] M. Štumpf, A. T. De Hoop and G. A. E. Vandenbosch, "Generalized ray theory for time-domain electromagnetic fields in horizontally layered media," *IEEE Trans. Antennas Propag.*, submitted.

[33] D. Kincaid and W. Cheney, *Numerical Analysis: Mathematics of Scientific Computing*, Pacific Grove, CA: Brooks/Cole, 1991.

A hybrid electromagnetics-circuit simulation method exploiting discontinuous Galerkin time domain finite element method

Ping Li and **Li Jun Jiang**
University of Hong Kong, Hong Kong, China e-mail: liping@eee.hku.hk

Abstract

A hybrid electromagnetics (EM)-circuit simulation method employing the discontinuous Galerkin finite element time domain method (DGFETD) is developed to model single lumped port networks comprised of both linear and non-linear elements. The whole computational domain is split into two subsystems. One is the EM subsystem that is analyzed by the DGFETD, while another is the circuit circuit subsystem that is modeled by the Modified Nodal Analysis method (MNA) to generate a circuit subsystem. The coupling between the EM and circuit subsystems is achieved through a lumped port. Due to the local properties of DGFETD operations, only small coupling matrix equation systems are involved. To solve non-linear devices, the standard Newton-Raphson method is applied to solve the established non-linear system equations. Numerical examples are presented to validate the proposed algorithm.

1 Introduction

With the ever increasing operating frequencies of microwave circuits, the minimization of chip packaging, and the requirement of multifunctional capabilities, any successful system/subsystem design must take into account unintentional emissions and couplings from lumped circuit networks. To model non-linear devices, time domain simulators are more favorable compared with frequency domain simulators since transient analysis can directly

---

Pulsed Electromagnetic Fields: Their Potentialities, Computation and Evaluation
I. E. Lager and L. J. Jiang (Eds.).
doi: 10.3233/978-1-61499-230-1-89

consider the non-linear properties without resorting to harmonic balance method.

Recently, many transient simulators are available to analyze the interactions between the full-wave and the circuit regions. Among them, finite-difference time-domain (FDTD) considers lumped elements by a direct stamping technique [1], using an equivalent source concept [2], or an algorithm based on the admittance matrix in Laplace domain [3].

Time domain finite element method (TDFEM) is another popular algorithm. In [4–6], TDFEM combined with the MNA is employed to study the transient behavior of non-linear devices. A global system is constructed by coupling the full-wave parts with circuit subsystems. When non-linear elements are involved, this global matrix system becomes time dependent. A significant amount of time is consumed in factorizing this matrix.

DGFETD [7] is an amenable alternative for FDTD and TDFEM. Compared with FDTD, it supports various types and shapes of elements, unstructured and non-conformal meshes. It also can achieve high order accuracy. Unlike FEM, all the operations of DGFETD are local because of its discontinuous property. In this way, the resultant mass matrix is locally coupled with the dimension equal to the number of degrees of freedom in that element. Hence, the fully explicit time marching scheme with high efficiency is obtained. In [8], DGFETD is applied to study the transient behavior of interconnect structures with linear lumped elements. The lumped elements are treated by assigning each of them onto a rectangular surface. For this kind of direct stamping method, it is quite complex or impossible to model arbitrary complex networks. In [9], the lumped network is solved by a direct recall of SPICE simulator. A lot of time is wasted on the interface communication.

The aim of this letter is to develop a hybrid EM-circuit simulator to model arbitrary complex single port networks including both linear/non-linear elements. The EM part and circuit subsystem couples with each other through an lumped port residing over an rectangular impedance surface. The EM part is analyzed by solving the Maxwell's equation via DGFETD, while the circuit part is modeled by the MNA based on Kirchoff's circuit laws (KCL). The coupling from the EM subsystem to the circuit subsystem is achieved by introducing a voltage source at the lumped port. This voltage source is computed from the integration of the electric field obtained by DGFETD, while the coupling from the circuit subsystem to the EM subsystem is realized by introducing a current source calculated through the circuit solver at the lumped port. Compared with the FEM [4–6], the coupled system (as shown in Section 2.3) is quite small and can be solved with trivial cost. This property is very important for circuit networks including nonlinear elements. To verify our algorithm, numerical results are presented.

2 Formulation

This section details the proposed EM-circuit simulator. The basics of DGFETD is formulated in Section 2.1, and the circuit subsystem is presented in Section 2.2. The details of the coupling scheme between the EM and circuit subsystems are described in Section 2.3.

2.1 Formulation of DGFETD

Suppose that we are concerning the electromagnetic field in the computational domain Ω bounded by $\partial\Omega$. The global domain Ω is splitted into a set of non-overlapping subdomains Ω_i bounded by a surface $\partial\Omega_i$, where $\Omega = \bigcup \Omega_i$. Applying the discontinuous Galerkin testing procedure to the two first-order Maxwell's equations leads to the following two equations,

$$\int_{\Omega_i} \boldsymbol{\Phi}_k^{(i)} \cdot \left(\epsilon \frac{\partial \boldsymbol{E}}{\partial t} - \boldsymbol{\nabla} \times \boldsymbol{H}\right) dV = \int_{\partial\Omega_i} \boldsymbol{\Phi}_k^{(i)} \cdot \left[\hat{\boldsymbol{n}} \times (\boldsymbol{H}^* - \boldsymbol{H}) - \boldsymbol{J}^{\mathrm{im}}\right] \mathrm{d}S \quad (1)$$

$$\int_{\Omega_i} \boldsymbol{\Psi}_l^{(i)} \cdot \left(\mu \frac{\partial \boldsymbol{H}}{\partial t} + \boldsymbol{\nabla} \times \boldsymbol{E}\right) \mathrm{d}V = -\int_{\partial\Omega_i} \boldsymbol{\Psi}_l^{(i)} \cdot \hat{\boldsymbol{n}} \times (\boldsymbol{E}^* - \boldsymbol{E}) \, \mathrm{d}S \quad (2)$$

where $\boldsymbol{\Phi}_k^{(i)}$ denotes the k-th vector basis function for $\boldsymbol{E}$ in the i-th subdomain and $\boldsymbol{\Psi}_l^{(i)}$ denotes the l-th vector basis function for $\boldsymbol{H}$ in i-th subdomain. $\boldsymbol{J}^{\mathrm{im}}$ represents the imposed electrical current density in the EM subsystem. Here, it is assumed to be zero. $\hat{\boldsymbol{n}}$ is the unit outward normal vector. $\hat{\boldsymbol{n}} \times \boldsymbol{H}^*$ and $\hat{\boldsymbol{n}} \times \boldsymbol{E}^*$ are called the numerical flux for communications between adjacent elements. In elements containing lumped ports, the central flux

$$\hat{\boldsymbol{n}} \times \boldsymbol{H}^* = \hat{\boldsymbol{n}} \times \frac{\boldsymbol{H}^- + \boldsymbol{H}^+}{2} - \frac{\boldsymbol{J}^{\mathrm{CKT}}}{2} \quad (3)$$

$$\hat{\boldsymbol{n}} \times \boldsymbol{E}^* = \hat{\boldsymbol{n}} \times \frac{\boldsymbol{E}^- + \boldsymbol{E}^+}{2} \quad (4)$$

is employed, which is derived from the boundary condition over the lumped ports

$$\hat{\boldsymbol{n}} \times (\boldsymbol{H}^+ - \boldsymbol{H}^-) = \boldsymbol{J}^{\mathrm{CKT}} \quad (5)$$

$$\hat{\boldsymbol{n}} \times (\boldsymbol{E}^+ - \boldsymbol{E}^-) = 0 \quad (6)$$

while the upwind flux

$$\hat{\boldsymbol{n}} \times \boldsymbol{E}^* = \hat{\boldsymbol{n}} \times \frac{(Y^-\boldsymbol{E}^- - \hat{\boldsymbol{n}} \times \boldsymbol{H}^-) + (Y^+\boldsymbol{E}^+ + \hat{\boldsymbol{n}} \times \boldsymbol{H}^+)}{Y^- + Y^+} \tag{7}$$

$$\hat{\boldsymbol{n}} \times \boldsymbol{H}^* = \hat{\boldsymbol{n}} \times \frac{(Z^-\boldsymbol{H}^- + \hat{\boldsymbol{n}} \times \boldsymbol{E}^-) + (Z^+\boldsymbol{H}^+ - \hat{\boldsymbol{n}} \times \boldsymbol{E}^+)}{Z^- + Z^+} \tag{8}$$

is used in the elements without lumped ports. The superscripts - and + represent local and neighboring elements, respectively. Z^- is the characteristic wave impedance in the local element and Z^+ is the characteristic wave impedance in the corresponding neighboring element. $Y^- = 1/Z^-$ and $Y^+ = 1/Z^+$ are characteristic wave admittances. $\boldsymbol{J}^{\mathrm{CKT}}$ denotes the current through the lumped port surface.

Next, the fields $\boldsymbol{E}$ and $\boldsymbol{H}$ in the domain Ω_i are expanded by local basis functions: $\boldsymbol{E} = \sum_{k=1}^{n_e^{(i)}} e_k^{(i)} \boldsymbol{\Phi}_k^{(i)}$, $\boldsymbol{H} = \sum_{l=1}^{n_h^{(i)}} h_l^{(i)} \boldsymbol{\Psi}_l^{(i)}$, where $n_e^{(i)}$ and $n_h^{(i)}$ are the number of degrees of freedom for $\boldsymbol{E}$ and $\boldsymbol{H}$ in the i-th domain, respectively. By substituting these two expressions together with (3),(4) into (1),(2), the EM matrix system in the elements where lumped ports reside can be constructed as

$$\boldsymbol{M}_e^{(i)} \frac{\partial \boldsymbol{e}^{(i)}}{\partial t} = \boldsymbol{S}_e^{(i)} \boldsymbol{h}^{(i)} - \frac{\boldsymbol{j}^{(i)}}{2} - \boldsymbol{F}_{eh}^{(ii)} \boldsymbol{h}^{(i)} + \boldsymbol{F}_{eh}^{(ij)} \boldsymbol{h}^{(j)} \tag{9}$$

$$\boldsymbol{M}_h^{(i)} \frac{\partial \boldsymbol{h}^{(i)}}{\partial t} = -\boldsymbol{S}_h^{(i)} \boldsymbol{e}^{(i)} + \boldsymbol{F}_{he}^{(ii)} \boldsymbol{e}^{(i)} - \boldsymbol{F}_{he}^{(ij)} \boldsymbol{e}^{(j)} \tag{10}$$

where

$$\left[\boldsymbol{M}_e^{(i)}\right]_{(kl)} = \int_{\Omega_i} \boldsymbol{\Phi}_k^{(i)} \cdot \epsilon \boldsymbol{\Phi}_l^{(i)} \mathrm{d}V \tag{11}$$

$$\left[\boldsymbol{M}_h^{(i)}\right]_{(kl)} = \int_{\Omega_i} \boldsymbol{\Psi}_k^{(i)} \cdot \mu \boldsymbol{\Psi}_l^{(i)} \mathrm{d}V \tag{12}$$

$$\left[\boldsymbol{S}_e^{(i)}\right]_{(kl)} = \int_{\Omega_i} \boldsymbol{\Phi}_k^{(i)} \cdot \boldsymbol{\nabla} \times \boldsymbol{\Psi}_l^{(i)} \mathrm{d}V \tag{13}$$

$$\left[\boldsymbol{S}_h^{(i)}\right]_{(kl)} = \int_{\Omega_i} \boldsymbol{\Psi}_k^{(i)} \cdot \boldsymbol{\nabla} \times \boldsymbol{\Phi}_l^{(i)} dV \tag{14}$$

$$\left(\boldsymbol{j}^{(i)}\right)_{(k)} = \int_{\partial\Omega_{i,port}} \boldsymbol{\Phi}_k^{(i)} \cdot \boldsymbol{J}^{\mathrm{CKT}} \mathrm{d}S \tag{15}$$

$$\left[\boldsymbol{F}_{eh}^{(ii)}\right]_{(kl)} = \frac{1}{2}\int_{\partial\Omega_i} \boldsymbol{\Phi}_k^{(i)} \cdot \hat{\boldsymbol{n}} \times \boldsymbol{\Psi}_l^{(i)} \mathrm{d}S \tag{16}$$

$$\left[\boldsymbol{F}_{eh}^{(ij)}\right]_{(kl)} = \frac{1}{2}\int_{\partial\Omega_i} \boldsymbol{\Phi}_k^{(i)} \cdot \hat{\boldsymbol{n}} \times \boldsymbol{\Psi}_l^{(j)} \mathrm{d}S \tag{17}$$

$$\left[\boldsymbol{F}_{he}^{(ii)}\right]_{(kl)} = \frac{1}{2}\int_{\partial\Omega_i} \boldsymbol{\Psi}_k^{(i)} \cdot \hat{\boldsymbol{n}} \times \boldsymbol{\Phi}_l^{(i)} \mathrm{d}S \tag{18}$$

$$\left[\boldsymbol{F}_{he}^{(ij)}\right]_{(kl)} = \frac{1}{2}\int_{\partial\Omega_i} \boldsymbol{\Psi}_k^{(i)} \cdot \hat{\boldsymbol{n}} \times \boldsymbol{\Phi}_l^{(j)} \mathrm{d}S \tag{19}$$

where superscript j represents the neighboring element of the i-th element. The $\boldsymbol{\Phi}_k^{(i)}$ and $\boldsymbol{\Psi}_k^{(i)}$ denote the k-th testing basis for the E and H-fields in the i-th element, respectively. The $\boldsymbol{\Phi}_l^{(j)}$ and $\boldsymbol{\Psi}_l^{(j)}$ denote the l-th basis functions for the E and H-fields in the j-th element, respectively.

The first order time derivatives will be approximated using the centering difference method, which is second order accurate. The fully discrete local system equations can be obtained from the semi-discrete system in (9) and (10) with the approximation $\boldsymbol{j}_{n+\frac{1}{2}}^{(i)} = \left(\boldsymbol{j}_{n+1}^{(i)} + \boldsymbol{j}_n^{(i)}\right)/2$ as

$$\begin{aligned}\boldsymbol{M}_e^{(i)}\boldsymbol{e}_{n+1}^{(i)} = \boldsymbol{M}_e^{(i)}\boldsymbol{e}_n^{(i)} + \Delta t \Bigg[\left(\boldsymbol{S}_e^{(i)} - \boldsymbol{F}_{eh}^{(ii)}\right)\boldsymbol{h}_{n+\frac{1}{2}}^{(i)} \\ \left(\boldsymbol{j}_{n+1}^{(i)} + \boldsymbol{j}_n^{(i)}\right)/4 + \boldsymbol{F}_{eh}^{(ii)}\boldsymbol{h}_{n+\frac{1}{2}}^{(j)}\Bigg]\end{aligned} \tag{20}$$

$$\boldsymbol{M}_h^{(i)}\boldsymbol{h}_{n+\frac{3}{2}}^{(i)} = \boldsymbol{M}_h^{(i)}\boldsymbol{h}_{n+\frac{1}{2}}^{(i)} + \Delta t\left[\left(-\boldsymbol{S}_h^{(i)} + \boldsymbol{F}_{he}^{(ii)}\right)\boldsymbol{e}_{n+1}^{(i)} - \boldsymbol{F}_{he}^{(ij)}\boldsymbol{e}_{n+1}^{(j)}\right] \tag{21}$$

2.2 Construction of circuit subsystem equations with MNA

To generate the circuit subsystem equations, the MNA based on KCL is employed to model single port lumped networks with arbitrary number of linear/non-linear elements. The resultant circuit matrix equation at time $t = (n+1)\Delta t$ is

$$\begin{bmatrix}[Y] & -[B] \\ -[B]^{\mathrm{T}} & \mathbf{0}\end{bmatrix}\begin{bmatrix}\boldsymbol{V}_{n+1}^{\mathrm{CKT}} \\ \boldsymbol{I}_{n+1}^{\mathrm{CKT}}\end{bmatrix} + \boldsymbol{I}_{n+1}^{\mathrm{CKT,nl}}\left(\boldsymbol{V}_{n+1}^{\mathrm{CKT}}\right) = \begin{bmatrix}\boldsymbol{I}_n^{\mathrm{CP}} \\ \boldsymbol{V}_{n+1}^{\mathrm{Port}} + \boldsymbol{V}_{n+1}^{\mathrm{ind}}\end{bmatrix} \tag{22}$$

where the $[Y]$ matrix is determined by interconnections between the circuit elements, the $[B]$ matrix is determined by the connection of the supplied voltage sources. $\boldsymbol{V}_{n+1}^{\mathrm{CKT}}$ denotes the unknown non-reference node voltages,

$\boldsymbol{I}_{n+1}^{\mathrm{CKT}}$ denotes the unknown currents through voltage sources. $\boldsymbol{I}_{n+1}^{\mathrm{CKT,nl}}$ represents currents through branches containing non-linear elements. $\boldsymbol{I}_{n}^{\mathrm{CP}}$ is comprised of both the supplied current source and those derived from the companion models of inductors and capacitors, $\boldsymbol{V}_{n+1}^{\mathrm{Port}}$ holds the values of the supplied voltage sources coupled from the EM part, while the $\boldsymbol{V}_{n+1}^{\mathrm{ind}}$ represents the independent voltage source in the circuit subsystem. The overall dimension of the circuit subsystem in (22), denoted as N^{CKT}, is equal to the number of non-reference voltage nodes plus the number of voltage sources.

2.3 Coupling between the EM and circuit subsystems

The coupling between the EM and circuit subsystems is achieved by introducing impressed current and voltage sources at the rectangular lumped ports with width w and length l. Since the lumped port is small compared to the wavelength, quasi-static approximation is assumed at the lumped port. It means that the electric and magnetic fields are constant over the lumped port. At the time $t = n\Delta t$, the supplied voltage at the q-th lumped port associated to i-th element is determined by DGFETD and expressed as

$$\boldsymbol{V}_{n,q}^{\mathrm{Port}} = \sum_{p=1}^{n_e} e_{n,p}^{(i)} \int \boldsymbol{\Phi}_p^{(i)} \cdot \hat{\boldsymbol{l}}_q dl = l \sum_{p=1}^{n_e} e_{n,p}^{(i)} \boldsymbol{\Phi}_p^{(i)} \cdot \hat{\boldsymbol{l}}_q = [C]_q^{(i)} \{e\}_n^{(i)} \tag{23}$$

where $\hat{\boldsymbol{l}}_q$ is the unit vector along the direction of potential descending at the q-th port. Since the current unknowns in the circuit subsystem are $\boldsymbol{I}^{\mathrm{CKT}}$ instead of $\boldsymbol{J}^{\mathrm{CKT}}$, (15) is rewritten for uniform as

$$\left(\boldsymbol{j}^{(i)}\right)_{(n,q,k)} = \frac{\boldsymbol{I}_{n,q}^{\mathrm{CKT}}}{w} \int_{\partial\Omega_{i,port}} \boldsymbol{\Phi}_k^{(i)} \cdot \hat{\boldsymbol{l}}_q \mathrm{d}S = \boldsymbol{I}_{n,q}^{\mathrm{CKT}} \mathrm{G}_{q,k}^{(i)}. \tag{24}$$

The coupled local system equation can be established by combining (20), (23) and (24) and formulated as

$$\boldsymbol{F}(\boldsymbol{x}_{n+1}) = \boldsymbol{b}_n \tag{25}$$

where

$$\boldsymbol{x}_{n+1} = \begin{bmatrix} \boldsymbol{e}_{n+1}^{(i)} & \boldsymbol{V}_{n+1,q}^{\mathrm{CKT}} & \boldsymbol{I}_{n+1,q}^{\mathrm{CKT}} \end{bmatrix}^{\mathrm{T}} \tag{26}$$

$$\boldsymbol{F}(\boldsymbol{x}_{n+1}) = \begin{bmatrix} \left[\boldsymbol{M}_e^{(i)}\right] & \mathbf{0} & \Delta t \mathrm{G}_q^{(i)}/4 \\ \mathbf{0} & [Y]_q & -[B]_q \\ [C]_q^{(i)} & -[B]_q^{\mathrm{T}} & \mathbf{0} \end{bmatrix} \begin{bmatrix} \boldsymbol{e}_{n+1}^{(i)} \\ \boldsymbol{V}_{n+1,q}^{\mathrm{CKT}} \\ \boldsymbol{I}_{n+1,q}^{\mathrm{CKT}} \end{bmatrix} + \begin{bmatrix} \mathbf{0} \\ \boldsymbol{I}_{n+1,q}^{\mathrm{CKT,nl}} \\ -\boldsymbol{V}_{n+1}^{\mathrm{ind}} \end{bmatrix} \tag{27}$$

$$\boldsymbol{b}_n = \begin{bmatrix} \boldsymbol{b}_{\mathrm{EM}} \\ \boldsymbol{I}_{n,q}^{\mathrm{CP}} \\ \mathbf{0} \end{bmatrix} \tag{28}$$

with

$$\boldsymbol{b}_{\mathrm{EM}} = \boldsymbol{M}_e^{(i)} \boldsymbol{e}_n^{(i)} + \Delta t \left[\left(\boldsymbol{S}_e^{(i)} - \boldsymbol{F}_{eh}^{(ii)} \right) \boldsymbol{h}_{n+\frac{1}{2}}^{(i)} - \boldsymbol{I}_{n,q}^{\mathrm{CKT}} \mathrm{G}_q^{(i)}/4 + \boldsymbol{F}_{eh}^{(ii)} \boldsymbol{h}_{n+\frac{1}{2}}^{(j)} \right]. \tag{29}$$

The overall dimension of the coupled system in (25) is equal to $n_e^{(i)} + N^{\mathrm{CKT}}$. Compared with the globally coupled FEM system, this system using DGFETD is very small. Note that the minus sign in front of the $[B]$ matrix is introduced since the current direction in our method is opposite to that defined in the standard MNA formulation. To tackle the instability issue caused by non-linear elements, the standard Newton-Raphson method is used with trivial computational cost due to the coupled small matrix system.

3 Numerical results

In this section, a parallel plate waveguide terminated by different lumped networks is employed to validate the proposed algorithm.

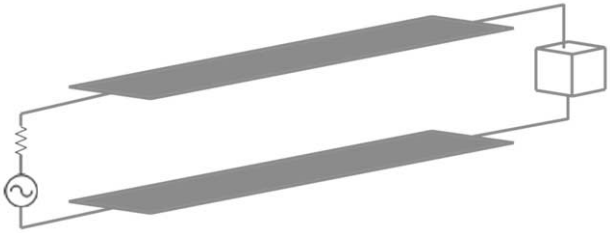

Figure 1: Geometrical structure of a parallel plate waveguide used to verify the proposed algorithm.

In the first example, a 1 cm waveguide is driven by a Thévenin voltage source as shown in Fig. 1 and terminated with a lumped network comprised of only linear lumped elements as shown in Fig. 2 is investigated. Two lumped ports are defined at the driven source and the load end of the waveguide, respectively. The Thévenin voltage source is a first order differential Guassian pulse. The amplitude and phase of the S parameter are presented in Fig. 3 and Fig. 4, respectively. The calculated input impedance is shown in Fig. 5. It can be explicitly noted that very good agreements are achieved from DC to 10 GHz.

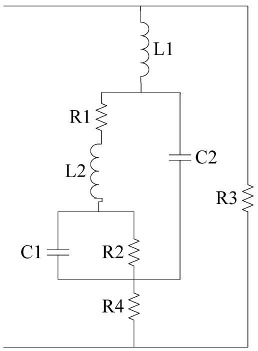

Figure 2: A single port lumped network containing only linear elements. The corresponding R, L, and C values are: $R_1 = 75\,\Omega$, $R_2 = 100\,\Omega$, $R_3 = 376.7\,\Omega$, $R_4 = 100\,\Omega$, $L_1 = 10\,\text{nH}$, $L_2 = 1\,\text{nH}$, $C_1 = 1\,\text{pF}$, $C_2 = 0.01\,\text{pF}$.

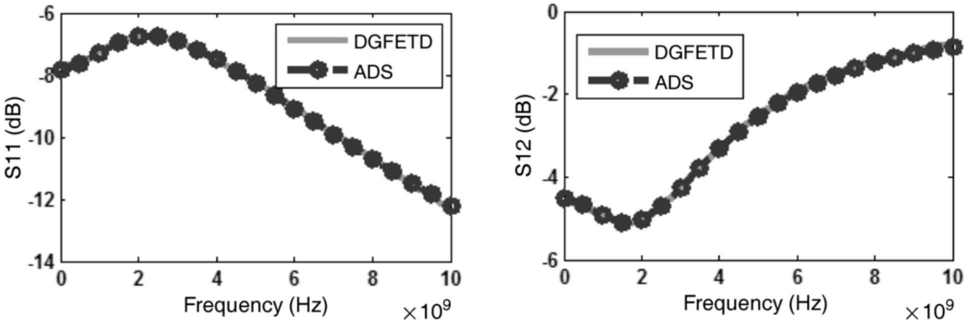

a b

Figure 3: Magnitude of S_{11} and S_{21} calculated from the proposed hybrid EM-circuit simulator and ADS.

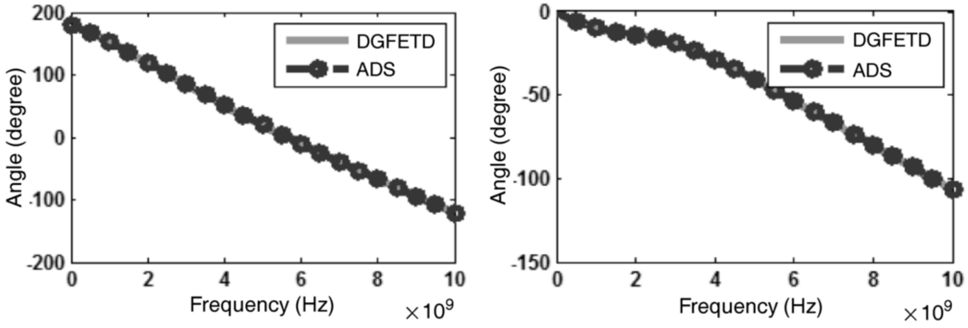

a b

Figure 4: The phase of the S parameter. (a) Phase of S_{11}; (b) phase of S_{21}.

In the next example, the same parallel plate waveguide driven by a TEM wave is studied. It is loaded with silicon diodes ($i_D(t) = I_0[e^{V_D(t)/V_0} - 1], I_0 = 10^{-14}\,\text{A}, V_0 = 0.026\,\text{V}$) as shown in Fig. 5. Since this diode is a

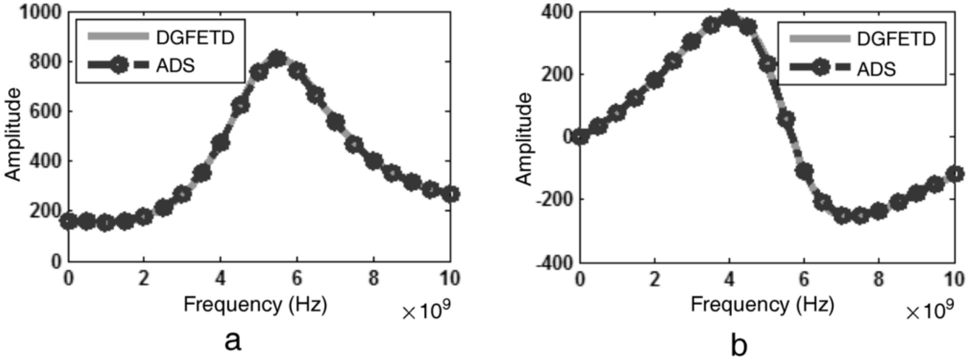

Figure 5: The real part (a) and the imaginary part (b) of the input impedance.

nonlinear device, the standard Newton-Raphson method is applied to handle the potential instability introduced by this non-linearity. The incident wave is a sinusoidal source oscillating at 2.5 GHz. The amplitude of this sinusoidal source is gradually increased, and the time domain voltage at the terminal of the diode in Fig. 6(a) is presented in Fig. 7(a) without any instability problem. It can be clearly noted that the maximum voltage at the diode terminal is around 0.7 V, which complies with the theory.

Finally, the diode pair in Fig. 6(b) is used to terminate the wave guide. This diode pair is capable of limiting the output voltage and is called the clamping diode. Theoretically, the output voltage should be clamped between -0.7 V and 0.7 V. To verify the validity of the proposed algorithm, the output voltage at this diode pair is shown in Fig. 7(b). The calculated result completely agrees with the theory.

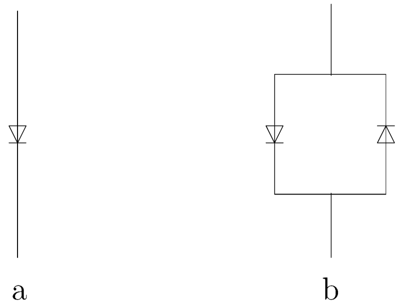

Figure 6: Diode and diode pair are used to validate the capability of the proposed algorithm to handle non-linear elements.

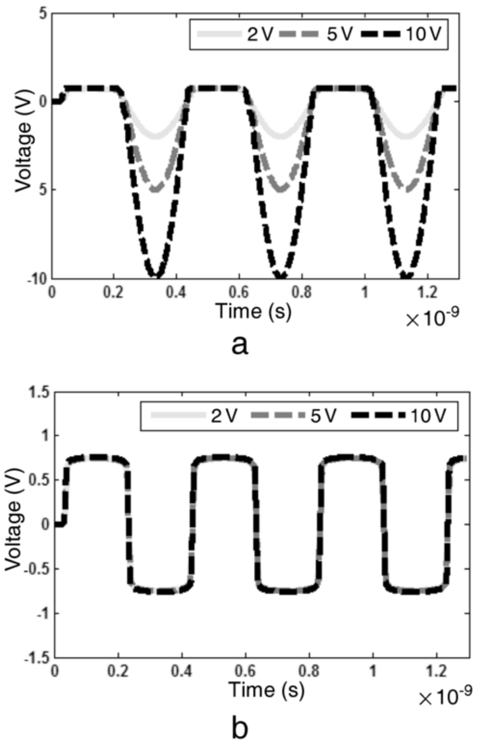

Figure 7: The time domain voltage at the terminal of the diode corresponding to excitations with different amplitude. (a) Output voltage of the diode in Fig. 6(a). (b) Output voltage of the clamping diode in Fig. 6(b).

4 Conclusion

In this work, a hybrid EM-circuit simulator based on the DGFETD and MNA is developed to model single port lumped networks. The interactions between the EM and circuit systems is achieved through a lumped port residing over a rectangular surface. Due to the local property of the DGFETD, the resultant coupled EM-circuit system is quite small. Thus, it can be solved with negligible cost even non-linear elements are included in the lumped network. To suppress the instability issue, the standard Newton-Raphson method is used to solve the non-linear system. The proposed algorithm is validated by numerical examples.

Ongoing work includes the modeling of multi-port lumped networks using DGFETD and MNA. These multi-port lumped networks contain either arbitrarily complex linear or non-linear devices such as power amplifiers, oscillators and so on.

Acknowledgment

The authors are grateful for the constructive suggestions from Professor Weng Cho Chew. We are also grateful to the supports from the Research Grants Council of Hong Kong (GRF 713011 and GRF 712612), National Science Foundation of China (NSFC 61271158), and in part by the University Grants Council of Hong Kong (Contract No. AoE/P-04/08).

Bibliography

[1] M. Piket-May, A. Taflove, and J. Baron, "FD-TD modeling of digital signal propagation in 3-D circuits with passive and active loads," *IEEE Trans. Microw. Theory Tech.*, vol. 42, no. 8, pp. 1514–1523, Aug. 1994.

[2] C. N. Kuo, R. B. Wu, B. Houshmand, and T. Itoh, "Modeling of microwave active devices using the FDTD analysis based on the voltage-source approach," *IEEE Microwave Guided Wave Lett.*, vol. 6, pp. 199–201, Apr. 1996.

[3] C. C. Wang and C. W. Kuo, "An efficient scheme for processing arbitrary lumped multiport devices in the finite-difference time-domain method," *IEEE Trans. Microw. Theory Tech.*, vol. 55, no. 5, pp. 958–965, May 2007.

[4] R. Wang and J. M. Jin, "A symmetric electromagnetic-circuit simulator based on the extended time-domain finite element method," *IEEE Trans. Microw. Theory Tech.*, vol. 56, no. 12, pp. 2875–2884, Dec. 2008.

[5] R. Wang and J. M. Jin, "Incorporation of multiport lumped networks into the hybrid time-domain finite-element analysis," *IEEE Trans. Microw. Theory Tech.*, vol. 57, no. 8, pp. 2030–2037, Aug. 2009.

[6] Q. He and D. Jiao, "Fast electromagnetic-based co-simulation of linear network and nonlinear circuits for the analysis of high-speed integrated circuits," *IEEE Trans. Microw. Theory Tech.*, vol. 58, no. 12, pp. 3677–3687, Dec. 2010.

[7] S. D. Gedney, C. Luo, J. A. Roden, R. D. Crawford, B. Guernsey, J. A. Miller, T. Kramer, and E. W. Lucas, "The discontinuous Galerkin finite-element time-domain method solution of Maxwell's equations," *Journal of Applied Comput. Electromag. Society* , vol. 24, no. 2, pp. 129–142, Apr. 2009.

[8] S. Dosopoulos and J. F. Lee, "Interconnect and lumped elements modeling in interior penalty discontinuous Galerkin time-domain methods," *J. Comput. Phys.*, vol. 229, no. 22, pp. 8521–8536, Nov. 2010.

[9] B. Zhao, J. C. Yong, and S. D. Gedney, "SPICE lumped circuit subcell model for the discontinuous Galerkin finite element time-domain method," in *Proc. IEEE Int. Symp. on Antennas Propag.*, pp. 2969-2971, Spokane, WA, July 2011.

Ensemble methods for large scale inverse problems

Arnold W. Heemink, **M. Umer Altaf**, **Alina L. Barbu** and
Martin Verlaan
Delft University of Technology,
Faculty of Electrical Engineering, Mathematics and Computer Science,
DIAM – Delft Institute of Applied Mathematics,
Mekelweg 4, 2628 CD Delft, the Netherlands,
e-mail: a.w.heemink@tudelft.nl

Abstract

Variational data assimilation, also sometimes simply called the 'adjoint method', is used very often for large scale model calibration problems. Using the available data, the uncertain parameters in the model are identified by minimizing a certain cost function that measures the difference between the model results and the data. A variational scheme requires the implementation of the adjoint of (the tangent linear approximation of) the original model which is a tremendous programming effort, that hampers new applications of the method. Recently a new ensemble approach to variational inverse modelling using Proper Orthogonal Decomposition (POD) model reduction has been proposed that does not require the implementation of the adjoint model. Using an ensemble of forward model simulations an approximation of the covariance matrix of the model variability is determined. A limited number of leading eigenvectors of this matrix are selected to define a model sub space. By projecting the original model onto this subspace an approximate linear model is obtained. Once this reduced model is available the minimization process can be solved completely in reduced space with negligible computational costs.

Schemes based on the well-known Kalman filtering algorithm are also used recently for inverse modeling. The last years a number of ensemble based algorithms have been proposed, e.g., the Ensemble Kalman filter (EnKF), the Reduced Rank Square Root filter (RRSQRT) and the Ensemble Square Root filter (ESRF). Although introduced for linear state estimation, these new algorithms

---

Pulsed Electromagnetic Fields: Their Potentialities, Computation and Evaluation
I. E. Lager and L. J. Jiang (Eds.).
doi: 10.3233/978-1-61499-230-1-101

are able to handle nonlinear models accurately and, therefore, are very attractive for solving combined state and parameter estimation problems. It has been shown recently that the so-called symmetric version of the ESRF introduces the smallest increments and, therefore, is in most applications more accurate then the original version of this algorithm.

1 Introduction

Computational models for pulsed EM fields usually contain a number of uncertain parameters that have to be identified using measurements. In this way a more accurate reconstruction of the dynamic behavior of the model state can be obtained. Variational data assimilation schemes (see [1]) have often been used for model calibration, e.g., [2]. These methods aim at adjusting a number of unknown parameters on the basis of some given observations. One first defines an objective function, which, for any model solution over the assimilation interval, measures the misfit between that solution and the available observations. Then, the new model solution is obtained by minimizing this objective function. To obtain a computationally efficient procedure, this objective function is minimized with a gradient-based algorithm that determines the gradient of the given problem. Usually, it requires the implementation of an adjoint model, which requires a huge programming effort even with the use of an adjoint compiler.

Proper orthogonal decomposition (POD) is a model reduction method considered as an application of the SVD to the approximation of general dynamical systems [3]. The method was originally developed by [4] and has been extensively used and successfully applied in many fields like image processing, signal processing, data compression, oceanography, chemical engineering and fluid mechanics [5–7]. The POD has recently been applied successfully in variational data assimilation [8, 9]. In the presented reduced order approach a set of snapshot vectors of forward model simulations is used to determine an approximation of covariance matrix and a small number of eigenvectors of this matrix are used to define a model subspace. By projecting the original model onto this subspace, an approximate linear model is obtained. The controllable subspace obtained is low rank and hence an efficient reduced model is obtained. Once the reduced model is available, its adjoint can be implemented easily and the minimizing problem is solved completely in reduced space with very low computational cost [10].

Kalman filtering is a well known method for state estimation. The standard Kalman filter algorithms however would impose an unacceptable computational burden for systems with a very large state dimension. In order to obtain a computationally efficient filter new algorithms have been introduced. The last years a number of ensemble based algorithms have been proposed, e.g. the Ensemble Kalman filter (EnKF), the Reduced Rank Square Root filter (RRSQRT) and the Ensemble Square Root filter (ESRF). Ott et al. [11] and Sakov et al. [12] showed that the symmetric version of the Ensemble Square Root Filter has the property that the analysis increments are smallest. Recently [13] also introduced the symmetric version of the RRSQRT algorithm and shown that in many different experiments the symmetric versions of both the ESRF as the RRSQRT filter are the most accurate algorithms. The ESRF algorithms are able to handle nonlinearities very well. As a result they can also be used for parameter estimation by simply adding the uncertain parameters to the state vector. Ensemble type algorithms can be implemented very easily also in case of complex large scale systems. Furthermore it is also possible to take into account statistical errors in the underlying model. Because of these advantages ensemble Kalman filters have become a very attractive inverse modeling technique.

In this paper we will discuss ensemble approaches to inverse modeling. Here we focus on inverse modeling problems with a very large number of uncertain parameters. All the algorithms we describe are “adjoint-free” methods and are very easy to implement in combination with complex large scale numerical modeling systems. In Sections 2, 3 and 4 we briefly explain the procedure required for the construction of different projection based reduced methods, the classical inverse modeling methods, define the procedure for collecting snapshots and the basis vectors (patterns) required for simulation of reduced model in the context of variational data assimilation. To illustrate the procedure in the Section 5 numerical results obtained by applying the procedure to the 2D-advection diffusion model to estimate a space varying diffusion are presented. In Section 6 we briefly summarize the ensemble Kalman filter approach to inverse modeling and illustrate this approach with a similar 2D-advection diffusion model.

2 Reduced order modeling

Given a dynamical system defined by

$$x(t_i) = A_i x(t_i) + B\,u(t_i), \quad y(t_i) = H\,x(t_i) \tag{1}$$

where $A \in \mathfrak{R}^{n\times n}$, $B \in \mathfrak{R}^{n\times k}$, $H \in \mathfrak{R}^{q\times n}$, the aim of reduced order modeling is to find a projection $\Pi = V\,U^{\mathrm{T}}$ with $U^{\mathrm{T}}V = I_r$ where $r < n$, to obtain the reduced order dynamical system as follows

$$\hat{x}(t_i) = U^{\mathrm{T}} A_i V \hat{x}(t_i) + U^{\mathrm{T}} B u(t_i), \quad y(t_i) = HV(\hat{x}(t_i)) \tag{2}$$

whose trajectories $\hat{x} = U^{\mathrm{T}}x$, evolve in an $r-$dimensional subspace. If $V = U$, we have Galerkin (orthogonal) projection and oblique (Petrov-Galerkin) projection otherwise.

2.1 Proper Orthogonal Decomposition

The POD consists in the orthogonal decomposition of the correlation associated with the state variable of the system and its representation, optimal in the least square sense, with respect to the orthonormal, complete set of the eigenfunctions of the correlation operator. The POD is an optimal technique of finding a basis, which spans an ensemble of data, collected from an experiment or a numerical simulation of a dynamical system, in the sense that when these basis functions are used in a Galerkin procedure.

We start by collecting a set of s snapshots of some physical process taken at position $\boldsymbol{x}$

$$x_i = \{x_{i1}, x_{i2}, \ldots, (x_{in}), i = 1, 2, \ldots, s\}. \tag{3}$$

Define the vector $\boldsymbol{x}_b$ of background state and correct each snapshot vector so that

$$e_i = x_i - x_b. \tag{4}$$

These corrected snapshots are arranged in matrix E which denotes the new ensemble. We define an eigenvalue decomposition problem of discrete covariance matrix $Q = E\,E^{\mathrm{T}}$ as:

$$Qp_j = \lambda_j p_j, \quad j = 1, 2, \ldots, n. \tag{5}$$

The dimension n can be of the order of 10^8, and even larger, so direct eigenvalue decomposition of Q is not feasible. One can however solve the reduced $s \times s$ eigenvalue problem

$$E^{\mathrm{T}}E\psi_k = \lambda_k \psi_k, \quad k = 1, 2, \ldots, s \tag{6}$$

where the eigenvalues λ_j are the same as in (5). We can choose the eigenvectors ψ_k orthonormal and give POD modes (patterns) by

$$p_k = E\psi_k / \lambda_k. \tag{7}$$

The number of patterns should be chosen in such a way that they are close to capture 100% relative energy.

2.2 Balanced POD

Balanced POD is an approximation to balanced truncation. The idea has recently applied by [14]. The main idea behind balanced truncation is to consider both inputs and outputs of the system (1), i.e., considering both controlability and observability, while determining which states to keep in the reduced model structure. A controllable subspace is the space that can be obtained with zero initial state and a given input $u(t)$. It is similar to the POD dataset of snapshots given in Section 2.1 obtained by simulation of original model.

$$W_c = EE^{\mathrm{T}}. \tag{8}$$

The extra computation in this method is the computation of observability gramian (W_o). With no external input, the observable subspace consists of those states which produces nonzero output $y(t)$. For this we compute the impulse responses of the adjoint system based on original system (1).

$$\dot{z}(t_i) = Az(t_i) + Hu_z \tag{9}$$

So we need to solve the adjoint system as many time as the number of outputs. If the number of outputs is large then its computationally expensive, so we follow the following procedure:

a) *Project the snapshots $E = \{\boldsymbol{e}_1, \boldsymbol{e}_2, \ldots, \boldsymbol{e}_s\}$ on observation the space.*

b) *Obtain r dominant POD modes of this projection.*

c) *Instead of solving the adjoint system for q outputs we need to solve it for r dominant modes to get a similar matrix F as in case of POD data set*

$$W_o = F\,F^{\mathrm{T}} \tag{10}$$

Balanced POD modes are the dominant eigenvectors of the product of two gramians, which are obtained by singular value decomposition (SVD) of the matrix (F^*S).

The use of balanced POD for parameter estimation requires the adjoint of the tangent linear approximation of the forward model operator, but does not require the Jacobian with respect to the parameters (as in the case the full adjoint method). Sometimes the Jacobian with respect to states is available as part of the numerical scheme of the original forward model.

3 Inverse modeling

The idea of parameter estimation is the estimation of uncertain model parameters by minimizing the measure of residuals. Let γ_k be the estimate variable to be determined, then we can define a nonlinear discrete model for the state vector $\boldsymbol{x}$ as

$$X(t_i) = M_i\left[X(t_{i-1}), \gamma_k\right], \quad Y_i = H\left[X(t_i)\right] + v(t_i) \tag{11}$$

where M_i is a nonlinear and deterministic dynamics operator that includes inputs and propagates the state from time t_{i-1} to t_i. Here H is an operator that maps the model fields on observation space. $v(t_i)$ is a white Gaussian observation noise process with zero mean and covariance matrix R_i. The objective function J to be optimized is defined based on model-data misfit as

$$J(\gamma_k) = \sum_{i=1}^{s} \left\{Y(t_i) - H[X(t_i)\right\}^{\mathrm{T}} R_i^{-1} \left\{Y(t_i) - H[X(t_i)]\right\} \tag{12}$$

The minimization of the objective (cost) function is often based on quasi-Newton method. These methods require the computation of the gradient ($\boldsymbol{\nabla} J$) of the cost function. In most situations it is possible to numerically determine the gradient through adjoint method efficiently. The principle of adjoint model is based on systematic use of chain rule of differentiation. It needs one forward simulation and a second additional simulation backward in time with the adjoint model. If $\lambda(t_i)$ is the solution of the adjoint model, then the gradient $\boldsymbol{\nabla} J$ of the cost function with respect to estimate variable γ_k is

$$\boldsymbol{\nabla} J = \sum_i -\lambda(t_i)^{\mathrm{T}} \frac{\partial M\left[X\left(t_{i-1}\right)\right]}{\partial \gamma_k}. \tag{13}$$

The main hurdle in the use of adjoint method is its implementation, as it requires huge programming effort. Also the adjoint equation need to be integrated backward in time, the determined states of the original problem must be stored for all time steps. The memory access will therefore be huge for largescale problems, and is therefore major hurdle in applying the adjoint model to compute the gradient of J.

4 Inverse modeling using a reduced model

An approximate linear reduced model inspired by the work of [10] in variational data assimilation is based on the principle of POD model reduction technique. A set of snapshot vectors is generated from the original model.

Reduced model operates on the dominant eigenvectors generated from the set of snapshots. The reduced model used here includes dependency on estimated parameters γ_k. The snapshot vectors of the original model provide sensitivity with respect to γ_k. A single snapshot vector is obtained by perturbing γ_k as

$$e_k(t_i) = \frac{\partial M_i \left[X^b\left(t_{i-1}\right), \gamma_k\right]}{\partial \gamma_k} \tag{14}$$

where X^b is the background state for which the corresponding estimate variable γ_k is linearized. The number of snapshot vectors depends on the number of time-steps and number of estimate variables. We follow the procedure given in Sections 2.1 or 2.2 to calculate the basis of the leading eigenvectors. The total number of vectors in basis depends on the accuracy required for the reduced model. If $\hat{X}$ is the approximate linearized state, then we can write

$$\hat{X}(t_i) = X^b(t_i) + V\xi(t_i) \tag{15}$$

with $\xi(t_i)$ being the reduced state vector

$$\xi\left(\Delta\gamma_k\right) = N_i\left[\hat{X}\left(t_{i-1}\right), \Delta\gamma_k\right] + N_\gamma \Delta\gamma_k. \tag{16}$$

The dimension on which reduced model operates is $(r+u)$, where r is the number of basis vectors. N and N_γ are reduced dynamics operators computed as

$$N_i = U^{\mathrm{T}} \frac{\partial M_i}{\partial X^b\left(t_{i-1}\right)} V \tag{17}$$

$$N_\gamma = U^{\mathrm{T}} \left(\frac{\partial M_i}{\partial \gamma_1}, \ldots, \frac{\partial M_i}{\partial \gamma_u}\right) \tag{18}$$

The value of the approximate objective function $\hat{J}$ is obtained by correcting the observations $Y(t_i)$ for background state $X^b(t_i)$ which is mapped on the observational space through a mapping H and for the reduced model state $\xi(t_i, \Delta\gamma)$ which is mapped to the observational space through mapping $\hat{H}$ with $\hat{H} = HP$.

$$\hat{J}\left(\Delta\gamma_k\right) = \sum_i \left\{Y(t_i) - H\left[X^b(t_i)\right] - \hat{H}\xi\left(t_i, \Delta\gamma\right)\right\}^2 \tag{19}$$

Let $\hat{\lambda}(t_i)$ be a reduced adjoint state, then the gradient of the approximate objective function 19 is given by

$$\frac{\Delta\hat{J}}{\Delta\gamma_k} = \sum_i -\hat{\lambda}(t_i)^{\mathrm{T}} \frac{\partial \xi(t_i)}{\partial \Delta\gamma_k}. \tag{20}$$

Once the gradient is obtained, the reduced model is used again to compute the $\hat{J}$ along the direction of the gradient. As reduced model and its adjoint model both are low dimensional and have linear characteristics the amount of simulation time is negligible. In Fig. 1 a flowchart of the inverse modelling process is given.

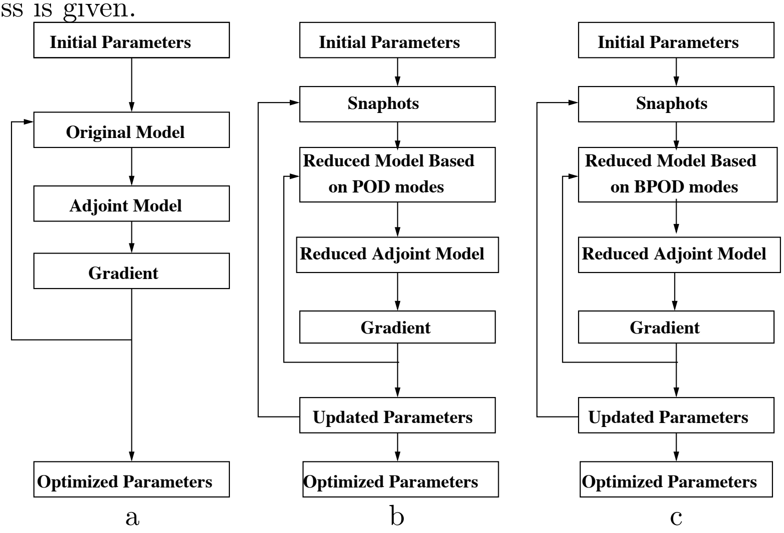

Figure 1: Flow chart of inverse modeling process by (a) classical method; (b) POD reduced method; (c) BPOD outer projection method.

5 Numerical experiment

5.1 The model

We consider the advection-diffusion of concentration $c(x, y, t)$ for the transport of pollutant in two space dimensions. The evaluation of c with square domain $[0, 20] \times [0, 20]$ gives

$$\frac{\partial c}{\partial t} + u\frac{\partial c}{\partial x} + v\frac{\partial c}{\partial y} = \frac{\partial}{\partial x}\vartheta\frac{\partial c}{\partial x} + \frac{\partial}{\partial x}\vartheta\frac{\partial c}{\partial x} + S \tag{21}$$

where ϑ contains diffusion coefficient, $[u, v]$ is the velocity field which is given and constant with respect to time and S is the source term. A solution to the partial differential equation is obtained by imposing boundary conditions and applying Euler-time stepping to approximate the time derivative, the second derivatives are approximated with the central finite difference, while the upwind scheme is used for the first order spatial derivatives. Initially the concentration is zero for the whole model domain.

We have applied the reduced model approach describe above to the 2D advection diffusion model 21 to estimate the diffusion coefficient. The experiments are performed for three different cases, two with POD based reduced-order method and the last case compares the BPOD method with POD method. The original model is simulated for 50 time-steps. The estimate variable γ_k is effected by the parameter ϑ. A uniform source term is introduced at two grid points during the course of simulation.

5.2 Case 1

Here we have considered diffusion to be more dominant than advection. The number of parameters estimated for this case is two. A set of observations is obtained at 2 different grid points in the model domain. The estimate parameters γ_1 and γ_2 effect two different zones within model domain. The true value for both parameters is $\gamma^t = 0.18$. Initially, $\gamma_1 = 0.12$ and $\gamma_2 = 0.2$. For these initial parameters, a set of snapshot vectors is generated and we are able to form a basis consisting of only 8 vectors that captured 99.99% relative energy. So a reduced model is built using these basis vectors. With this reduced model, approximate objective function $\hat{J}$ is minimized and new values of estimate variables are found at $\gamma_1 = 0.1641$ and $\gamma_2 = 0.1944$. This process is repeated several times by running the original model using the new set of updated parameter values.Table 1 shows the results of minimization of two estimate variables.

Table 1: The results for minimization of two estimate variables (Case 1).

β	γ_1	γ_2	J	$\hat{J}$	$\Re^n$
initial	0.12	0.20	0.8434	0.0504	10
1	0.1641	0.1944	0.0865	0.0172	10
2	0.1751	0.1899	0.0167	0.0056	10
3	0.1830	0.1783	0.0035	4.5×10^{-4}	10
6	0.17998	0.17969	1.08×10^{-5}	4.77×10^{-6}	10

5.3 Case 2

Here, we have applied the BPOD outer projection procedure to get the basis of reduced model and compare results with POD and BPOD based reduced-order models. The whole model domain is divided into two parameter zones. A set of observations is obtained at every other grid point, i.e., 200. The initial values of the parameters are same as in previous case. Snapshots are collected by running the original model and applying BPOD (outer projection method) explained in Section 2.2, to obtain basis U and V. To quantify the performance of both reduced models we have used as metric the root mean square error. This is obtained by first taking the full order approximation results and the corresponding reduced order results of the forward run within the inner loop of variational data assimilation. Table 2 shows the error in full and reduced order approximations (POD, BPOD and BPOD with outer projection). It can be seen from table that error in BPOD is less than that of POD reduced model. Outer projection method with only 12 balancing modes gives the same result as compared to full BPOD with 200 observations.

Table 2: Error in full and reduced order approximations.

No. of modes	**5**	**6**	**7**	**8**	**9**	**10**
POD	0.315	0.169	0.167	0.095	0.091	0.063
BPOD	0.237	0.141	0.135	0.088	0.086	0.062
BPOD (12 OP)	0.238	0.141	0.135	0.087	0.086	0.063

6 Ensemble Kalman filter

Let us now assume that modeling techniques have provided us with a nonlinear stochastic state space representation of the form

$$X_{i+1} = M_i\left[X(t_i)\right] + B_i u(t_i) + G_i w(t_i) \tag{22}$$

where X_i is the system state, u_i is the input of the system, M_i is a nonlinear function, and B_i is an input matrix. A white Gaussian system noise process W_i with zero mean and covariance matrix $Q(i)$ is introduced to take into account the model uncertainties. $G(i)$ is the noise input matrix. The initial state X_0 is assumed to be Gaussian with mean X_0 and covariance matrix P_0. The initial condition, the system and measurement noise processes are all assumed to be independent of each other. It can be shown that the model (22) is Markov.

The standard Ensemble Kalman Filter (EnKF) introduced by [15] is a Monte Carlo approach to the Kalman Filter. It is based on the representation of the probability density of the state estimate by a finite number of randomly generated system states and is able to handle the nonlinearities of the models. In the first version of the EnKF, all ensemble members were updated with the same observations and as consequence, the analyzed covariance matrix was systematically underestimated. Therefore, now an independent set of perturbed observations obtained by adding random noise to the actual measurements is used in the analysis step to prevent the collapse of the ensemble [16].

The Ensemble Kalman filter is based on a finite number N randomly generated system states

$$\xi_i(i-1|i-1), \quad i = 1, \ldots, N. \tag{23}$$

The optimal estimate and the square root of the covariance matrix of the estimation error are now given by

$$X(i-1|i-1) = \frac{1}{N}\sum_{i=1}^{N} \xi_i(i-1|i-1) \tag{24}$$

$$\begin{aligned} L(i-1|i-1) = \frac{1}{\sqrt{N-1}} \Big[&\xi_1(i-1|i-1) - X(i-1|i-1) \ldots \\ &\xi_N(i-1|i-1) - X(i-1|i-1) \Big]^{\mathrm{T}} \end{aligned} \tag{25}$$

The square root $L(i-1|i-1)$ defines an approximation of the covariance matrix $P(i-1|i-1)$ with rank N

$$P(i-1|i-1) = \frac{1}{N-1} L(i-1|i-1) L(i-1|i-1)^{\mathrm{T}}. \tag{26}$$

$P(i-1|i-1)$ is however never actually computed. Using the algorithm first the initial ensemble of state vectors is generated with mean x_0 and covariance matrix P_0. Then for updating the ensemble, realizations of the system noise and measurement noise processes are generated too. The Ensemble Kalman filter algorithm can be summarized as follows:

Time update:

$$\xi_i(i|i-1) = f\left[\xi_i(i-1|i-1), i-1\right] + G(i) w_i^i \tag{27}$$

$$X(i|i-1) = \frac{1}{N}\sum_{i=1}^{N} \xi_i(i|i-1) \tag{28}$$

$$L(i|i-1) = \frac{1}{\sqrt{N-1}}\Big[\xi_1(i|i-1) - X(i|i-1)\dots \\ \xi_N(i|i-1) - X(i|i-1)\Big]^{\mathrm{T}} \tag{29}$$

Measurement update:

$$K_i = L(i|i-1)L(i|i-1)^{\mathrm{T}}H_i^{\mathrm{T}}\Big[H_iL(i|i-1)L(i|i-1)^{\mathrm{T}}H_i^{\mathrm{T}} + R_i\Big]^{-1} \tag{30}$$

$$\xi_i(i|i) = \xi_i(i|i-1) + K_i\Big[Y_i - H_i\gamma_i(i|i-1) + v_i^i\Big] \tag{31}$$

The time update equation is for most applications computationally dominant. As a result the computationally effort required for the Ensemble Kalman filter is approximately N model simulations. The ensemble Kalman filter does not suffer from the curse of dimensionality. Even for very large state dimensions 50–200 ensemble members are often enough to obtain reliable results. However the standard deviation of the statistical errors in the state estimate converges very slowly with the sample size. This is one of the very few drawbacks of this Monte Carlo type approach. Note that for the time update only simulations with the original nonlinear model are used. The tangent linear model is not required.

An alternative way to solve the update step of the ensemble-based filter is represented by the deterministic analysis that is not sensitive to the observational sampling errors associated with the use of perturbed observations. This method referred to as ensemble square root filter (ESRF) is placed in a unified framework by [17, 18].

It is possible to classify the ESRF into three subclasses as the cycle of alternating forecast and analysis steps are performed: stochastic ESRF, where both steps are influenced by sampling for each ensemble member using a pseudo-random generator, semi-deterministic ESRF, where only the forecast step is based on sampling, and deterministic ESRF, where both steps of the assimilation cycle are deterministic. The first two classes contain the ensemble-based filters. An example of a deterministic ESRF is given by the Reduced Rank Square Root (RRSQRT) filter introduced by [19].

Using the following notations

$$Y = HL(i|i) \tag{32}$$

$$S = YY^{\mathrm{T}} + R \tag{33}$$

the updated covariance matrix becomes

$$L(i|i)L(i|i)^{\mathrm{T}} = L(i|i-1)\left(I - Y^{\mathrm{T}}S^{-1}Y\right)L(i|i-1)^{\mathrm{T}}. \tag{34}$$

The solution of equation (34) is obtained as

$$L(i|i)L(i|i-1)T \tag{35}$$

where T is a matrix that satisfies

$$TT^{\mathrm{T}} = I - Y^{\mathrm{T}}S^{-1}Y. \tag{36}$$

It can easily be shown that there is a unique symmetric positive definite solution to equation (36) defined as the square root of the symmetric positive definite matrix in the brackets.

$$T^{\mathrm{s}} = \left[I - Y^{\mathrm{T}}S^{-1}Y\right]^{1/2}. \tag{37}$$

By using the eigenvalue decomposition, the matrix T^{s} has the following form

$$T^{\mathrm{s}} = C\Lambda^{1/2}C^{\mathrm{T}}. \tag{38}$$

Following Ott et al. [11] and Sakov et al. [12], we will refer to T^{s} as the symmetric solution. The symmetric algorithm defined above introduces the smallest analysis increments for an arbitrary compatible norm. This property is one of the main reasons of the good performance of the symmetric ESRF obtained by [11, 12].

With a formal definition, an ESRF is an ensemble filter in which the analysis ensemble is updated by using an ensemble transform matrix (ETM) T which satisfies Eq. (36). Consequently, every semi-deterministic filter belongs to the class of the ESRF. In addition, the set of all solutions T which characterize the ESRF class is described in terms of the orthogonal matrix group $O(N)$. Then, a general form of T that satisfies Eq. (36) is

$$T = T^{\mathrm{s}}U \tag{39}$$

where T^{s} is the symmetric solution and U is an arbitrary orthonormal matrix. The ESRF method encompasses filters with a ETM which matches the exact analyzed covariance, but the update perturbations could change the ensemble mean. An example is provided by the Ensemble Transform Kalman Filter (ETKF) introduced by [20] whose ETM denoted by T^{o} is obtained by the multiplication of (38) by the orthogonal matrix C

$$T^{o} = T^{\mathrm{s}}C = C\Lambda^{1/2} \tag{40}$$

We will refer to the solution (40) as the one-sided formulation of the ESRF. A random rotation U^{r} was added to the solution of Eq. (40) to prevent the ETKF tendency of producing high variance outliers [21]

$$T = T^{\mathrm{s}}U^{\mathrm{r}} \tag{41}$$

It has been found by [18, 22] that the statistics of the update ensemble were still inconsistent with the actual error. A valid analysis ensemble should satisfy the zero-centered condition

$$L(i|i)\mathbf{1} \tag{42}$$

where $\mathbf{1}$ is the vector with all elements being 1. Due to the fact that the forecasted ensemble perturbations do not perturb the ensemble mean, a sufficient condition for an analyzed ensemble to preserve the ensemble mean is that the ensemble transform matrix T satisfies (up to a scalar constant λ) the following mean-preserving condition

$$T\mathbf{1} = \lambda\mathbf{1}. \tag{43}$$

We will refer to an ESRF with the ETM satisfying Eq. (43) as an unbiased ensemble square root filter (UESRF). Sakov et al. [12] and Wang et al. [23] have shown that the symmetric transformation does not introduce a bias. Therefore, for providing a mean-preserving solution, it is sufficient to find a rotation matrix U^{p} such that the vector $\mathbf{1}$ is an eigenvector of U^{p}. To obtain an arbitrary orthogonal transformation with the desired propriety, we need to construct an orthonormal basis B whose first orthonormal vector is $\mathbf{1}/N^{1/2}$ by using the Gram-Schmidt procedure. Consequently, the required rotation matrix has the following form

$$U^{\mathrm{p}} = B \begin{pmatrix} 1 & 0 \\ 0 & U_1 \end{pmatrix} B^{\mathrm{T}} \tag{44}$$

where U_1 is a random orthonormal matrix obtained from the singular value decomposition of a generated pseudo-random matrix. The ESRF with the matrix transformation T^{s} is unbiased and, if the vector $\mathbf{1}$ is an eigenvector of a rotation matrix U^{p}, the new transformation matrix written as

$$T = T^{\mathrm{s}}U^{\mathrm{p}} \tag{45}$$

is a mean-preserving solution. The ETM from (45) defines an UESRF algorithm.

Much of the research for square root filtering has been devoted to the analysis step. For strongly unstable dynamics this can be motivated, but for many applications also the system noise plays an important role. In the ESRFs the system noise is added with the introduction of random numbers, but as in the analysis, this scheme introduces sampling errors. To avoid the sampling errors, several approaches have been proposed, e.g., the reduced-rank square root (RRSQRT) filter by [19] or its extensions [24]. The RRSQRT algorithm belongs to the deterministic (both forecast and analysis are deterministic) methods. It is an ensemble version of the famous extended Kalman filter. It is very efficient for weakly nonlinear problems. However, for strongly nonlinear estimation problem like we generally have in parameter estimation problems, the ESRF seems to be the best choice.

The numerical experiments in this section are intended to show the performance of the four semi-deterministic filters obtained by using different solutions of the Eq. (36). Our data assimilation experiments use a 2D pollution model [24], based on the 2D advection diffusion equation for the transport of a pollutant (see Eq. (21)).

A reference simulation was performed by inserting randomly generated emissions at five grid cells (see Fig. 2). Observations are measured in twelve locations of the domain (see Fig. 2) and they are simulated using the true concentrations to which a zero mean Gaussian observation noise was added with standard deviation 0.1. In the assimilation experiment the initial emission is assumed to be zero resulting in a zero concentration field. Using the data the emission parameters are reconstructed and the concentration can be estimated.

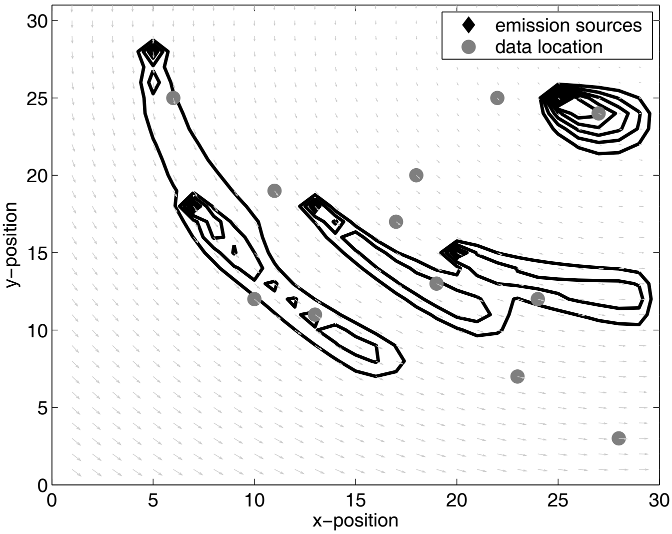

Figure 2: Reference simulation of concentrations and wind velocity. Emission sources and data locations are represented by diamonds.

In Fig. 3 the root mean square error of the filter results are shown for the various algorithms. Here the error is determined at a certain time by comparing the filter result with the exact result over the entire spatial domain. From the results it is clear that the symmetric versions of the algorithms are the most accurate. For more results the reader is referred to [13].

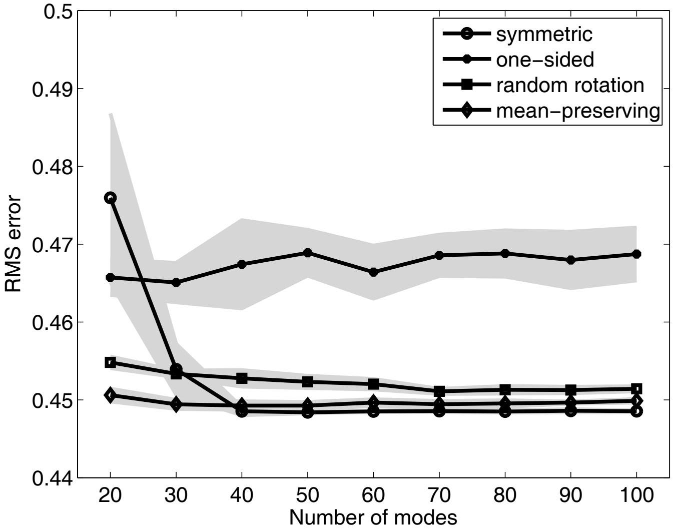

Figure 3: Average root mean square error of the concentration over 500 time steps and 10 realizations as function of ensembles and modes, for the ESRFs filters using an observational standard deviation error of 1.0. The standard deviation between the independent simulations is represented by the grey bands.

Although originally developed for state estimation Ensemble Kalman filter is also used for large scale combined state and parameter estimation problems. The symmetric version of the ESRFs which has the smallest analysis increments over all semi-deterministic filters provides the more accurate solution compared to one-sided variant, random rotations and mean-preserving random rotations. What seems consistent is that the symmetric ESRF is always among the best performing algorithms of the 4 ESRFs in tests performed by [13]. From these experiments and those reported by other authors and because of the attractive theoretical properties, we conclude that the symmetric ESRF is likely to provide the most accurate results for a large number of applications when compared to other ESRFs. In addition, the computational requirements are not significantly larger for the symmetric ESRF, nor is it difficult to implement.

In reservoir engineering the Ensemble Kalman filter is used very often for estimation the permeability field in large scale reservoir models [25]. Filter divergence might be a problem in case of a large amount of data. This can be reduced however using localization techniques. For more details the reader is referred to the review paper [25].

7 Conclusions

In variational data assimilation, it is necessary to build an adjoint model for the efficient computation of the gradient. This adjoint model is difficult to implement for large-scale systems. In this work we have developed a method of simplifying this problem using a projection based POD model reduction method. The method approximates the full dynamical system while retaining its essential properties. Numerical experiments have been performed with this method to estimate the diffusion coefficient in a 2D advection-diffusion model.

Balancing is also applied using the outer projection method, to obtain an approximate balanced truncation, so that the basis vector matrices also capture information of the observable subspace. Results show that computationally efficient balanced reduced model can be obtained using outer projection. Balancing does however require the Jacobian with respect to the state (not with respect to the parameters).

The Ensemble Kalman filter is very suitable for nonlinear systems and can easily be used for combined state and parameter estimation. This approach is very easy to implement and it is also possible to include a statistical model error. The symmetric version of the ensemble square root filter has the smallest analysis increments over all semi-deterministic filters. From this theoretical result and from experiments reported in literature, we conclude that the symmetric ESRF is likely to provide the most accurate results for a large number of combined state and parameter estimation problems.

Bibliography

[1] G. Chavent, M. Dupuy, and P. Lemonnier, “History matching using optimal control theory,” *SPE journal*, vol. 15, pp. 74–86, 1975.

[2] J. Carrera and S. P. Neuman, “Estimation of aquifer parameters under transient and steady-state conditions 1. Maximum-likelihood method incorporating prior information,” *Water Resources Research*, vol. 22, no. 2, pp. 199–210, 1986.

[3] C. Athanasios, “Approximation of large-scale dynamical systems,” *SIAM*, 2005.

[4] D. Kosambi, “Statistics in function space,” *J. Indian Math. Soc.*, vol. 7, pp. 76–88, 1943.

[5] C. Lopez and E. Garcia-Herandez, “Low-dimensional dynamical system model for observed coherent structures in ocean satellite data,” *Physica A*, pp. 238–250, 2003.

[6] G. Berkooz, P. Holmes, and J. Lumley, “The proper orthogonal decomposition in the analysis of turbulent flows,” *Ann. Rev. Fluid Mech*, pp. 777–786, 1993.

[7] C. Yanhua, Z. Jiang, L. Zhendong, and I.M. Navon, “Reduced order modeling of the upper tropical Pacific Ocean model using proper orthogonal decomposition,” *Computers and Mathematics with Application*, pp. 1373–1386, 2006.

[8] C. Yanhua, Z. JJiang, I.M. Navon, and L. Zhendong, “A reduced-order approach to four-dimensional variational data assimilation using proper orthogonal decomposition,” *Int. J. Numer. Meth. Fluids*, pp. 1571–1583, 2007.

[9] M. U. Altaf, M. Verlaan, and A. W. Heemink, “Efficient identification of uncertain parameters in a large-scale tidal model of the European continental shelf by proper orthogonal decomposition,” *International Journal for Numerical Methods in Fluids*, 2012, [Online], doi.: 10.1002/fld.2511.

[10] P. T. M. Vermeulen and A. W. Heemink, “Model-reduced variational data assimilation,” *Monthly Weather Review*, pp. 2888–2899, 2006.

[11] E. Ott, B.R. Hunt, I. Szunyogh, A. V. Zimin, E. J. Kostelich, M. Corazza, E. Kalnay, D. J. Patil, and J. A. Yorke, “A local ensemble Kalman filter for atmospheric data assimilation,” *Tellus*, pp. 415–428, 2004.

[12] P. Sakov and P. R. Oke, “Implication of the form of the ensemble transformation in the ensemble square root filters,” *Mon. Wea. Rev.*, pp. 539–560, 2007.

[13] A. L. Barbu, *Ensemble-based data assimilation schemes for atmospheric chemistry models*, dissertation, Delft University of Technology, 2010.

[14] C. W. Rowley, “Model reduction for fluids, using balanced proper orthogonal decomposition,” *International Journal of Bifurcation and Chaos*, pp. 997–1013, 2005.

[15] G. Evensen, “Sequential data assimilation with a nonlinear quasi-geostrophic model using monte-carlo methods to forecast error statistics,” *J. Geophys. Res.*, pp. 143–162, 1994.

[16] G. Burgers, P. J. Leewen, and G. Evensen, “Analysis scheme in the ensemble Kalman filter,” *Mon. Wea. Rev.*, pp. 1719–1724, 1998.

[17] M.K. Tippett, J.L. Anderson, C.H. Bishop, T. M. Hamill, and J. Whitaker, “Ensemble square root filters.” *Mon. Wea. Rev.*, pp. 1485–1490, 2003.

[18] D. Livings, S. L. Dance, and N. K. Nichols, “Unbiased ensemble square root filters,” *Physica D: Nonlinear Phenomena*, pp. 1021–1028, 2008.

[19] M. Verlaan and A. W. Heemink, “Tidal flow forecasting using reduced-rank square root filter,” *Stochastic Hydro. Hydraul.*, pp. 349–368, 1997.

[20] C. Bishop, B. J. Etherthon, and S. J. Majumdar, “Adaptive sampling with the ensemble transform Kalman filter,” *Mon. Weath. Rev.*, pp. 420–436, 2001.

[21] G. Evensen, “Sampling strategies and square root analysis schemes for the EnKF,” *Ocean Dynamics*, pp. 539–560, 2004.

[22] O. Leeuwenburgh, G. Evensen, and L. Bertino, “The impact of ensemble filter definition on the assimilation of temperature profiles in the tropical Pacific,” *Q. J. Meteorol. Soc.*, pp. 3291–3300, 2005.

[23] X. Wang, C. H. Bishop, and S. J. Julier, “Which is better, an ensemble of positive-negative pairs or a centered spherical simplex ensemble?,” *Mon. Weath. Rev.*, pp. 1590–1605, 2004.

[24] A. W. Heemink, M. Verlaan, and A. J. Segers, “Variance reduced ensemble Kalman filtering,” *Monthly Weather Review*, pp. 1718–1728, 2001.

[25] D. S. Oliver and Y. Chen, “Recent progress on reservoir history matching: a review,” *Computational Geosciences*, pp. 185–221, 2010.

THz Leaky Lens Antenna integrated with Kinetic Inductance Detectors

Andrea Neto[†], **Núria Llombart Juan**[†], **Jochem J. A. Baselmans**[‡],
Andrey Baryshev[‡] and **Stephen Yates**[‡]
[†]*Delft University of Technology,*
Faculty of Electrical Engineering, Mathematics and Computer Science,
Mekelweg 4, 2628 CD Delft, the Netherlands,
e-mail: a.neto@tudelft.nl

[‡] *SRON Netherlands Institute of Space Research, Sorbonnelaan 2, 3584 CA*
Utrecht, the Netherlands

Abstract

This contribution presents the fabrication and measurements of the leaky lens antenna integrated with a cryogenically cooled Kinetic Inductance Detector, in order to achieve an ultra sensitive THz receivers over a bandwidth ranging from 0.15 GHz to 1.5 THz. The system has been manufactured and characterized in terms of power efficiency, and radiation pattern properties. The agreement between the expectations and the measurements is excellent already at this first attempt. These measurements demonstrate the manufacturability and repeatability at THz frequencies of the properties of the leaky lens antenna concept.

1 Introduction

Reflector systems with wideband antenna feeds and arrays receiving growing interest for applications in the THz frequency ranges such as radio astronomy and space observation [1]. For THz space observation, dielectric lens antenna arrays are typically used in focal plane array configurations, due to their easy integration. However, the typical antenna solutions used as feed of dielectric lenses are efficient only over a narrow band [2]. An improved solution is the leaky-lens antenna recently proposed in [3], which can achieve multi-octave bandwidth. This antenna consists of a leaky-wave slot

---

Pulsed Electromagnetic Fields: Their Potentialities, Computation and Evaluation
I. E. Lager and L. J. Jiang (Eds.).
doi: 10.3233/978-1-61499-230-1-121

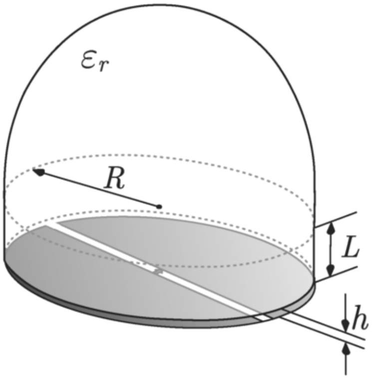

Figure 1: Dielectric lens fed by single leaky-wave slot.

kept at an electrically small distance from the dielectric lens (Fig. 1), in order to obtain directive radiation inside the dielectric and, consequently, efficient illumination of the lens. The leaky-lens was experimentally proved to be non-dispersive and highly efficient over a wide bandwidth in the microwave [4]. Standalone demonstrations of antennas, is typical in the microwave domain. They can be useful, but not conclusive, in the THz regimes due to the importance of parasitic effects that come in when the actual connection of a micro-metric antennas and receivers are eventually realized. In order to be able to characterize an antenna efficiently in the THz frequency domain it is essential to co-design it together with the receiver it is intended to operate with.

This contribution represents the first demonstration of the feasibility of the leaky lens antenna concept at THz frequencies. The antenna is integrated with a cryogenically cooled Kinetic Inductance Detector (KID) [1, 5], so that the two of them would function as an ultra-sensitive receiver over a bandwidth ranging from 0.15 GHz to 1.5 THz. KIDs had previously shown photon noise limited performance at frequencies of 350 GHz in a narrow band [6] in an architecture similar as the one presented here, with however a narrow band twin slot antenna [2]. The present system with KIDS and Leaky Lens Antenna has been manufactured and characterized in terms of, radiation pattern properties at several frequencies.

2 Manufacturing

The functioning of KID detectors as microwave resonators that function as THz power detectors is discussed in [1]. The KID resonator (central in Fig. 2) is coupled to a GHz Transmission line on one side (top portion of

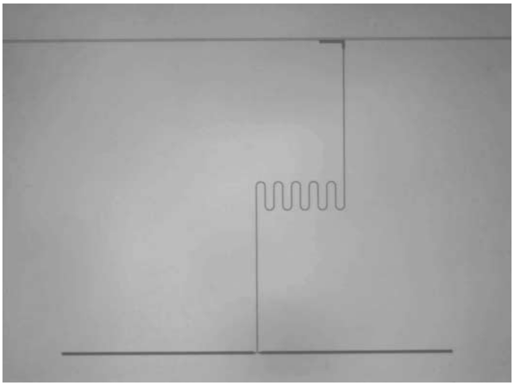

Figure 2: Micrograph from front side with front illumination. The slot is is 4 mm long.

Fig. 2 and the to the THz antenna on the other side (long slot in Fig. 2). The KID resonator is made of a 200 nm thick Tantalum film and provides a virtually frequency independent THz power sensitivity for frequencies above the gap frequency of Tantalum (320 GHz). The key difficulty in manufacturing the antenna was the necessity to print it on a thin 3·m membrane. In the present experiment, we used a SiN membrane deposited on both sides of a Si wafer using PECVD. Using standard lithographic techniques and KOH wet etching of the Si we fabricated a membrane without Si support of 5×5 mm, on the rest of the chip the 525 μm thick Si was left in place below the SiN. Fig. 3 shows the finished chip and in the center the membrane can be observed as a small depression in the thicker wafer. A small ($h = 35, \mu$m) spacing between the slot antenna and the dielectric lens was achieved by laser etching a 30 μm deep suppression in another high resistivity silicon wafer of 350 μm thick (the ‘back-short’). After clamping the chip

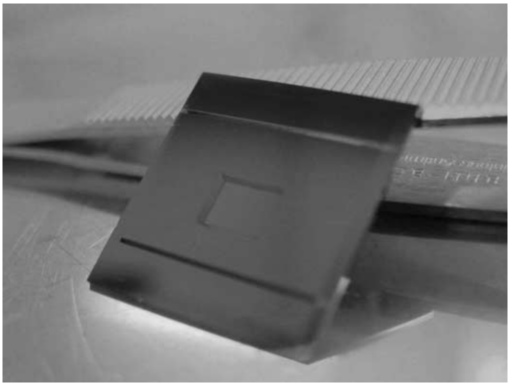

Figure 3: Sample fabrication: finished chip seen from the backside.

in its holder and connecting the feed line via wire bonds to the coax feeds, we glued the spacer chip on top of the detector chip with cyanoacrylate glue, which is present only at the sides of the spacer chip, not behind the antenna feed. On top of the back-short chip we then mounted the Si lens, aligned to the center of the feed, creating the structure shown in Fig. 4.

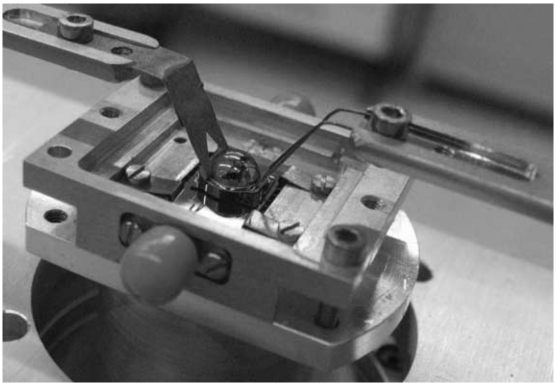

Figure 4: Chip inside the sample holder and position of the lens before gluing.

3 Measurements

The entire system was then located in inside a liquid He cryostat and thermally anchored to the cold stage of a He3 cooler, cooling the detector to 300 mK. In the experiment the lens is facing a window, equipped with IR blockers at 77 K and 4 K and a low pass filter with a cut-off at 1.2 THz at 4 K. A hot load (2000 K), with a few millimeter aperture and equipped with changeable band pass filters was used as THz source and moved at a distance of approximately 20 cm from the lens. Three different filters were located between the source and the receiver: 1) 350 GHz pass band, 2) 650 GHz pass band 3) 850 GHz pass band. These filters provide direct information on frequency performance of the receiver. Without any filter the receiver detects within the 1.2 THz bandwidth given by the filter on the cryostat window. $E-$plane radiation patterns derived from the responsivity of the KIDs as the source was moving in front of the cryostat window are shown for the three investigated frequencies (350 GHz, 650 GHz and 850 GHz) in Fig. 5 (a), (b) and (c), respectively, where they are compared with the pertinent simulation results, obtained using an in house developed tool.

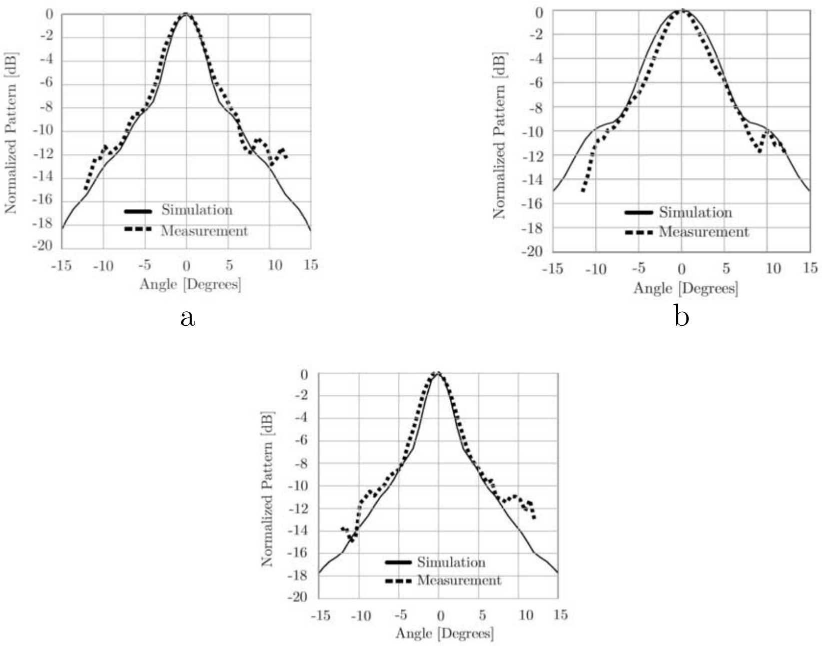

a b

c

Figure 5: Comparison betwene the measuremnts and caculations for $E-$plane radiation patterns at three different frequencies: (a) 350 GHz, (b) 650 GHz and (c) 850 GHz.

Bibliography

[1] A. Baryshev, J. J. A. Baselmans, A. Freni, G. Gerini, H. Hoevers, A. Iacono, and A. Neto, “Progress in antenna coupled kinetic inductance detectors,” *IEEE Terahertz Science Tech.*, vol. 1, no. 1, pp. 112–123, Sep. 2011.

[2] D. F. Filipovic, S. S. Gearhart, and G. M. Rebeiz, “Double-slot antennas on extended hemispherical and elliptical silicon dielectric lenses,” *IEEE Trans. Microw. Theory Tech.*, vol. 41, no. 10, pp. 1738–1749, Oct. 1993.

[3] A. Neto, “Planarly fed leaky lens antenna. Part 1: Theory and design,” *IEEE Trans. Antennas Propag.*, vol. 58, no. 7, pp. 2238–2247, July 2010.

[4] A. Neto, S. Monni, and F. Nennie, “Planarly fed leaky lens antenna. Part 2: Demonstrator and measurements,” *IEEE Trans. Antennas Propag.*, vol. 58, no. 7, pp. 2248–2258, July 2010.

[5] P. K. Day, H. G. LeDuc, B. A. Mazin, A. Vayonakis, and J. Zmuidzinas, “A broadband superconducting detector suitable for use in large arrays,” *Letters to Nature*, vol. 425, pp. 817–821, Oct. 2003.

[6] S. J. C. Yates, J. J. A. Baselmans, A. Endo, R. M. J. Janssen, L. Ferrari, and P. Diener, "Photon noise limited radiation detection with lens-antenna coupled microwave kinetic inductance detectors," *Applied Physics Letters*, vol. 99, 073505, 2011. [Online], doi: 10.1063/1.3624846.

[7] O. Yurduseven, D. Cavallo, and A. Neto, "Dielectric lens fed by coherent connected-slot array as wideband reflector feed," *7^{th} European Conference on Antennas and Propagation – EuCAP*, submitted.

Wireless digital information transfer: modelling, prediction and assessment

Ioan E. Lager[†], **Adrianus T. de Hoop**[†] and **Takamaro Kikkawa**[‡]
[†]*Delft University of Technology,*
Faculty of Electrical Engineering, Mathematics and Computer Science,
Mekelweg 4, 2628 CD Delft, the Netherlands,
e-mail: i.e.lager@tudelft.nl

[‡]*Research Institute for Nanodevice and Bio Systems,*
Hiroshima University, 1-4-2 Kgamiyama, Higashi-Hiroshima,
Hiroshima, 739-8527, Japan

Abstract

The loop-to-loop pulsed electromagnetic field wireless signal transfer is investigated with a view on its application in wireless digital information transfer. Closed-form expressions are derived for the emitted magnetic field and for the open-circuit voltage of the receiving loop in dependence on the mutual orientation of the loops and the characteristics of the feeding pulse. Numerical results are given for some configurations that are representative for microelectronic wireless signal transfer. In them, the transmitting loop is excited with a monocycle pulse electric current and with a propitious, causal, ultra wide-band pulse. The results are indicative for the potentialities of the pulsed-field wireless signal transfer concerning the received signal characteristics and the system's compliance with regulatory specifications on ElectroMagnetic Emission.

1 Introduction

Wireless data transfer is cornerstone to information technology, whether for providing network access to the exploding number of mobile terminals or for ensuring wireless integrated circuit (IC) interconnects [1–5]. The practical realisation of such systems is the subject of extensive research, with investigations ranging from abstract channel management principles to

---

Pulsed Electromagnetic Fields: Their Potentialities, Computation and Evaluation
I. E. Lager and L. J. Jiang (Eds.).
doi: 10.3233/978-1-61499-230-1-127

concrete IC implementations. However, prior to approaching such matters, two questions as to the wireless links' functionality have to be addressed: are the signal levels involved sufficiently high for their proper system performance, and do the (inevitable) field emission levels comply with the pertaining (international) regulations on ElectroMagnetic Interference (EMI)?

It is now stressed that digital electronic systems inherently operate in the time domain. Hence, an investigation into their properties is naturally, and most adequately, carried out with time-domain (rather than frequency-domain), analytical and computational, mathematical tools. In this respect, [6] formulated a full time-domain methodology for analysing the susceptibility of microwave electronic circuits to pulsed field electromagnetic (EM) disturbances.

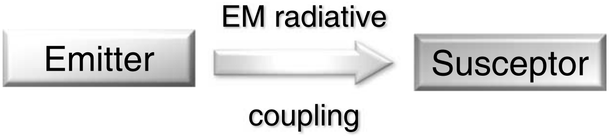

Figure 1: The ElectroMagnetic Interference (EMI) triptych.

The framework in [6] is used as a starting point to studying a configuration consisting of a single transmitting loop and a single receiving loop in free space – the simplest representative circuit instantiation of the standard EMI-triptych (see Fig. 1) in the realm of wireless signal transfer. The transmitting loop is excited by a suitable pulsed electric current. The open-circuit generator voltage source of the equivalent Thévenin Kirchhoff circuit of the receiving loop is determined via Faraday's induction law. In the model, the loops are located in free space and the coupling pulsed magnetic field is calculated from the Maxwell field equations. Once the mechanisms governing the signal performance of this simple (in fact, the simplest) model configuration are fully understood, the more complicated configurations met in practice can become amenable to further analysis.

As to the electromagnetic emission properties of the system, the time-domain magnetic field that performs the wireless signal transmission carries the full information. Whether or not this field interferes with other digital electronic systems, too, is a matter of pulsed field and is of concern to the designer. However, international, in particular, Federal Communications Commission (FCC) regulations on electromagnetic emission and ElectroMagnetic Interference (EMI), are still exclusively formulated in terms of the frequency-domain properties of devices and systems (with [7, 8] as the most widely cited ultra wide-band (UWB) emission regulation). It is, *a priori* unclear in which sense these two aspects share a range of compatibility, but a discussion on this matter is outside the scope of this study.

This work proceeds now by evaluating the loop-to-loop signal transfer and the pertaining energy spectral density of the emitted field, the employed formulation following that in [9]. The ensuing numerical results illustrate the complexity and the intricateness in already this, simplest, configuration. A first study will concern the signal level assessment, the transmitting loop being fed by a monocycle pulse electric current (with no electric charge transport over time)[1]. We will then study the emission level compliance for the loop-to-loop signal transfer, the transmitting loop being fed in that case by an UWB, causal pulse with a spectral behaviour that adequately fills the spectral masks in [8].

2 Prerequisites

2.1 Description of the configuration

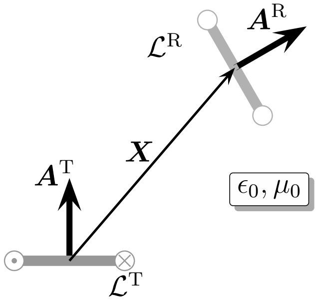

Figure 2: Configuration concerning the pulsed signal transfer between a transmitting wire loop $\mathcal{L}^{\mathrm{T}}$ and a receiving wire loop $\mathcal{L}^{\mathrm{R}}$.

The discussed configuration is shown in Fig. 2. In it, position is specified by the coordinates $\{x, y, z\}$ with respect to a Cartesian reference frame with the origin $\mathcal{O}$ and the three mutually perpendicular base vectors $\{\boldsymbol{i}_x, \boldsymbol{i}_y, \boldsymbol{i}_z\}$ of unit length each that, in the indicated order, form a right-handed system. The position vector is $\boldsymbol{x} = x\boldsymbol{i}_x + y\boldsymbol{i}_y + z\boldsymbol{i}_z$. The time coordinate is t. The transmitting loop $\mathcal{L}^{\mathrm{T}}$ has $\boldsymbol{x} = \boldsymbol{x}^{\mathrm{T}}$ as its reference center and $\boldsymbol{A}^{\mathrm{T}} = \boldsymbol{i}_{\boldsymbol{A}^{\mathrm{T}}} A^{\mathrm{T}}$ (with $|\boldsymbol{i}_{\boldsymbol{A}^{\mathrm{T}}}| = 1$) as its vectorial area. The receiving loop $\mathcal{L}^{\mathrm{R}}$ has $\boldsymbol{x} = \boldsymbol{x}^{\mathrm{R}}$ as its reference center and $\boldsymbol{A}^{\mathrm{R}} = \boldsymbol{i}_{\boldsymbol{A}^{\mathrm{R}}} A^{\mathrm{R}}$ (with $|\boldsymbol{i}_{\boldsymbol{A}^{\mathrm{R}}}| = 1$) as its vectorial area. The relative vectorial position of the loops is $\boldsymbol{X} = \boldsymbol{x}^{\mathrm{R}} - \boldsymbol{x}^{\mathrm{T}}$ (with

---

[1] For the exciting monocycle pulse we use a mathematical model with three parameters that comply both with the International Electrotechnical Vocabulary (IEV) of the International Electrotechnical Commission (IEC) [10] and with signal processing usage.

$\boldsymbol{X}/|\boldsymbol{X}| = \boldsymbol{\Xi}$). The included angle between $\boldsymbol{\Xi}$ and $\boldsymbol{i}_{\boldsymbol{A}^{\mathrm{T}}}$ is ϑ. The coupling path between the loops is free space, with electric permittivity ϵ_0, magnetic permeability μ_0 and wave speed $c_0 = (\epsilon_0\mu_0)^{-1/2}$. The loops are assumed to have maximum diameters that are small compared with the spatial extent of the exciting pulses.

2.2 The exciting pulses

The excitation of the transmitting loop is taken as pulsed electric currents having a *causal* time behaviour. The following pulses will be employed:

- the *time differentiated power exponential pulse* (∂_tPE) [14] (see Appendix A.1);
- the *power exponential modulated – sinc-cosine pulse* (PE–sinc-cosine) [15] (see Appendix A.2).

2.3 The radiated field

By denoting as $t' = t - |\boldsymbol{X}|/c_0$ the wave travel time retarded, time coordinate, the magnetic field strength $\boldsymbol{H}^{\mathrm{T}}$ generated by $\mathcal{L}^{\mathrm{T}}$ is given by [11, p. 761]

$$\boldsymbol{H}^{\mathrm{T}}(\boldsymbol{X},t) = \frac{A^{\mathrm{T}}}{4\pi|\boldsymbol{X}|^3}\left\{\boldsymbol{\Theta}_{\boldsymbol{H}}^{\mathrm{NF}}\left[I^{\mathrm{T}}(t') + \frac{|\boldsymbol{X}|}{c_0}\partial_t I^{\mathrm{T}}(t')\right] + \boldsymbol{\Theta}_{\boldsymbol{H}}^{\mathrm{FF}}\frac{|\boldsymbol{X}|^2}{c_0^2}\partial_t^2 I^{\mathrm{T}}(t')\right\} \quad (1)$$

in which

$$\boldsymbol{\Theta}_{\boldsymbol{H}}^{\mathrm{NF}}(\boldsymbol{i}_{\boldsymbol{A}^{\mathrm{T}}},\boldsymbol{\Xi}) = 3\left(\boldsymbol{\Xi}\cdot\boldsymbol{i}_{\boldsymbol{A}^{\mathrm{T}}}\right)\boldsymbol{\Xi} - \boldsymbol{i}_{\boldsymbol{A}^{\mathrm{T}}} \quad (2)$$

is the *near-field radiated field directional characteristic* and

$$\boldsymbol{\Theta}_{\boldsymbol{H}}^{\mathrm{FF}}(\boldsymbol{i}_{\boldsymbol{A}^{\mathrm{T}}},\boldsymbol{\Xi}) = \left(\boldsymbol{\Xi}\cdot\boldsymbol{i}_{\boldsymbol{A}^{\mathrm{T}}}\right)\boldsymbol{\Xi} - \boldsymbol{i}_{\boldsymbol{A}^{\mathrm{T}}} \quad (3)$$

is the *far-field radiated field directional characteristic.*

2.4 Receiving loop equivalent Thévenin circuit

Application of the electromagnetic reciprocity theorem of the time-convolution type leads to the following expression for the equivalent Thévenin circuit generator voltage in $\mathcal{L}^{\mathrm{R}}$ [12]

$$\begin{aligned} V^{\mathrm{G}}(\boldsymbol{X},t') = -\frac{\mu_0 A^{\mathrm{T}}A^{\mathrm{R}}}{4\pi|\boldsymbol{X}|^3}\Big\{&\Theta^{\mathrm{NF}}(\boldsymbol{i}_{\boldsymbol{A}^{\mathrm{T}}},\boldsymbol{i}_{\boldsymbol{A}^{\mathrm{R}}},\boldsymbol{\Xi})\left[\partial_t I^{\mathrm{T}}(t') + \frac{|\boldsymbol{X}|}{c_0}\partial_t^2 I^{\mathrm{T}}(t')\right] \\ &+\Theta^{\mathrm{FF}}(\boldsymbol{i}_{\boldsymbol{A}^{\mathrm{T}}},\boldsymbol{i}_{\boldsymbol{A}^{\mathrm{R}}},\boldsymbol{\Xi})\frac{|\boldsymbol{X}|^2}{c_0^2}\partial_t^3 I^{\mathrm{T}}(t')\Big\} \end{aligned} \quad (4)$$

in which

$$\Theta^{\mathrm{NF}}(\boldsymbol{i}_{\boldsymbol{A}^{\mathrm{T}}}, \boldsymbol{i}_{\boldsymbol{A}^{\mathrm{R}}}, \boldsymbol{\Xi}) = 3\left(\boldsymbol{\Xi}\cdot\boldsymbol{i}_{\boldsymbol{A}^{\mathrm{T}}}\right)\left(\boldsymbol{\Xi}\cdot\boldsymbol{i}_{\boldsymbol{A}^{\mathrm{R}}}\right) - \boldsymbol{i}_{\boldsymbol{A}^{\mathrm{T}}}\cdot\boldsymbol{i}_{\boldsymbol{A}^{\mathrm{R}}} \tag{5}$$

is the *near-field directional characteristic* and

$$\Theta^{\mathrm{FF}}(\boldsymbol{i}_{\boldsymbol{A}^{\mathrm{T}}}, \boldsymbol{i}_{\boldsymbol{A}^{\mathrm{R}}}, \boldsymbol{\Xi}) = \left(\boldsymbol{\Xi}\cdot\boldsymbol{i}_{\boldsymbol{A}^{\mathrm{T}}}\right)\left(\boldsymbol{\Xi}\cdot\boldsymbol{i}_{\boldsymbol{A}^{\mathrm{R}}}\right) - \boldsymbol{i}_{\boldsymbol{A}^{\mathrm{T}}}\cdot\boldsymbol{i}_{\boldsymbol{A}^{\mathrm{R}}} \tag{6}$$

is the *far-field directional characteristic.*

3 Loop-to-loop signal transfer

The loop-to-loop signal transfer is analysed for the two canonical configurations in Fig. 3. The case of two parallel loops is representative of for planar microelectronic configurations, the case of two perpendicular loops for 3D microelectronic ones. In the realm of microelectronic circuit design the parameters that are more or less open to choice are: the mutual orientation of the loops, in general, their mutual distance and the parameters of the pulse shape. Some of these are discussed below.

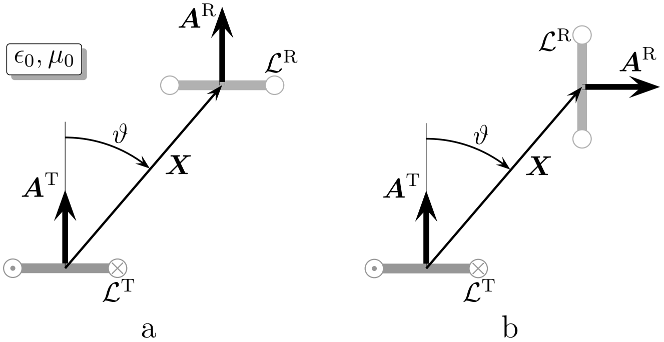

Figure 3: Canonic configurations for the study of the pulsed signal transfer in a loop-to-loop wireless signal transfer. (a) Mutually parallel loops $\boldsymbol{A}^{\mathrm{T}}\cdot\boldsymbol{A}^{\mathrm{R}} = A^{\mathrm{T}}A^{\mathrm{R}}$; (b) mutually perpendicular loops $\boldsymbol{A}^{\mathrm{T}}\cdot\boldsymbol{A}^{\mathrm{R}} = 0$.

Mutually parallel loops

In this case, $\boldsymbol{A}^{\mathrm{T}}\cdot\boldsymbol{A}^{\mathrm{R}} = A^{\mathrm{T}}A^{\mathrm{R}}$ and the directional characteristics are

$$\Theta^{\mathrm{NF}}(\boldsymbol{i}_{\boldsymbol{A}^{\mathrm{T}}}, \boldsymbol{i}_{\boldsymbol{A}^{\mathrm{R}}}, \boldsymbol{\Xi}) = 3\cos^2(\vartheta) - 1 \tag{7}$$

$$\Theta^{\mathrm{FF}}(\boldsymbol{i}_{\boldsymbol{A}^{\mathrm{T}}}, \boldsymbol{i}_{\boldsymbol{A}^{\mathrm{R}}}, \boldsymbol{\Xi}) = \cos^2(\vartheta) - 1. \tag{8}$$

These expressions show that the near-field constituent yields zero contribution to $V^{\mathrm{G}}(\boldsymbol{X}, t')$ for $\cos(\vartheta) = \pm 3^{-1/2}$ and that the far-field constituent yields zero contribution for $\cos(\vartheta) = \pm 1$.

Mutually perpendicular loops

In this case, $(\boldsymbol{A}^{\mathrm{T}} \cdot \boldsymbol{A}^{\mathrm{R}} = 0)$ and the directional characteristics expressed in terms of the standard spherical coordinates $\{\vartheta, \varphi\}$[2] are

$$\Theta^{\mathrm{NF}}(\boldsymbol{i}_{\boldsymbol{A}^{\mathrm{T}}}, \boldsymbol{i}_{\boldsymbol{A}^{\mathrm{R}}}, \Xi) = (3/2)\sin(2\vartheta)\sin(\varphi) \tag{9}$$

$$\Theta^{\mathrm{FF}}(\boldsymbol{i}_{\boldsymbol{A}^{\mathrm{T}}}, \boldsymbol{i}_{\boldsymbol{A}^{\mathrm{R}}}, \Xi) = (1/2)\sin(2\vartheta)\sin(\varphi) \tag{10}$$

implying that $V^{\mathrm{G}}(\boldsymbol{X}, t')$ vanishes at $\vartheta = \{0, \pi/2, \pi\}$ and at $\varphi = \{0, \pi\}$.

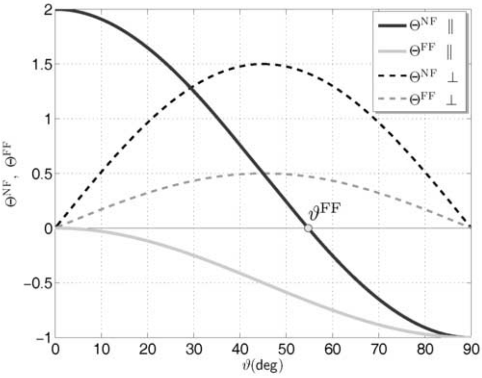

Figure 4: Angular dependence of the directional characteristics for $\varphi = \pi/2$.

The directional characteristics (7)–(10) are plotted in Fig. 4. It evidences that the mutually parallel configuration allows obtaining stronger loop-to-loop link signals. The figure also shows the orientations that provide the best coupling and those with vanishing coupling. This information is relevant for the design of wireless signal transfer systems.

4 Energy spectral density of the emitted field

The FCC regulations identify the *power spectral density* of the emitted field as the quantity for which admissible levels are specified [8]. Since this work concerns pulsed fields, we interpret these regulations as applying to the

---

[2] The spherical coordinate system has the origin at the center of the transmitting wire loop, $\boldsymbol{i}_{\boldsymbol{A}^{\mathrm{T}}}$ is the polar axis and φ measures the trigonometric rotation from $\boldsymbol{i}_{\boldsymbol{A}^{\mathrm{R}}}$.

energy spectral density of the emitted field. Furthermore, for a proper information transfer in a pulse-operated communication system, pulse crowding is to be avoided. The regulation can then be taken to apply to a single pulse. In view of these considerations, the energy spectral density of the electromagnetic field emitted by the transmitting loop is determined. Since the embedding medium is lossless, the total energy radiated by the loop follows from the corresponding expression in the far-field region. Upon writing [11, Section 26.10]

$$\{\boldsymbol{E}^{\mathrm{T}},\boldsymbol{H}^{\mathrm{T}}\}(\boldsymbol{X},t) = \frac{\{\boldsymbol{E}^{\mathrm{T};\infty},\boldsymbol{H}^{\mathrm{T};\infty}\}(\boldsymbol{\Xi},t-|\boldsymbol{X}|/c_0)}{4\pi|\boldsymbol{X}|}[1+o(1)] \text{ as } |\boldsymbol{X}|\to\infty \tag{11}$$

in which, on account of (1),

$$\boldsymbol{H}^{\mathrm{T};\infty}(\boldsymbol{\Xi},t) = A^{\mathrm{T}}\boldsymbol{\Theta}_H^{\mathrm{FF}}\frac{1}{c_0^2}\partial_t^2 I^{\mathrm{T}}(t) \tag{12}$$

and

$$\boldsymbol{E}^{\mathrm{T};\infty}(\boldsymbol{\Xi},t) = (\mu_0/\epsilon_0)^{1/2}\boldsymbol{H}^{\mathrm{T};\infty}(\boldsymbol{\Xi},t)\times\boldsymbol{\Xi} \tag{13}$$

the total energy W^{rad} radiated by the loop is

$$W^{\mathrm{rad}} = \left(\frac{1}{4\pi}\right)^2\left(\frac{\mu_0}{\epsilon_0}\right)^{1/2}\int_{\boldsymbol{\Xi}\in\Omega}\mathrm{d}\Omega\int_{t=-\infty}^{\infty}|\boldsymbol{H}^{\mathrm{T};\infty}(\boldsymbol{\Xi},t)|^2\mathrm{d}t \tag{14}$$

where $\Omega = \{|\boldsymbol{\Xi}| = 1\}$ is the sphere of unit radius. In view of Parseval's theorem, this expression is equivalent to

$$W^{\mathrm{rad}} = \int_{f=-\infty}^{\infty} w^{\mathrm{rad}}(f)\mathrm{d}f = 2\int_{f=0}^{\infty} w^{\mathrm{rad}}(f)\mathrm{d}f \tag{15}$$

in which the *energy spectral density* $w^{\mathrm{rad}}(f)$ of the radiated field is given by

$$w^{\mathrm{rad}}(f) = \left(\frac{1}{4\pi}\right)^2\left(\frac{\mu_0}{\epsilon_0}\right)^{1/2}\int_{\boldsymbol{\Xi}\in\Omega}|\hat{\boldsymbol{H}}^{\mathrm{T};\infty}(\boldsymbol{\Xi},2\pi\mathrm{j}f)|^2\mathrm{d}\Omega. \tag{16}$$

Using (12), together with

$$\int_{\boldsymbol{\Xi}\in\Omega}\boldsymbol{\Theta}_H^{\mathrm{FF}}\cdot\boldsymbol{\Theta}_H^{\mathrm{FF}}\mathrm{d}\Omega = \frac{8\pi}{3} \tag{17}$$

we obtain

$$W^{\mathrm{rad}}(f) = \frac{8\pi}{3}\left(\frac{A^{\mathrm{T}}}{4\pi}\right)^2\left(\frac{\mu_0}{\epsilon_0}\right)^{1/2}\frac{1}{c_0^4}\int_{t=0}^{\infty}\left[\partial_t^2 I(t)\right]^2\mathrm{d}t \tag{18}$$

and

$$w^{\mathrm{rad}}(f) = \frac{8\pi^3}{3}(A^{\mathrm{T}})^2\left(\frac{\mu_0}{\epsilon_0}\right)^{1/2}\frac{1}{c_0^4}f^4|\hat{I}^{\mathrm{T}}(2\pi\mathrm{j}\,f)|^2. \tag{19}$$

Substitution of (22) in (19) yields the thought for energy spectral density of the emitted field in closed-form. This quantity is to be compared with prescribed spectral masks for verifying the system's compliance with regulatory specifications, an approach that will be used in Section 5.2.

5 Illustrative numerical results

Some illustrative numerical results are now discussed for the case of two *mutually parallel*, identical small loops with $A^{\mathrm{T}} = A^{\mathrm{R}} = 0.0314\,\mathrm{mm}^2$ (for circular loops, this amounts to a diameter of 0.2 mm, a dimension that is consistent with the implementation choices in [13]).

5.1 Loop-to-loop signal transfer

The feeding pulse employed in this experiment is a ∂_tPE with the parameters: $I_{\mathrm{peak}} = 1\,\mathrm{mA}$, $t_{\mathrm{r}} = 0.1\,\mathrm{ns}$ and $\nu = 4$ (see Appendix A.1 for its time signature and spectral diagram).

The receiving antenna response is evaluated at:

- $|\boldsymbol{X}| = 2\,\mathrm{mm}$ – an upper bound for:the inter-spacing between loops located inside the same IC (see Fig. 5 (a)); this study is relevant for signal transfer in intra-chip communication;
- $|\boldsymbol{X}| = 50\,\mathrm{mm}$ – representative for the inter-spacing between widely spaced IC's of the same device or between IC's of nearby located devices, (see Fig. 5 (b)); this study is relevant for an EMI evaluation.

The magnitude of the first peak $|V^{\mathrm{G}}|$ at $|\boldsymbol{X}| = 2\,\mathrm{mm}$ (where the $\partial_t I^{\mathrm{T}}(t)$ behavior dominates) is approximately $3.1\,\mu\mathrm{V}$, a value that can be easily detected with standard circuitry. As predicted by (7), the peak value corresponds to $\vartheta = 0°$ that, in view of the IC's characteristic flat aspect ratio, corresponds to the most frequently encountered situation. However, note that the change in sign of the first peak for $\vartheta > \arccos\left(3^{-1/2}\right)$ can lead to difficulties in interpreting the information contained in a succession of pulses.

At $|\boldsymbol{X}| = 50\,\mathrm{mm}$ (where the $\partial_t^3 I^{\mathrm{T}}(t)$ behavior dominates) the magnitude of the peak $|V^{\mathrm{G}}|$ drops drastically to below $2.3\,\mathrm{nV}$ a value that can be adequately suppressed by the immunity rejection circuitry of the 'victim' IC's. As predicted by (8), the peak value corresponds to $\vartheta = 90°$.

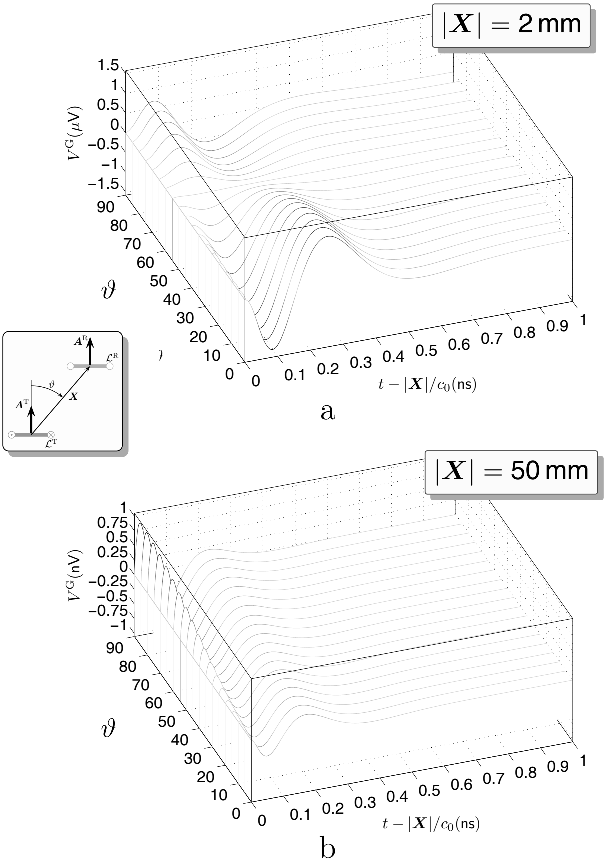

Figure 5: Pulsed signal transfer between *mutually parallel* loops. $\mathcal{L}^T$ is excited by means of a ∂_tPE. (a) Receive antenna response for $|\boldsymbol{X}| = 2\,\mathrm{mm}$ (predominantly $\partial_t I^T(t)$ behavior); (b) Receive antenna response for $|\boldsymbol{X}| = 50\,\mathrm{mm}$ (predominantly $\partial_t^3 I^T(t)$ behavior). The purple vertical lines correspond to $\vartheta = \arccos\left(3^{-1/2}\right)$.

It must be noted that the conditions under which this analysis was carried out are highly idealized, namely unobstructed, free space radiative coupling path between the emitter and the susceptor. The link inside a real IC occurs in an highly heterogeneous environment that will distort and attenuate severely the received signals. Nonetheless, our analysis evidences *the potentiality* of the loop-to-loop wireless interconnect to establish a viable intra-chip link, that is a requisite first step in any design process and provides a valuable interpretation instrument for the signal processing aiming at recovering the original signal. Furthermore, from an EMI perspective, it gives an impression of the orders of magnitude that can be expected in another 'victim' IC using a similar intra-chip signal transfer technology.

5.2 Energy spectral density analysis

This analysis is carried out based on (19) for the chosen transmitting wire loop. The spectral behaviour of the emitted magnetic field is assessed against the *normalised* FCC mask for UWB hand-held systems [8, p. K.36] in the 3.1–10.6 GHz frequency band. To this end, the feeding current pulse is taken as a PE–sinc-cosine (see Appendix A.2) with parameters: $K_{\mathrm{sc}} = 10$, $\nu = 3$, $B = 7.5\,\mathrm{GHz}$ and $f_{\mathrm{c}} = 6.85\,\mathrm{GHz}$. As shown in Fig. 8, the spectral diagram of this pulse fills almost completely the prescribed mask, with a practically flat, wide-band behaviour and a steep falloff outside this band, yielding a -19.15 dB normalised energy spectral density level at both 3.1 GHz and 10.6 GHz.

The energy spectral density is plotted in Fig. 6, evidencing the full compliance of the loop-to-loop transfer for the chosen UWB feeding pulse. It then follows that *for this pulse signature* the selection of the feeding current I_0 for ensuring compliance with regulatory specifications must be done based on the mask level at 10 GHz. This value is then used for verifying the system's functionality by performing the loop-to-loop signal transfer analysis.

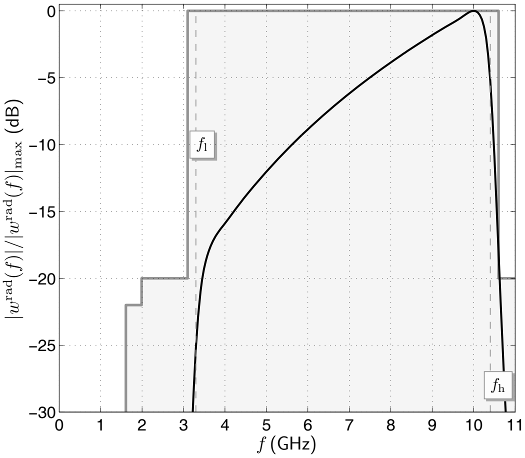

Figure 6: Energy spectral density assessment. The shaded area corresponds to the normalised FCC mask for UWB hand-held systems [8, p. K.36].

6 Conclusions

The loop-to-loop pulsed electromagnetic field wireless signal transfer was investigated in configurations that are of relevance for microelectronic systems and devices. The derived closed-form expressions for the emitted magnetic field and for the open-circuit voltage of the receiving loop provide valuable design rules as concerns the influence of the mutual orientation of the loops and of the parameters of the feeding pulse on both the emitted field (EMI evaluation) and the received pulse (system performance prediction). Numerical results were given for some configurations that are of relevance for intra-chip communication systems. The results highlighted the potentialities of the pulsed-field wireless signal transfer for the relevant application but also evidenced the intricate received pulses' dependence on the relative orientation of the loops, an aspect that may result in difficulties in interpreting the transferred information. The compliance with regulatory specifications on ElectroMagnetic Emission was studied by evaluating the behavior of the energy spectral density in the FCC ultra wide-band spectrum.

Appendix

A The exciting pulses

A.1 The time differentiated power exponential pulse

The ∂_tPE pulse follows as the time derivative of the IEC 60050 − IEV normalised, unipolar *power exponential pulse* [14]

$$I(t) = I_{\mathrm{peak}} N(\nu) \left(1 - \frac{t}{t_{0\mathrm{x}}}\right) \left(\frac{t}{t_{0\mathrm{x}}}\right)^{\nu-1} \exp\left[-\nu\left(\frac{t}{t_{0\mathrm{x}}} - 1\right)\right] H(t) \text{ for } \nu > 1 \tag{20}$$

in which I_{peak} is the magnitude of the first peak in $I(t)$, $t_{0\mathrm{x}}$ is the pulse zero-crossing time (equaling the pulse rise time t_{r} of the power exponential pulse), ν is the initial rise power of the latter pulse (which is related to the high-frequency asymptotic falloff in the corresponding Bode plot) and $N(\nu)$ is the normalisation constant

$$N(\nu) = \nu^{1/2} \left(\frac{\nu^{1/2}}{\nu^{1/2} - 1}\right)^{\nu-1} \exp(-\nu^{1/2}). \tag{21}$$

The pulse carries no net electric charge. The time Laplace transform of (20) is

$$\hat{I}(s) = I_{\mathrm{peak}}\, t_{0\mathrm{x}}\, N(\nu)\, \frac{s\, t_{0\mathrm{x}} \Gamma(\nu) \exp(\nu)}{(s\, t_{0\mathrm{x}} + \nu)^{\nu+1}} \text{ for } \mathrm{Re}(s) > -\nu/t_{0\mathrm{x}} \tag{22}$$

where Γ denotes the Euler gamma function. The relevant Fourier transformation follows from (22) taking $s = \mathrm{j}\omega = \mathrm{j}2\pi f$, with $\omega \in \mathbb{R}$ denoting the angular frequency and $f \in \mathbb{R}$ the frequency.

The normalised time signatures and corresponding normalised spectral diagrams of the ∂_tPE pulse used in Section 5.1 are given in Fig. 7.

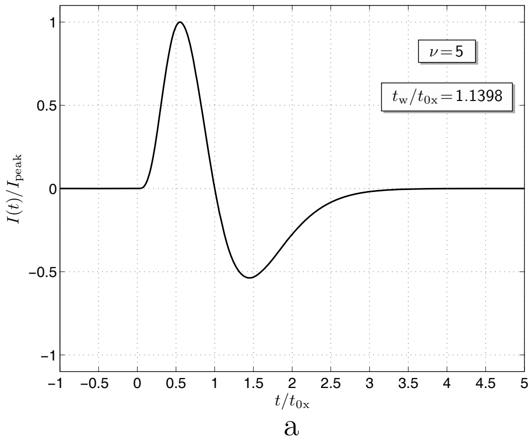

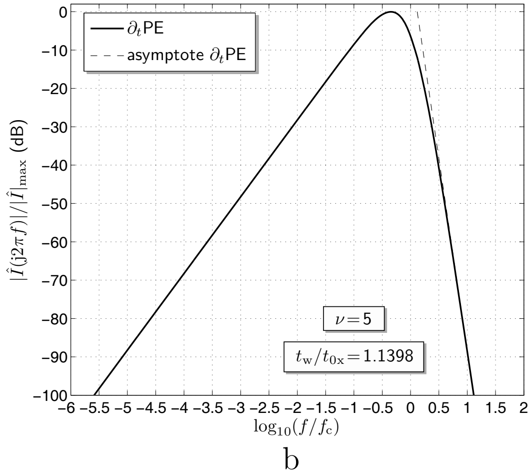

Figure 7: ∂_tPE pulse with $\nu = 5$. (a) Normalised time signature; (b) normalised spectral diagrams.

A.2 The power exponential modulated – sinc-cosine pulse

This pulse is constructed by using the IEC 60050 – IEV normalised, unipolar *power exponential pulse* [14]

$$I_{PE}(t) = I_0 \,(t/t_r)^{\nu} \exp\left[-\nu\,(t/t_r - 1)\right] H(t) \tag{23}$$

in which I_0 denotes the pulse amplitude, $t_r > 0$ the pulse rise time, $\nu > 0$ the pulse power and $H(t)$ the Heaviside unit step function, as an *envelope* for the a *non-causal* sinc-cosine function (carrier)

$$G(t) = \mathrm{sinc}[B(t - t_0)] \cos\left[2\pi f_c(t - t_0)\right] \tag{24}$$

in which

$$\mathrm{sinc}(x) \overset{\mathrm{def}}{=} \frac{\sin(\pi x)}{\pi x} \quad x \in \mathbb{R} \tag{25}$$

t_0 is an arbitrary delay, $B = f_\mathrm{h} - f_\mathrm{l}$, with $0 < f_\mathrm{l} < f_\mathrm{h}$, is a (prescribed) bandwidth and $f_\mathrm{c} = (f_\mathrm{l} + f_\mathrm{h})/2$. By taking $t_0 = t_\mathrm{r}$, the PE–sinc-cosine pulse follows as

$$\begin{aligned} I(t) = I_0\,(t/t_\mathrm{r})^\nu\,\mathrm{sinc}\left[B(t-t_\mathrm{r})\right]\cos\left[2\pi f_\mathrm{c}(t-t_\mathrm{r})\right] \\ \exp\left[-\nu\,(t/t_\mathrm{r}-1)\right]H(t). \end{aligned} \tag{26}$$

For simplicity, we confine ν to integer values, only. Furthermore, in our experiments we interrelate B and t_r via

$$t_\mathrm{r} = K_\mathrm{sc}/B, \text{ with } K_\mathrm{sc} = 1, 2, 3, \ldots \tag{27}$$

The Fourier transform of the PE–sinc-cosine pulse is obtained by applying the convolution theorem [16, p. 115] this yielding

$$\begin{aligned} \hat{I}(\mathrm{j}\omega) &= \frac{1}{2\pi}\left[\hat{I}_\mathrm{PE}(\mathrm{j}\omega) \overset{(\mathrm{j}\omega)}{*} \hat{G}(\mathrm{j}\omega)\right] \\ &= I_0\,\frac{\exp(-\mathrm{j}\omega t_\mathrm{r})}{4\pi B}\left[\mathcal{I}\left(\omega-\omega_\mathrm{h},\omega-\omega_\mathrm{l}\right) + \mathcal{I}\left(\omega+\omega_\mathrm{l},\omega+\omega_\mathrm{h}\right)\right] \end{aligned} \tag{28}$$

where $\overset{(\mathrm{j}\omega)}{*}$ denotes frequency convolution and

$$\begin{aligned} &\mathcal{I}\left(\omega_\mathrm{i},\omega_\mathrm{f}\right) = \int_{\omega_\mathrm{i}}^{\omega_\mathrm{f}}\left[\exp(\mathrm{j}\omega' t_\mathrm{r})\hat{P}(\mathrm{j}\omega')\right]\mathrm{d}\omega' \\ &= I_0\,t_\mathrm{r}\,\Gamma(\nu+1)\,\exp(\nu)\int_{\omega_\mathrm{i}}^{\omega_\mathrm{f}}\frac{\exp(\mathrm{j}\omega' t_\mathrm{r})}{(\mathrm{j}\,t_\mathrm{r}\,\omega'+\nu)^{\nu+1}}\,\mathrm{d}\omega' \\ &= I_0\left(\exp(\nu)\int_{t_\mathrm{r}\omega_\mathrm{i}}^{t_\mathrm{r}\omega_\mathrm{f}}\frac{\exp(\mathrm{j}\,\xi)}{\mathrm{j}\,\xi+\nu}\,\mathrm{d}\xi + \mathrm{j}\sum_{m=1}^{\nu}\left\{\Gamma(m)\,\left[\exp(\alpha)\,\alpha^{-\nu+m-1}\right]\Big|_{\alpha_\mathrm{i}}^{\alpha_\mathrm{f}}\right\}\right) \end{aligned} \tag{29}$$

with $\alpha_\mathrm{i} = \mathrm{j}\,t_\mathrm{r}\,\omega_\mathrm{i} + \nu$ and $\alpha_\mathrm{f} = \mathrm{j}\,t_\mathrm{r}\,\omega_\mathrm{f} + \nu$. The integral arrived at in (29) cannot be solved analytically but is amenable to numeric evaluation, e.g., by means of the Matlab® `quadl` function.

The normalised time signatures and corresponding normalised spectral diagrams of the PE–sinc-cosine pulse used in Section 5.2 are given in Fig. 8.

Bibliography

[1] M.-C. F. Chang, V. P. Roychowdhury, L. Zhang, H. Shin, and Y. Qian, "RF/wireless interconnect for inter- and intra-chip communications," *Proc. IEEE*, vol. 89, no. 4, pp. 456–466, April 2001.

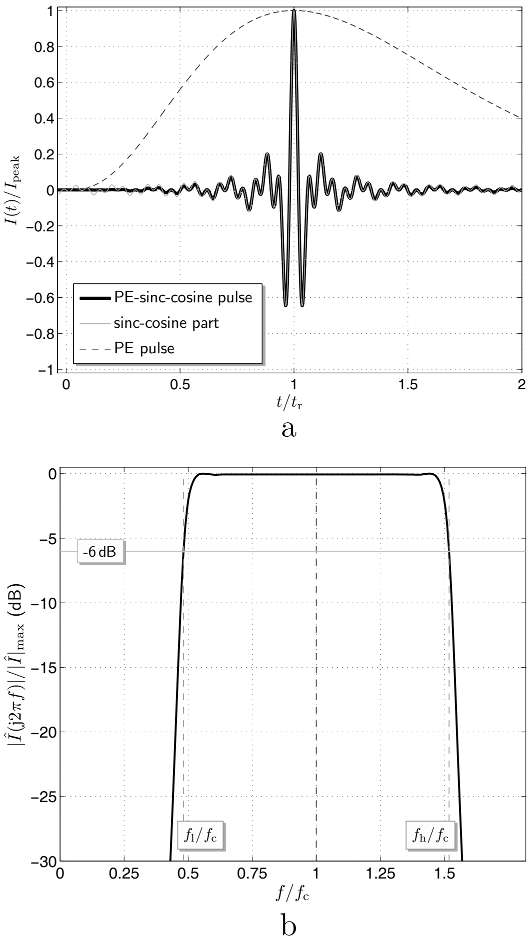

Figure 8: PE–sinc-cosine pulse with $K_{\text{sc}} = 13$, $\nu = 3$, $B = 7.1\,\text{GHz}$ and $f_{\text{c}} = 6.85\,\text{GHz}$ (corresponding to $f_{\text{l}} = 3.3\,\text{GHz}$ and $f_{\text{h}} = 10.4\,\text{GHz}$). (a) Normalised time signature; (b) normalised spectral diagrams. The normalised energy spectral density level at 3.1 GHz and 10.6 GHz (the mask's band limits) amounts to -19.15 dB.

[2] B. A. Floyd, C.-M. Hung, and K. K. O, "Intra-chip wireless interconnect for clock distribution implemented with integrated antennas, receivers, and transmitters," *IEEE J. Solid-State Circuits*, vol. 37, no. 5, pp. 543–552, May 2002.

[3] "On-chip antennas in Silicon ICs and their application," K. K. O, K. Kim, B. A. Floyd, J. L. Mehta, H. Yoon, C.-. Hung, D. Bravo, T. O. Dickson, X. Guo, R. Li, N. Trichy, J. Caserta, W. R. Bomstad, II, J. Branch, D.-J. Yang, J. Bohorquez, E. Seok, L. Gao, A. Sugavanam, J.-J. Lin, J. Chen, and J. E. Brewer, *IEEE Trans. Electron Devices*, vol. 57, no. 1, pp. 1312–1321, July 2005.

[4] Y. Zheng, Y. Zhang, and Y. Tong, "A novel wireless interconnect technology using impulse radio for interchip communications," *IEEE Trans. Microw. Theory Tech.*, vol. 54, no. 4, pp. 1912–1920, April 2006.

[5] W.-H. Chen, S. Joo, S. Sayilir, R. Willmot, T.-Y. Choi, D. Kim, J. Lu, D. Peroulis, and B. Jung, "A 6-Gb/s wireless inter-chip data link using 43-GHz transceivers and bond-wire antennas," *IEEE Journal of Solid-State Circuits* vol. 44, no. 10, pp. 2711–2721, Oct. 2009.

[6] A. T. de Hoop, H. Blok, I. E. Lager, M. Štumpf, and G. A. E. Vandenbosch, "Pulsed-field emi susceptibility analysis of microelectronic circuits – a full time-domain methodology," in *Proc. 42nd European Microwave Conference – EuMC*, pp. 337-339, Amsterdam, the Netherlands, Oct.-Nov. 2012.

[7] Federal Communications Commission, "First Report and Order," April 2002.

[8] National Telecommunications and Information Administration, "Manual of regulations and procedures for federal radio frequency management," May 2011 Revision of the 2008 Edition [Online] Available: http://www.ntia.doc.gov/files/ntia/publications/manual_5_11.pdf.

[9] I. E. Lager, A. T. de Hoop, and T. Kikkawa, "Pulsed-field wireless interconnects in digital integrated circuits – a time-domain signal transfer and electromagnetic emission analysis," in *Proc. 6th European Conference on Antennas and Propagation – EuCAP*, pp. 1855–1859, Prague, Czech Republic, April, 2012.

[10] International Electrotechnical Commission, *International Electrotechnical Vocabulary*, [Online]. Available: http://www.electropedia.org.

[11] A. T. de Hoop, *Handbook of Radiation and Scattering of Waves*, London: Academic Press, 1995, xxx + 1085 pp.; electronic reproduction (with corrections) 2008, freely downloadable, for private use, from http://www.atdehoop.com.

[12] A. T. de Hoop, I. E. Lager, and V. Tomassetti, "The pulsed-field multiport antenna system reciprocity relation – a time-domain approach," *IEEE Trans. Antennas Propag.*, vol. 57, no. 3, pp. 594–605, March 2009.

[13] P. K. Saha, N. Sasaki, and T. Kikkawa, "A CMOS monocycle pulse generation circuit in a ultra-wideband transmitter for intra/inter chip wireless interconnection," *Jpn. J. Appl. Phys.*, vol. 44, no. 4B, pp. 2104–2108, April, 2005.

[14] I. E. Lager, A. T. de Hoop, and T. Kikkawa, "Model pulses for performance prediction of digital microlectronic systems," *IEEE Trans. Compon., Packag., Manuf. Technol.*, vol. 2, no. 11, pp. 1859–1870, Nov. 2012.

[15] I. E. Lager and A. T. de Hoop, "Model pulses for time-domain analysis of ultra wideband systems: Causality in the time-domain versus regulatory masks in the spectral domain," *IEEE Trans. Antennas Propag.*, submitted.

[16] R. N. Bracewell, *The Fourier Transform and Its Applications*, Boston: McGraw-Hill, 2000.